Subsurface Flow and Transport Model Development for the Operable Unit 7-13/14 Remedial Investigation and Feasibility Study

Swen O. Magnuson
A. Jeffrey Sondrup

March 2006

Idaho Cleanup Project

Subsurface Flow and Transport Model Development for the Operable Unit 7-13/14 Remedial Investigation and Feasibility Study

Swen O. Magnuson
A. Jeffrey Sondrup

Edited by LauraLee Gourley

March 2006

Idaho Cleanup Project
Idaho Falls, Idaho 83415

ABSTRACT

In support of the remedial investigation and baseline risk assessment and feasibility study for Operable Unit 7-13/14, a numerical model has been developed to simulate subsurface transport of contaminants released from buried waste at the Subsurface Disposal Area at the Idaho National Laboratory Site. The model, referred to as the remedial investigation and feasibility study model, is the latest and most comprehensive in a series of Subsurface Disposal Area subsurface contaminant transport models, and features significant improvements over the most recent predecessor model presented in the *Ancillary Basis for Risk Analysis*. The model incorporates and uses the latest characterization and monitoring data and represents the current best interpretation of water movement and contaminant transport in the Subsurface Disposal Area subsurface.

This document contains a summary of the conceptual model and how it was implemented into a numerical model, not only for purposes of assessing risk, but also for purposes of evaluating remedial alternatives as part of the feasibility study. The report contains all relevant model assumptions, and the basis for selection of model parameter values. In addition, it describes all modifications and improvements made to the Ancillary Basis for Risk Analysis model, and summarizes specific modeling studies supporting the revisions. Simulation results, in terms of moisture distributions and resulting contaminant concentrations, are presented for the remedial investigation and baseline risk assessment base case and different sensitivity cases. Finally, a discussion of the model's applicability, strengths, limitations, and general uncertainty is included.

CONTENTS

FIGURES

TABLES

ACRONYMS

ABRA   Ancillary Basis for Risk Analysis

COPC   contaminant of potential concern

INL   Idaho National Laboratory

IRA   Interim Risk Assessment

RI/BRA   remedial investigation and baseline risk assessment

RI/FS   remedial investigation and feasibility study

RWMC   Radioactive Waste Management Complex

SDA   Subsurface Disposal Area

USGS   United States Geological Survey

VOC   volatile organic compound

VVET   vapor vacuum extraction with treatment

Subsurface Flow and Transport Model Development for the Operable Unit 7-13/14 Remedial Investigation and Feasibility Study

1. INTRODUCTION

This document presents development of the predictive flow and transport model used to evaluate the fate of contaminants from waste buried in the Subsurface Disposal Area (SDA) for the ongoing Operable Unit 7-13/14 remedial investigation and baseline risk assessment (RI/BRA) and feasibility study. This document is a companion to the draft RI/BRA and relies on discussions of geology, hydrology, and contaminant monitoring presented in the draft RI/BRA. A separate companion document describes the source-release model that addresses inventory and release mechanisms (Anderson and Becker 2006). An assumption is made that review of the draft RI/BRA will not produce substantive comments that would warrant changes to this modeling report.

1.1 Modeling Background

A series of numerical simulators have been developed by the Operable Unit 7-13/14 Project to represent water movement and contaminant transport beneath the SDA. Before this current model, the most recent model was the flow and transport simulation model developed for the Ancillary Basis for Risk Analysis (ABRA) (Holdren et al. 2002). That model will be referred to as the ABRA model in this report. An earlier model that preceded the ABRA model was presented in Magnuson and Sondrup (1998) and was used for the Interim Risk Assessment (IRA) (Becker et al. 1998). That model is referred to as the IRA model. Each of these previous models represented best available knowledge of subsurface information at the time they were developed to assess risks from transport of contaminants along the groundwater pathway. This information has evolved over time, along with understanding of the impacts of some of the assumptions included in the earlier modeling and the belated discovery of some minor errors in the implementation of the ABRA model, necessitating the development of a new model to support the Operable Unit 7-13/14 remedial investigation and feasibility study (RI/FS).

In this sequence of models developed for the Operable Unit 7-13/14 Project, the aquifer portion of subsurface pathway modeling has always been treated conservatively with simplistic assumptions that result in three-dimensional, advective-dispersive transport. Emphasis has been on developing the vadose zone model to relax conservative assumptions used in screening-level models.

The model developed for this report, called the RI/FS model, represents the most current and comprehensive interpretation of water and contaminant movement in the subsurface and was derived from the model presented in the ABRA. The improved information, minor errors in the ABRA model, and revised assumptions are summarized in Section 2. For the benefit of readers familiar with the ABRA model, detailed comparisons of assumptions and parameterization between the ABRA model and the RI/FS model are presented throughout this report.

The RI/FS model represents water movement and contaminant transport in the subsurface after contaminants are released from their disposal locations. This representation mimics flow and transport, where possible, and makes conservative assumptions otherwise. Simulations were also completed to support the Operable Unit 7-13/14 feasibility study, using this updated model with reduced infiltration and various treatments on waste inventory beginning in Calendar Year 2010. These same feasibility study simulations also support the radiological low-level waste performance assessment and composite analysis required to meet Department of Energy Order 435.1 requirements.

1.2   Subsurface Disposal Area Background

Originally established in 1949 as the National Reactor Testing Station, the Idaho National Laboratory (INL) Site is a Department of Energy-managed reservation, occupying 2,305 km^2 (890 mi^2) in the northeastern region of the Snake River Plain. The INL Site extends nearly 63 km (39 mi) from north to south, is about 58 km (36 mi) wide in its broadest southern portion, and occupies parts of five southeastern Idaho counties (Holdren et al. 2002).

Located in the southwestern quadrant of the INL Site, the Radioactive Waste Management Complex (RWMC) encompasses a total of 72 ha (177 acres) and is divided into three separate areas by function: the SDA, the Transuranic Storage Area, and the administration and operations area. The current size of the SDA is 39 ha (97 acres)—approximately 35 of the 97 acres contains waste. Located adjacent to the east side of the SDA, the Transuranic Storage Area was added to RWMC in 1970, encompasses 23 ha (58 acres), and is used to store, prepare, and ship stored transuranic waste to the Waste Isolation Pilot Plant. The 9-ha (22-acre) administration and operations area at RWMC includes administrative offices, maintenance buildings, equipment storage, and miscellaneous support facilities (Holdren et al. 2002).

The SDA is a radioactive waste landfill with shallow subsurface disposal units consisting of pits, trenches, and soil vaults (see Figure 1-1). Constituents in the landfill include hazardous chemicals, remote-handled fission and activation products, and transuranic radionuclides. Waste acceptance criteria and record-keeping protocols for the facility have changed over time in keeping with waste management technology and legal requirements. Today's requirements are much more stringent as a result of knowledge developed over the past several decades about potential environmental effects of waste management techniques. Previously, however, shallow landfill disposal of radioactive and hazardous waste was the conventional disposal technology.

Construction, operation, and decommissioning of INL Site nuclear reactor testing programs have resulted in large volumes of waste. Various containers were used in shipping and disposing of waste, including steel drums, casks, cardboard cartons, and wooden boxes. Larger individual items—such as tanks, furniture, process and laboratory equipment, engines, and vehicles—were placed separately as loose trash. Additionally, liquid waste was buried in the SDA, including direct disposal of free liquids to pits and trenches and disposal of solidified liquids in containers (Holdren et al. 2002).

Radioactive waste from off-INL Site sources originated from a variety of facilities, including military and other defense agencies, universities, commercial operations, and the U.S. Atomic Energy Commission. The primary off-INL Site contributor was the Rocky Flats Plant. Shipping of waste to the INL Site from the Rocky Flats Plant began in April 1954 and continued into late 1989. Waste from the Rocky Flats Plant was deposited underground in a series of pits and trenches until 1970, when the U.S. Atomic Energy Commission policy was implemented requiring segregation and retrievable storage of all solid transuranic waste. After 1970, transuranic waste received from the Rocky Flats Plant was placed in aboveground, earthen-covered retrievable storage at the Transuranic Storage Area. Aboveground stored waste was designated as transuranic retrievable waste (Vejvoda 2005). Initially, waste was stacked in pits and trenches. However, beginning in 1963, some waste was dumped to reduce labor costs and minimize radiation exposure of personnel. Current disposal operations stack contact-handled waste to maximize disposal capacity of the landfill. Remote-handled waste is placed in either concrete vaults or the bulk storage area.
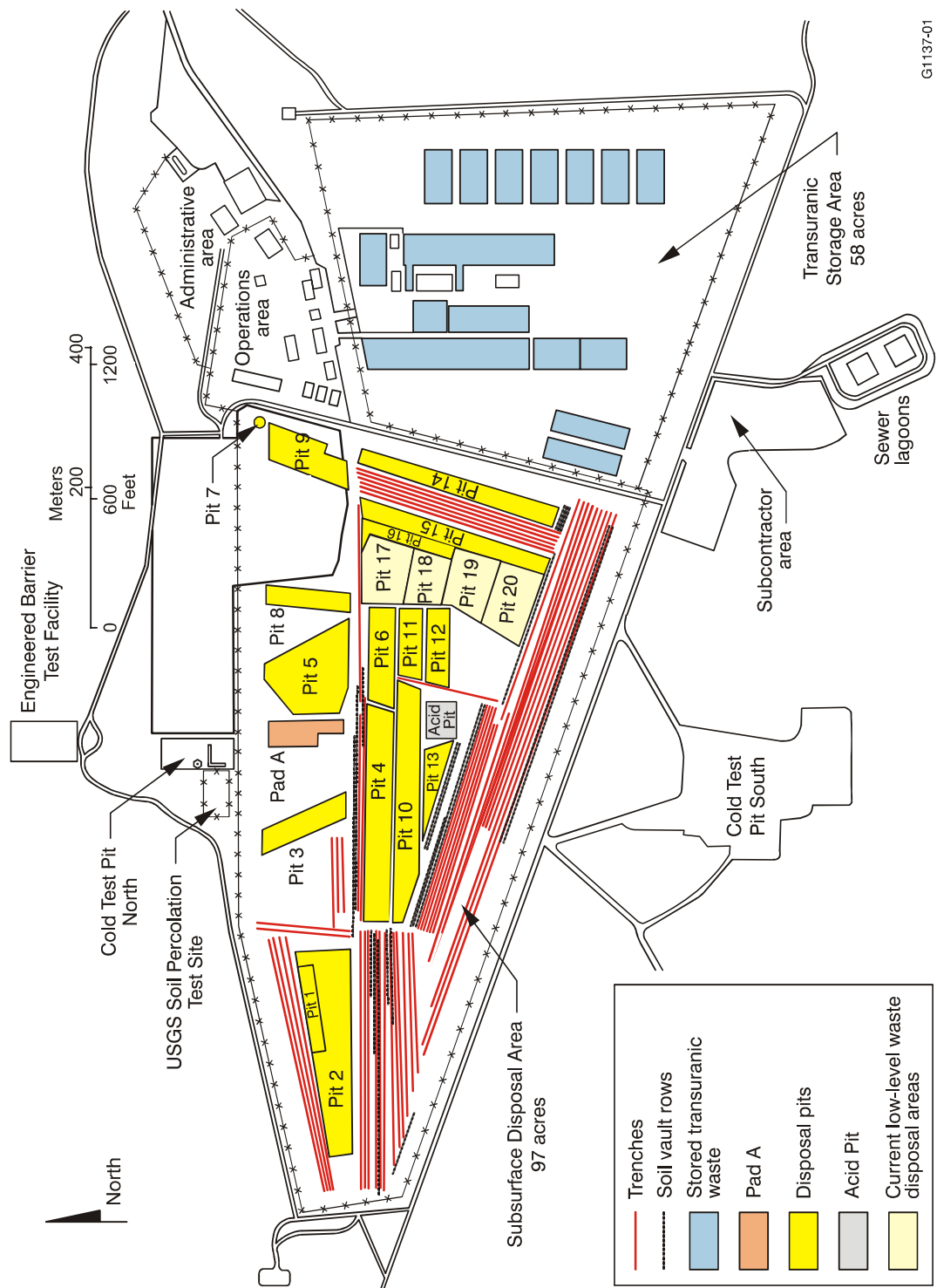
Figure 1-1. Map of the Radioactive Waste Management Complex showing pits, trenches, and soil vault rows within the Subsurface Disposal Area.

1-3

1.3   Objectives

The overall objective in developing the RI/FS model was to create a simulator that would be sufficiently representative of water movement and contaminant transport so that predictive simulations would be suitable to support decisions that will be made during the Operable Unit 7-13/14 RI/FS process. In this instance, sufficiently representative means the model generally represents observed transport or can be demonstrated to be conservative with respect to maximizing groundwater-pathway concentrations. For clarity, the latter would result in overpredicting concentrations in the aquifer.

This document has the following specific objectives:

- Summarize modifications and improvements to the ABRA model and parameters

- Summarize specific modeling studies that support revisions to the ABRA model

- Document base-case model simulations used for the Operable Unit 7-13/14 RI/BRA

- Document base-case sensitivity simulations for the Operable Unit 7-13/14 RI/BRA

- Document feasibility study simulations for Operable Unit 7-13/14

- Document simulations for the Department of Energy Order 435.1 performance assessment and composite analysis

- Summarize limitations of the resulting model in terms of calibration and processes included and excluded.

1.4   Scope

This document provides a complete description of the Operable Unit 7-13/14 flow and transport model used for the RI/FS. Also presented are modeling studies conducted since the ABRA model was developed to support revision of the ABRA model and determination of parameters in the Operable Unit 7-13/14 RI/FS flow and transport model.

1.5   Report Organization

Previous IRA and ABRA modeling efforts for Operable Unit 7-13/14 are summarized and corrections and refinements to the ABRA model are discussed in Section 2.

The TETRAD numerical simulator is described in Section 3, along with modifications to the TETRAD simulator to facilitate use for Operable Unit 7-13/14 RI/FS modeling.

The conceptual model, underlying assumptions, and complete description of the Operable Unit 7-13/14 flow and transport model are provided in Section 4.

Section 5 presents simulations that were performed as part of parameterizing the RI/FS model. Section 5 also includes comparisons to measured matric potentials from the advanced tensiometer network, comparisons of simulated velocities in the fractured basalt, a simulation study on chloride brine transport beneath the SDA, CCl_4 calibration, and the implementation process for simulating C-14 with partitioning into the gaseous phase.

A comparison of simulated concentrations from the RI/FS model in the surficial sediment, deeper vadose zone, and aquifer are discussed in Section 6, along with a description of the RI/BRA sensitivity

simulations, simulations to be performed for the feasibility study, and simulations performed for the performance assessment and composite analysis.

Appendixes A through H contain complete details of supplemental modeling studies that support the Operable Unit 7-13/14 RI/FS model.

2. PREVIOUS OPERABLE UNIT 7-13/14 COMPREHENSIVE MODELS AND IMPROVEMENTS FOR THE REMEDIAL INVESTIGATION AND FEASIBILITY STUDY MODEL

This section describes previous models developed for Operable Unit 7-13/14 to represent comprehensive evaluations of subsurface water and contaminant movement for the purpose of risk analysis. It then summarizes improvements implemented in the RI/FS model.

2.1 Predecessor Models

The RI/FS model represents culmination of a sequence of iterative modeling. The two previous iterations of three-dimensional modeling are the IRA model and the ABRA model. Both are described briefly to provide context for the RI/FS model.

2.1.1 Interim Risk Assessment Model

The IRA model represented the first attempt to simulate flow and transport through the entire vadose zone and aquifer domains for an extensive suite of contaminants of potential concern (COPCs). Calibration of vadose zone perched water behavior and an interpreted contribution to nitrate concentrations in the aquifer were attempted for the IRA model. Results were termed limited in their degree of success in emulating observed behavior. Attempts to improve calibration were hindered by lack of a widespread, well-behaved, identifiable plume in the vadose zone attributed strictly to dissolved-phase transport. Typically, contaminants in the vadose zone beneath the SDA (see Section 4 of the draft RI/BRA) are either not detected or are detected at very low concentrations with no stable temporal trends; therefore, monitoring data that could be used to demonstrate transport of a dissolved-phase nonsorbing contaminant were extremely sparse. The IRA model was used to make a series of 10,000-year predictive aquifer simulations for 52 contaminants. Results of that modeling formed the basis for risk estimates in the IRA (Becker et al. 1998) and were used to screen contaminants for the ABRA.

Waste management personnel at the INL Site also used the IRA model to update both the performance assessment (Case et al. 2000) and the composite analysis (McCarthy et al. 2000). The IRA model development, implementation, and results have undergone extensive review by Fabryka-Martin, Gee, and Flint (1999) and the U.S. Geological Survey (USGS) (Rousseau et al. 2005). Though reviews of the IRA model were generally complimentary, none concluded that the IRA model was satisfactory for developing conclusive predictions of the fate and transport of contaminants in the subsurface. The USGS review was by far the most extensive. The main comments from Rousseau et al. (2005) about modeling flow and transport of radionuclides at RWMC follow:

- Modeling performed for the IRA cannot necessarily be shown to be conservative.

- Spatial variability of hydrologic and transport properties of the sedimentary interbeds should be evaluated, and the impact of including this spatial variability into the IRA model should be assessed.

- Impacts of additional sources of vadose zone water from the Big Lost River system on predicted contaminant concentrations should be evaluated.

- Selected distribution coefficient (K_d) values used in the IRA cannot be shown to be conservative because they do not account for (1) colloidal transport, (2) the enhanced actinide mobility fraction observed in column studies, (3) variations in mineralogy, (4) nonlinearity of isotherms, and (5) fluctuations in pore-water chemistry. Furthermore, K_d values taken from the literature cannot be shown to be representative of the SDA.

2.1.2 Ancillary Basis for Risk Analysis Model

The ABRA model was developed to respond to each of the USGS review observations, particularly the second and third bullets (Rousseau et al. 2005). The vadose zone and aquifer portions of the simulation domain were separated, allowing increased discretization in the vadose zone model. This improved discretization included a gridding method that used variable gridblock thicknesses to better conform to the topography of the interbeds. The lithologic selections included interpretations from 22 additional wells drilled in 1999. Sediment cores were collected from the B-C and C-D interbeds and analyzed for hydrologic and transport properties. These analyses allowed a spatial description of the hydrologic properties to be implemented in the ABRA model. The aquifer model was further calibrated to take advantage of seven new wells completed since publication of the IRA model.

Additional refinement in the vadose zone model allowed an improved resolution of waste streams in the source-release model, with a closer match between infiltration rates assigned in the vadose zone model and those assigned in the source-release model. Twenty-four contaminants, which were all radionuclides with the exception of nitrate, were simulated with the ABRA model. Volatile organic compounds (VOCs) were not simulated with the ABRA model.

This ABRA model was used to make estimates of possible effects on groundwater-pathway risks from implementation of a preliminary set of remedial alternatives. Results of this modeling were documented in the Preliminary Evaluation of Remedial Alternatives (Zitnik et al. 2002). Alternatives that were evaluated singly and in combinations included an infiltration-reducing cap, in situ grouting, in situ vitrification, and waste removal.

2.2 Corrections to the Ancillary Basis for Risk Analysis Model

Three errors in the ABRA model were discovered since publication of the ABRA report. These errors have been corrected in the RI/FS model and are discussed individually.

2.2.1 Vadose Zone Vertical Grid Extension

The bottom 27.4 m (90 ft) of the vadose zone simulation domain were inadvertently omitted from the ABRA. This 27.4-m (90–ft) portion represents fractured basalt and would, therefore, have had minimal impact on the simulation results because fractured basalt hydrologic-property parameterization ensures rapid water movement. Because only dissolved-phase transport was simulated in the ABRA, this rapid water movement also ensured rapid dissolved-phase transport. There would not have been any noticeable increase in contaminant travel times through the vadose zone if the 27.4 m (90 ft) had been included.

Because the RI/FS model includes vapor-phase transport, the missing 27.4 m (90 ft) would be potentially more important; therefore, the RI/FS model domain now correctly extends down to the bottom of the vadose zone, requiring additional gridblocks in the base vadose zone domain, and slightly adds to the computational requirements for the RI/FS model.

2.2.2 Spatially Variable Interbed Porosity and Permeability

Kriged B-C and C-D interbed porosities and permeabilities were used in the ABRA. A row versus column indexing inconsistency in the assignment of permeabilities resulted in an incorrect permeability field for both the B-C and C-D interbeds. The kriged permeability fields from Leecaster (2002) are now correctly implemented in the RI/FS model. In addition, an error occurred in selecting minimum versus averaged porosities from the core–sample-characterization results for the B-C interbed. This error was also corrected. Additionally, Leecaster (2002) used the minimum instead of average porosities from each location where core samples were evaluated for the B-C interbed evaluation. The spatial variability analysis and kriging of porosities onto the vadose zone-model domains for the B-C and C-D interbed was reanalyzed for the RI/FS model with slightly higher averaged B-C interbed porosities. The reanalysis is contained in Appendix F. Neither of these errors was substantive in affecting simulation results presented in the ABRA.

2.2.3 Interface Between Source-Release and Vadose Zone Models

The source-release model requires a count of the number of gridblocks into which contaminant mass was loaded. In conducting the ABRA, this number of gridblocks was slightly increased, but the information provided to the source-release model was not updated. The result was to slightly increase the mass input to the vadose zone model above what should have been applied.

An additional check was added to the software interface between the source-release and vadose zone models. This interface program processes source-release results into the format necessary for input to the vadose zone flow and transport model. The additional check ensures consistency between the numbers of gridblocks in both models and thereby verifies that mass out of the source model equals mass into the vadose zone model.

2.3   Aquifer Domain Extension

The 1E-05 risk isopleth at the time of maximum overall risk for a spatially-consistent receptor was not closed in the ABRA aquifer model domain (see Figure 6-31 in Holdren et al. [2002]). Instead, this risk isopleth extended south of the INL Site boundary. For the RI/FS model, the aquifer domain was extended southward and westward to ensure the 1E-05 risk isopleth would be closed. This task required adopting permeabilities from the Operable Unit 10-08 aquifer model[a] (McCarthy et al. 1995) for extended portions of the domain, and interpolating new boundary conditions from Calendar Year 2000 water level data (i.e., the same that were used for the ABRA aquifer model calibration). Extension of the aquifer model domain is explained in detail in Appendix C.

2.4   Lithology Database Quality Assessment

An extensive effort to document selected lithologic contacts between sediment and basalt in the vadose zone and the thickness of the surficial sediment and sedimentary interbeds was conducted in support of RI/FS modeling. Results of this effort are documented in the *Updated Stratigraphic Selections for Wells in the Vicinity of the Subsurface Disposal Area* (Ansley, Helm-Clark, and Magnuson 2004). During this effort, previous stratigraphic selections by Anderson et al. (1996) were verified to be correctly entered into the data files used for the RI/FS spatial variability and kriging analysis. The primary effort, however, was in reevaluating lithologic selections for each well drilled since 1995, and in making new

---

[a] The updated INL Site-wide aquifer model, in preparation for Operable Unit 10-08, will maintain consistency with simulated SDA-vicinity water velocities from the Operable Unit 7-13/14 RI/FS model in accordance with the *Idaho National Engineering and Environmental Laboratory Operable Unit 10-08 Sitewide Groundwater Model Work Plan* (DOE-ID 2004).

selections for wells drilled since publication of the ABRA report through March 2003. The basis for lithologic selection for each well was reviewed and reinterpreted, as necessary, using suites of geophysical logs as the primary basis and driller lithologic logs as a last resort. This prioritization method resulted in several occurrences where the nonzero thickness locations used for the ABRA became zero-thickness locations in the draft RI/BRA and vice versa. These occurrences are highlighted in Table A-1 of Ansley, Helm-Clark, and Magnuson (2004). After lithologic selections were finalized, the spatial variability analysis and kriged surfaces and thicknesses of sedimentary features were updated (Leecaster 2004) for the vadose zone RI/FS model.

2.5   No Spreading Area Influence in the Vadose Zone

The ABRA model included a steady-state influence of additional water above the C-D interbed to emulate the effect of the spreading areas. Sensitivity simulations, without this additional water, presented in the ABRA showed that the effect of the additional water was to dilute the resulting aquifer concentrations for contaminants that underwent dissolved-phase transport. This finding was most applicable for contaminants with long half-lives that do not undergo substantial decay during transit of the vadose zone. Since short-lived contaminants, such as Sr-90 and Cs-139, are not evaluated for groundwater pathway in the RI/FS, it is appropriate that the RI/FS model does not include this additional spreading area water above the C-D interbed.

2.6   Reduction of Infiltration Rate Assigned Inside the Subsurface Disposal Area

Three infiltration rates were assigned to different regions inside the SDA in the ABRA model. These rates represented low-, medium-, and high-infiltration rates and were based on inverse modeling to neutron probe access tube measurements documented in the UNSAT-H infiltration model calibration report (Martian 1995). The high-infiltration rate of 24.1 cm/year (9.5 in./year) was based on results from three locations that had extremely high-infiltration rates due to the neutron probe access tubes being located in areas of low topography (e.g., near ditches). Excluding these three infiltration rates from the Martian (1995) estimates resulted in an upper-bound or high-infiltration rate of 10.0 cm/year (3.9 in./year), which was judged more appropriate for an upper-bound on infiltration through the waste.

2.7   Facilitated Transport of Plutonium-239 and Plutonium-240

Facilitated transport mechanisms (e.g., colloidal transport) may affect contaminant migration in the SDA subsurface. In the ABRA, facilitated transport was considered only as a sensitivity case. As recommended by Batcheller and Redden (2004), facilitated transport for a portion of the Pu-239 and Pu-240 inventory in the buried waste was adopted in the base-case model by assigning a K_d of 0 mL/g for the source zone, surficial sediment, and the A-B interbed. Batcheller and Redden (2004) further concluded that plutonium would sorb to the deeper B-C and C-D interbeds, inhibiting continued downward transport through the vadose zone.

2.8   Revision of Sediment Distribution Coefficients

Distribution coefficient values used in the RI/FS model were reassessed. In the methodology used for the batch tests (Fjeld, Coates, and Elzerman 2000), on which several of the values in the ABRA were based, the fraction of soil samples that were above 250 μm was removed before testing. Using only finer sediment particles in the batch tests introduced a bias to the results that overestimated the distribution coefficients. Using a weight ratio of the sieved fraction to the estimated total sample weight, an Environmental Protection Agency recommended method (EPA 1999) was used to adjust distribution

coefficients downward for actinium, americium, plutonium, and thorium. Distribution coefficients for uranium and neptunium were revised upward, based on results of batch tests measured on soil cores from wells drilled in Fiscal Year 2003 (Leecaster and Hull 2004). The complete list of final distribution coefficients for the RI/FS modeling appears in Table 4-4.

2.9   Gaseous-phase Simulation of Carbon-14 and Volatile Organic Compounds

Carbon-14 was simulated as a purely dissolved-phase contaminant in the ABRA, resulting in overestimated groundwater-pathway transport because two processes were neglected that allowed C-14 to escape the vadose zone through land surface. These processes were (1) partitioning of C-14 into the gaseous phase, which allows part of the C-14 mass to diffuse through the upper land surface boundary, and (2) gaseous-phase advection through that same boundary in response to changes in barometric pressure. In addition to simulating dissolved-phase movement of C-14, the RI/FS model also includes partitioning of C-14 into the gaseous phase, which accounts for losses to the atmosphere.

Volatile organic compounds were not simulated for the ABRA. Instead, VOCs were estimated by scaling the IRA (Becker et al. 1998) model results by the ratio of an updated inventory to the previous inventory. Current inventories were used for the RI/FS model, and the updated RI/FS model was used to simulate VOC transport. Calibration was performed using CCl_4 measurements from the extensive vadose zone gas-port-monitoring network and data from the groundwater-monitoring network. The calibration was performed primarily by adjusting tortuosity values, but much of the information gained from calibrating the IRA model was used in the RI/FS model. Another calibration parameter was the fractured basalt permeability horizontal-to-vertical anisotropy ratio. The ratio was changed from 30:1 used in the ABRA model to 300:1. This change helped to match the observed spreading of CCl_4 in the vadose zone, and demonstrated linkage between the flow model and the transport model for CCl_4. The VOC transport model also included the effects of air drilling and vapor vacuum extraction.

2.10   Increased Number of Waste Streams

In the ABRA model, the SDA was divided into 13 source areas for modeling contaminant release. For the RI/FS model, improvements in knowledge of contaminant inventories were used to refine the assignment into 18 source areas for modeling contaminant release and subsequent transport. A slight variation on the locations of the 18 waste streams was used when simulating VOCs (where the areas for Pits 4, 5, and 10 were slightly reduced in extent). This reduction is based on the Waste Information and Location Database tool and confirmation through soil-gas surveys (Housley, Sondrup, and Varvel 2002). Because of the influence of C-14 release from beryllium blocks on the C-14 risk, a third and different grouping was used to represent the blocks for the C-14 modeling.

3. TETRAD SIMULATION CODE

3.1 Description

The TETRAD computer code (Vinsome and Shook 1993), Version 12.7ms, was used for the RI/FS to simulate flow and transport. The TETRAD code has complete multiphase, multicomponent simulation capabilities and can mimic the behavior of any number of components in aqueous, gaseous, oleic, and solid phases. The TETRAD code has dual-permeability capabilities, which allow movement of components in a coupled fracture-matrix system. When dual permeability is invoked, water and contaminants move in both the aqueous and gaseous phases in both the fracture network and the basalt matrix. This dual-permeability feature was used in the RI/FS model to simulate movement of VOCs and C-14.

The general conservation equation solved by the TETRAD simulator for accumulation, flux, decay or degradation, and sources for any component i can be written as:

$$\frac{\partial W_i}{\partial t} + \vec{\nabla} \cdot \vec{N}_i - R_i + q_i = 0 \qquad\qquad (3\text{-}1)$$

where:

$\frac{\partial W_i}{\partial t}$ is the accumulation term that consists of net changes in concentration of the component i in any phase, including the adsorbed phase

$\vec{\nabla} \cdot \vec{N}_i$ is the divergence of the flux of component i

R_i is the change in concentration arising from decay of component i

q_i represents sources or sinks of component i.

The accumulation term can be written as:

$$W_i = \varphi \left(S_w \rho_w w_i + S_g \rho_g y_i + S_o \rho_o x_i \right) + \left((1-\varphi) \rho_s V_i \right) / M_i \qquad\qquad (3\text{-}2)$$

where:

φ is the porosity

S_j are the phase saturations (w aqueous, g gaseous, o oleic) of component i

ρ_j are the phase molar densities (w aqueous, g gaseous, o oleic) of component i

w_i y_i, and x_i are the mole fractions of component i in the aqueous, gaseous, and oleic phases, respectively

ρ_s is the solid phase density

V_i is the mole fraction of component i adsorbed on the solid phase

M_i is the molecular weight of component i.

A generalized sorption relationship is available in TETRAD that allows for sorption onto the solid phase from any of the other three phases.

The flux term in Equation (3-1) is comprised of an advection and dispersion term for each phase given by:

$$\vec{N}_i = \left[\rho_w \vec{u}_w w_i - \vec{D}_{iw} \cdot \vec{\nabla}(\rho_w w_i)\right] + \left[\rho_g \vec{u}_g y_i - \vec{D}_{ig} \cdot \vec{\nabla}(\rho_g y_i)\right] + \left[\rho_o \vec{u}_o x_i - \vec{D}_{io} \cdot \vec{\nabla}(\rho_o x_i)\right] . \qquad (3\text{-}3)$$

In Equation (3-3), the $\vec{u}_j$ are the phase advective fluxes given by the multiphase version of Darcy's law:

$$\vec{u}_j = \frac{-kk_{rj}}{\mu_j}\left(\vec{\nabla}P_j - \rho_j \vec{g}\right) \qquad (3\text{-}4)$$

where:

k is the intrinsic permeability

k_{rj} is the relative phase permeability

μ_j is the phase viscosity

P_j is the phase pressure

$\vec{g}$ is gravitational constant in vector form.

$\vec{D}_{ij}$ is the phase-dependant dispersion tensor comprised of molecular diffusion modified by porosity, phase saturation, tortuosity, and mechanical dispersion, consisting of phase dispersivities modified by directional components of advective phase fluxes (Bear 1972). The gravitational energy term is negative given that the positive z-direction is oriented downward in the TETRAD code.

The reaction term in Equation (3-1) accounts for decay or degradation of component i and is written as:

$$R_i = -A_{iK}\left(m_i + V_i(1-\varphi)\rho_r\right) + A_{\omega i}\left(m_\omega + V_\omega(1-\varphi)\rho_r\right); K \neq \omega \qquad (3\text{-}5)$$

where m_i is the total aqueous mass of i. The first term on the right hand side of Equation (3-5) accounts for component *i* decaying with a rate constant A_{iK} into component K ; whereas the second term on the right-hand side is the formation of *i* from destruction of component ω with a rate constant $A_{\omega i}$.

The final term on the right-hand side of Equation (3-1) is the source/sink term, q_i. This term accounts for addition or extraction of component *i* through wells or boundary conditions.

The TETRAD Version 12.7 code previously was used for the IRA and ABRA models. Before conducting modeling for the RI/FS, an evaluation exercise was performed to determine whether TETRAD was still the most appropriate code to use. This exercise resulted in a recommendation to continue using TETRAD for groundwater-pathway simulations for the RI/FS (Appendix C of Holdren and Broomfield 2004).

3.2 Modifications to Version 12.7 Resulting in Version 12.7ms

Modifications to improve computational efficiency for environmental modeling applications with the TETRAD simulator, Version 12.7, were described in Shook et al. (2003). The modified code resulting from this effort is called TETRAD, Version 12.7ms. Modifications were performed as part of an INL Laboratory-Directed Research and Development Project and consisted of allowing component-specific convergence criteria to be specified. This allowed tighter convergence criteria on those components representing contaminants, and looser criteria for those components representing pure water, air, and a required nonaqueous phase liquid. Appendix A describes simulation problems used to establish comparability of results between TETRAD Version 12.7 and Version 12.7ms. Two problems were simulated and results between the two versions were considered to be adequately consistent.

Two additional changes were implemented in the TETRAD simulator during transition from Version 12.7 to 12.7ms: (1) implementation of a Millington formulation (see Section 5.4.4.2) for calculating tortuosity during the simulation, based on total porosity and gaseous-phase saturation; and (2) modifications to limit repetitive time-step output for problems with frequent surface or internal boundary condition changes (e.g., emulating barometric pressure fluctuations or positive pressures imposed downhole during drilling of wells). These two changes only affected input and output from the TETRAD simulator and did not affect the solution method used internally.

3.3 Quality Control

The TETRAD 12.7ms simulator is a proprietary code, and its use constitutes an off-the-shelf application by modeling staff from the INL Site. Quality control for these types of simulations consists of ensuring that results are reproducible. This requires archiving a version of the simulator, model inputs, model outputs, and processing codes used to create inputs and outputs. An extensive searchable electronic archive is maintained by the Operable Unit 7-13/14 Project for this purpose. A description of this archive is contained in Appendix B. Appendix B also contains a copy of the software management agreement between the Idaho Cleanup Project and the Operable Unit 7-13/14 Project for this purpose.

4. OPERABLE UNIT 7-13/14 FLOW AND TRANSPORT MODEL DESCRIPTION

4.1 Conceptual Model

The general conceptual flow model treated water movement as though subsurface sediment were a heterogeneous, isotropic, porous medium. Net infiltration of meteoric water into the subsurface was described in the model by three constant rates representing areas of low, medium, and high infiltration (Martian 1995). Surficial sediment and sedimentary interbeds were simulated with varying thicknesses and upper-surface elevations (Leecaster 2004). Only the three uppermost interbeds were considered in the conceptual model. These were the A-B, B-C, and C-D interbeds. Interbeds deeper than the C-D interbed, though present in reality, were not included in the simulations. These deeper interbeds are also discontinuous, based on the fewer number of wells to this depth, and it is conservative to neglect them.

For strictly dissolved-phase contaminant transport, flow in the fractured basalt portion of the subsurface was considered as occurring only in the fracture network to emulate an anisotropic medium with a low effective porosity and a high permeability. For contaminants that also partition into the gaseous phase, both the exchange of water between the fracture network and the basalt matrix, and flow within the basalt matrix were assumed to affect flow and transport.

Sources of water were considered to be constant, allowing steady-state assignment of boundary conditions. The exception was including three transient events to represent historical flooding of the SDA. Transient infiltration events in response to changes in daily and seasonal meteorological conditions were evaluated in the IRA model and, as long as an assumption of equilibrium reversible sorption was included, these transient simulations showed no difference from the steady-state simulation at depth in the vadose zone.

Water that infiltrates the subsurface but does not contact buried waste serves primarily to dilute groundwater-pathway concentrations. Therefore, the effect of water migrating laterally at depth in the vadose zone from either Spreading Area A or B, or from the Big Lost River, was not included in the conceptual model. These additional sources of water were evaluated in the ABRA model and were found, primarily, to result in additional dilution for strictly dissolved-phase contaminants.

Movement of water in the aquifer was considered controlled by regional flow in the aquifer. Permeabilities were considered to be uniform vertically and pressures in the aquifer were considered to be in hydrostatic equilibrium, implying predominantly horizontal flow in the aquifer. Because of the long simulation time durations of hundreds to thousands of years, movement of water within the Snake River Plain aquifer was considered steady state. Neglecting transient influences in the aquifer, such as those that might occur from the spreading areas, is conservative because temporary changes in the direction of water velocity would result in additional dilution.

The effective depth of the Snake River Plain aquifer was assumed to be 76 m (250 ft). Robertson, Schoen, and Barraclough (1974) derived this estimate from the depth where tritium was observed in wells downgradient of the injection well at the Idaho Nuclear Technology and Engineering Center facility. More recent evaluations of temperature profiles indicate that the effective thickness is greater (Smith 2002). With predominantly horizontal flow, using a thinner aquifer thickness is conservative because less dilution occurs.

Locally, groundwater flow was affected by a region of low permeability in the aquifer (Wylie and Hubbell 1994). This region has been identified in wells immediately south of the SDA. This low-permeability region may extend underneath the SDA, as evidenced by the estimated transmissivity from a recent pumping test in Well M17S located centrally inside the SDA. Low velocities in the aquifer, as a result of including this low-permeability region, have an impact on model results. As contaminants enter the aquifer from the vadose zone, less dilution occurs in gridblocks with low aquifer velocities, and simulated contaminant concentrations are higher than they would be if the aquifer velocity were greater.

The general conceptual transport model for dissolved-phase transport considered advection, dispersion, diffusion, radioactive chain decay and ingrowth, and sorption in the sediment portions of the simulation domain.

In the fracture network within the basalt and basalt-matrix portions of the simulations, no sorption was assumed. Sorption in surficial and interbed sediment was assumed to follow linear reversible isotherms that could be described by use of K_ds. Sediment K_ds were assigned based on best-estimate values rather than conservative screening values. A set of best-estimate K_ds from Holdren and Broomfield (2004) was used in this application.

Facilitated transport mechanisms (e.g., colloidal transport) may affect contaminant migration in the SDA subsurface. Studies conducted with SDA interbed sediments have shown that very small fractions of plutonium and americium may move in a facilitated manner in the SDA. Grossman et al. (2001) showed that a very low mobile fraction forming from natural colloids in the soil (i.e., much less than 1%) was possible. Batcheller and Redden (2004) considered colloid formation from high-temperature processes and estimated that 3.7% of the waste stream could form colloids. This higher fraction is used for transport of Pu-239 and Pu-240 in the RI/BRA base case. Facilitated transport for Pu-239 and Pu-240 was considered to occur in the source zone and through the surficial sediment and A-B interbeds. The deeper B-C and C-D interbeds were considered as not allowing this facilitated transport to continue downward through the vadose zone because the B-C and C-D interbeds were treated as continuous in the model. This resulted in mechanical filtration for these two isotopes at this depth (Batcheller and Redden 2004) because water velocities are slowed at the interbeds. There are several locations where there are gaps in the B-C interbed inside the SDA (see Figure 4-8), but the interpolation process (Leecaster 2004) results in a nonzero thickness given the 76.2- × 76.2-m (250- × 250-ft) dimension of the gridblocks for the B-C interbed. There is a sensitivity case evaluated in Section 6.4.2 where the entire B-C interbed is neglected to examine the potential effects of gaps in the B-C interbed.

Single isolated detections of contaminants in the aquifer have occurred in the SDA during monitoring of subsurface contaminants. Though these isolated detections may be indicative of contaminant transport, it is not feasible with the current modeling approach to try to emulate each one. Instead, the subsurface-transport model attempts to mimic large-scale overall behavior of contaminants in the subsurface. This approach directs the model to emulate contaminants that are consistently present in a distributed manner in the subsurface. Contaminant monitoring in some locations in the vadose zone has identified likely trends in uranium, Tc-99, and nitrate. While not distributed adequately to be useful for calibration, these trends are compared against simulation results in Section 6.

Evaluation of aquifer contamination from upgradient sources in Section 2.3.4 of the draft RI/BRA concluded that there may be an influence from upgradient facilities on contaminant concentrations in the aquifer. The aquifer model ignores this possible influence and only considers regional background concentrations when making comparisons between simulated and observed results. Potential impacts from commingling plumes are the scope of the Operable Unit 10-08 Groundwater Modeling Project (DOE-ID 2004).

4.2   Assumptions

This section lists all assumptions that resulted from the conceptual model (discussed previously) or that were necessary to develop the subsurface model. Assumptions are divided into flow and transport categories. Most of these assumptions were the same as those used in developing the ABRA model. Assumptions that were modified for the RI/FS are italicized. These assumptions were applied only to the single-continua, dissolved-phase, subsurface flow and transport modeling. Assumptions relative to dual-continua modeling are included in Section 5.4.

4.2.1   Flow

- Infiltration is spatially variable inside the SDA and is greater than infiltration that occurs outside the SDA because of disturbed soil profiles with reduced vegetation inside the SDA.

- The spatially variable infiltration description of Martian (1995), adapted for the ABRA model, is adequate for base-case modeling.

- The higher infiltration rates, beginning in 1952, are implemented as though they were effective across the SDA.

- The background infiltration rate outside the SDA, through undisturbed vegetated sediment, is 1 cm/year (0.4 in./year).

- Initial conditions obtained from simulating a background infiltration rate of 1 cm/year (0.4 in./year) for 300,000 days (approximately 820 years) are adequate for representing the vadose zone beneath the SDA.

- The amount of water entering the SDA from the three historical floods is adequately estimated by Vigil (1988).

- Duration of infiltration from each of the historical flooding events is 10 days.

- Infiltration patterns in the SDA will remain the same indefinitely into the future for the base-case simulations and will be revised for feasibility study cases to reflect impact of an infiltration-reducing cover.

- The high-infiltration rate assigned over parts of the SDA by Martian (1995) is sufficient to account for occasional flooding of the SDA that may occur in the future for the base-case simulations.

- The surficial sediment and sedimentary interbeds have spatially variable lithologic surfaces and thicknesses that influence water and contaminant movement.

- Interbeds below the C-D interbed are thin and discontinuous and do not significantly affect flow and transport near the SDA. Neglecting the interbeds is conservative with respect to maximizing the groundwater-pathway concentrations.

- Hydrologic properties in the surficial sediment and A-B interbed are homogeneous. Hydrologic properties in the B-C and C-D interbeds are heterogeneous and varied spatially.

- The B-C and C-D interbeds have a low-porosity, low-permeability feature at their upper surface, which indicates either sediment within the interbed or the effect of fracture infilling by fine-grained sediment in the low-permeability basalt immediately above the interbed. (Though this feature was included in the subsurface model and discussed in detail in the IRA and ABRA modeling text, it was not specifically identified as an assumption.)

- Waste has the same hydrologic properties as surficial sediment.

- Flow in fractured porous basalt is controlled by the fracture network and is adequately represented as an anisotropic high-permeability, low-porosity, equivalent-porous continuum using a Darcian description.

- The field-scale hydraulic properties for fractured basalt were adequately described through inverse modeling by Magnuson (1995) for the large-scale infiltration test.

- *Any effect of water, from the Big Lost River discharged to the spreading areas, on water movement in the vadose zone beneath the SDA is neglected.* (In the ABRA, the effect of this influence was shown to primarily dilute concentrations for contaminants with long half-lives in the vadose zone and the aquifer. Not including the spreading-area influence is conservative with respect to maximizing the groundwater-pathway concentrations.)

- Water movement in the aquifer is treated as steady state. Possible influences of discharges from the Big Lost River to the spreading areas do not influence flow in the aquifer in the immediate vicinity of the SDA.

- Water levels corrected for borehole deviations from Fiscal Year 2003 are adequate for calibrating the Snake River Plain aquifer model and are representative of long-term, steady-state conditions.

- Within the aquifer, pressure is assumed to be in hydrostatic equilibrium and water movement is predominantly horizontal.

- A continuous region of low permeability exists locally in the aquifer, south and southwest of the SDA, that affects local flow directions.

- The effective depth of the Snake River Plain aquifer is 76 m (250 ft) (Robertson, Schoen, and Barraclough 1974).

4.2.2 Transport

- Field-measured concentrations of contaminants are generally representative and valid, based on data quality requirements associated with sampling activities. Single, isolated detections of contaminants are anomalous and not representative because contaminants are not consistently present.

- Advection, dispersion, diffusion, sorption, and radioactive decay are the only processes that influence dissolved-phase contaminant movement in the subsurface beneath the SDA.

- A linear equilibrium reversible distribution coefficient is representative of all geochemical processes that occur between contaminants dissolved in water and sediment. All available site-specific information will be used to determine appropriate contaminant distribution coefficients.

- Distribution coefficients are homogeneous in the interbeds.

- Sorption does not occur in fractured basalt portions of the vadose zone and aquifer.

- *Facilitated transport occurs in the vadose zone above the B-C interbed for Pu-239 and Pu-240. These isotopes undergo sorption within the B-C and C-D interbeds (Batcheller and Redden 2004).*

- No upgradient INL Site facilities influence aquifer-contaminant concentrations near the SDA, with the exception of nitrate, which has an estimated local background concentration of 1.4 mg/L.

- Feasibility study remedial alternatives will address (1) all estimated contamination retained in waste at the time of treatment, and (2) all contamination previously released that is still within the surficial sediment portion of the vadose zone model.

4.3   Vadose Zone Model

4.3.1   Domain and Horizontal Discretization

The same vadose zone horizontal domain and discretization was used in the RI/FS model as was used in the ABRA model. The extent of the vadose zone domain is shown in Figure 4-1. This horizontal extent was judged adequate to simulate flow and transport without undue influence from horizontal no-flux boundaries.

Horizontal gridding for the final vadose zone domain is shown in Figure 4-2. Two concentric levels of refinement are used to obtain adequate grid resolution in the SDA. The largest horizontal grids are 152.4 m (500 ft) on a side and the smallest gridblocks are 38.1 m (125 ft) on a side. Selection of the grid domain required a balance between the objectives of maximizing the extent of the domain so that outlying wells (e.g., Wells M7S, M15S, and M16S) could be included, while still obtaining sufficient resolution in the SDA for representing disposal locations and geologic and hydrologic features. Some outlying wells were not encompassed in the vadose zone simulation domain. The final domain extent was adequate to simulate transport without undue influence from the horizontal no-flux boundaries, which would otherwise truncate further horizontal spreading of water and contaminants in the vadose zone.

4.3.2   Lithology

An extensive effort to document selected lithologic contacts between sediment and basalt in the vadose zone and the thickness of the surficial sediment and sedimentary interbeds was conducted in support of the RI/FS model. The results of this effort are documented in Ansley, Helm-Clark, and Magnuson (2004). During this effort, previous interpretations by Anderson et al. (1996) were verified to be correctly entered into the data files used for the spatial variability and kriging analysis. The primary effort, however, was in reevaluating lithologic selections for each well drilled since 1995 and in making new selections for wells drilled since publication of the ABRA through March 2003. The basis for lithologic selection at each well was reviewed and reinterpreted as necessary using suites of geophysical logs as the primary basis and driller lithologic logs as a last resort. Table B-1 in Ansley, Helm-Clark, and Magnuson (2004) is the stratigraphic database for 134 wells deeper than the surficial sediment; this database is the foundation from which the RI/FS vadose zone model lithology is derived.
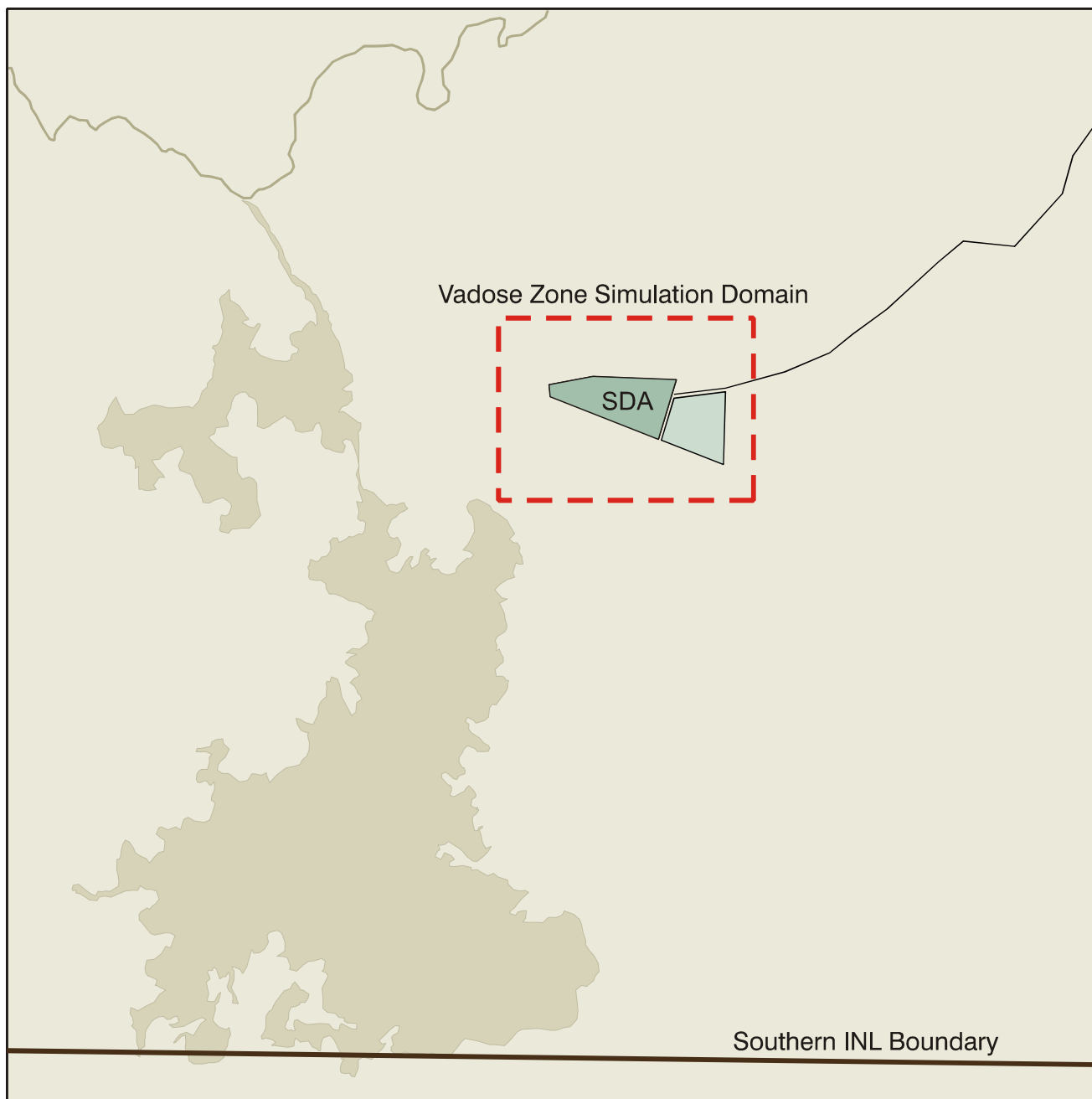
Figure 4-1. Horizontal domain for the remedial investigation and feasibility study vadose zone flow and transport.
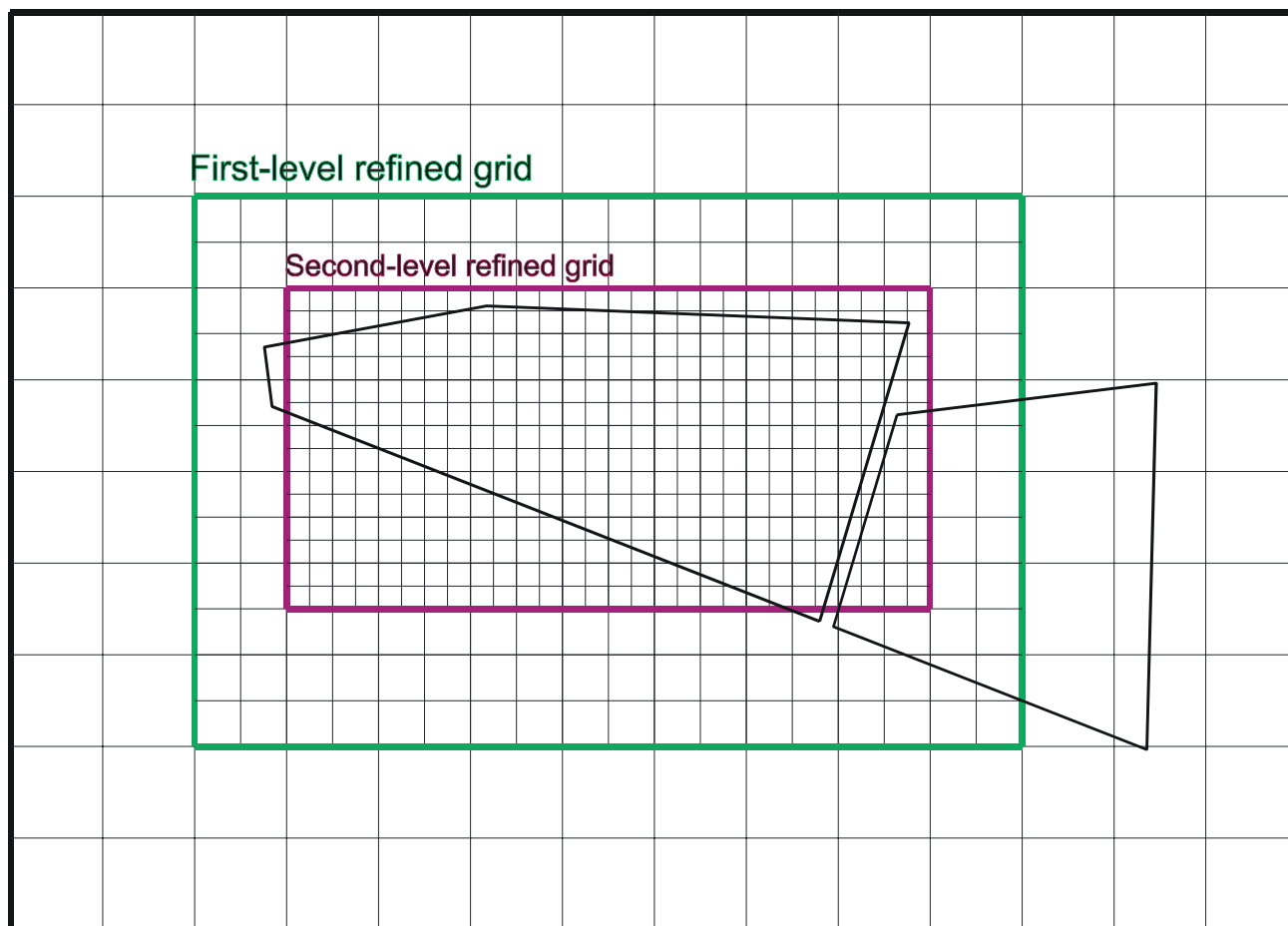
Figure 4-2. Horizontal discretization for the vadose zone model domain.

After lithologic selections were finalized, the spatial variability analysis and the kriged surfaces and thicknesses of the sedimentary features were updated for the Operable Unit 7-13/14 vadose zone model (Leecaster 2004). Surfaces and thicknesses, along with standard deviations for the surficial sediment and the A-B, B-C, and C-D interbeds were kriged for the base and refined grids and are contained in Leecaster (2004). The kriged surfaces and thicknesses are shown in Figures 4-3 through 4-10. The kriged results generally honor the data, with limited exceptions where both zero and nonzero thickness observations exist within a single grid. This is a result of single values being estimated for each grid and the smoothing that results from kriging. All lithologic selections were used in the kriging process without introducing bias by selectively removing locations with nonzero thickness when there were zero thickness locations nearby. The A-B interbed has two contiguous regions of gridblocks where the kriged thickness was zero, and is indicated by the zero contour line in Figure 4-6. These regions persist through the kriging because of the large number of wells with strictly zero thickness. Although it may be confusing to see an interpreted upper surface of the A-B interbed when that interbed is interpreted to be absent (compare Figure 4-5 to Figure 4-6), there was no A-B interbed in the model gridblocks inside the zero contour line indicated in Figure 4-6. The upper surface appears contiguous and nonzero everywhere in Figure 4-5 because the lithologic database (Ansley, Helm-Clark, and Magnuson 2004) contains information on the contact between the A and B basalt flows and treats the contact as the upper surface of the A-B interbed where it is not present.
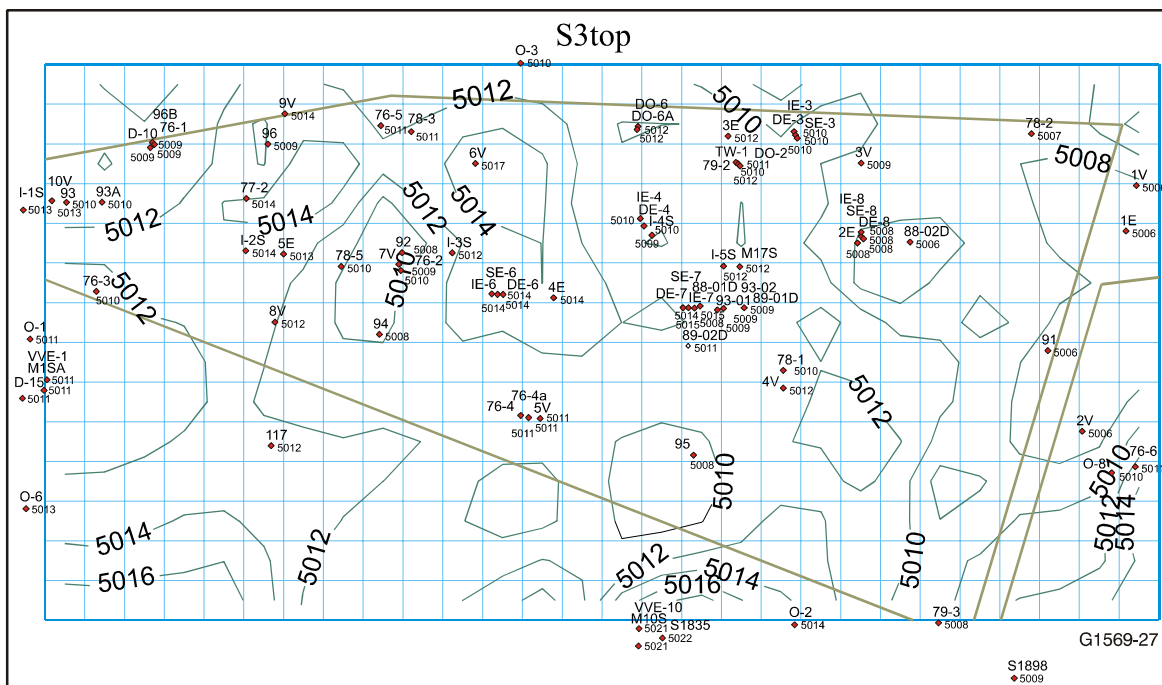
Figure 4-3. Kriged ground surface elevation (feet above mean sea level) for the second-level refined grid.
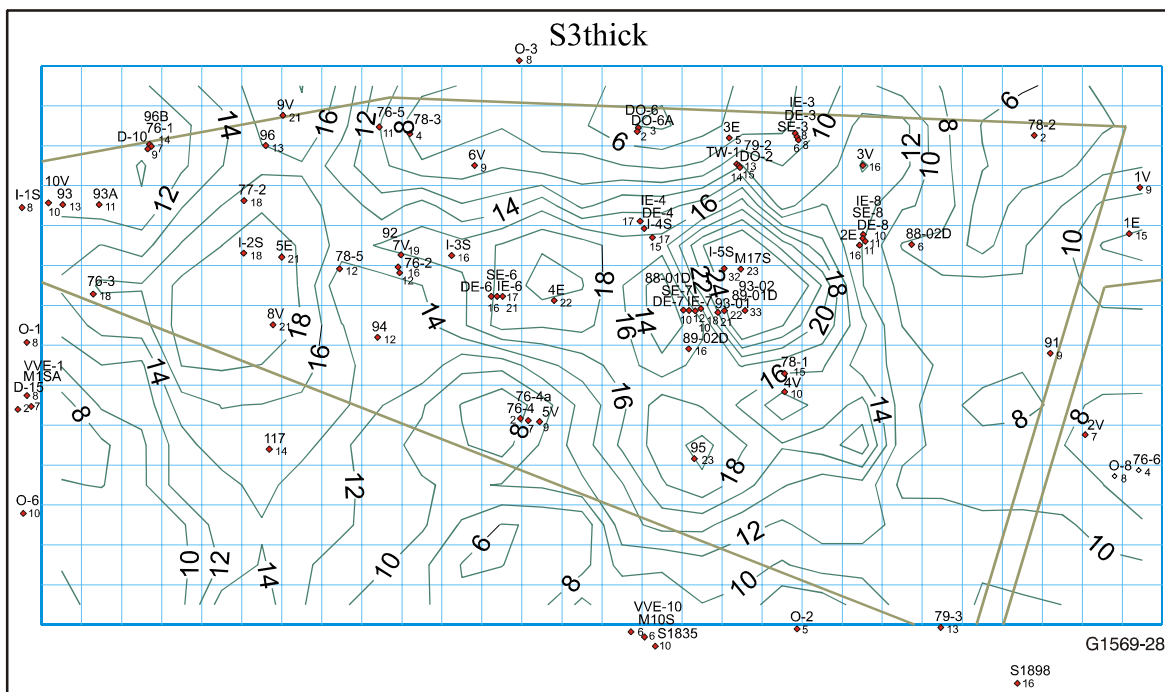
Figure 4-4. Kriged thickness (feet) of the surficial sediment for the second-level refined grid.

4-8
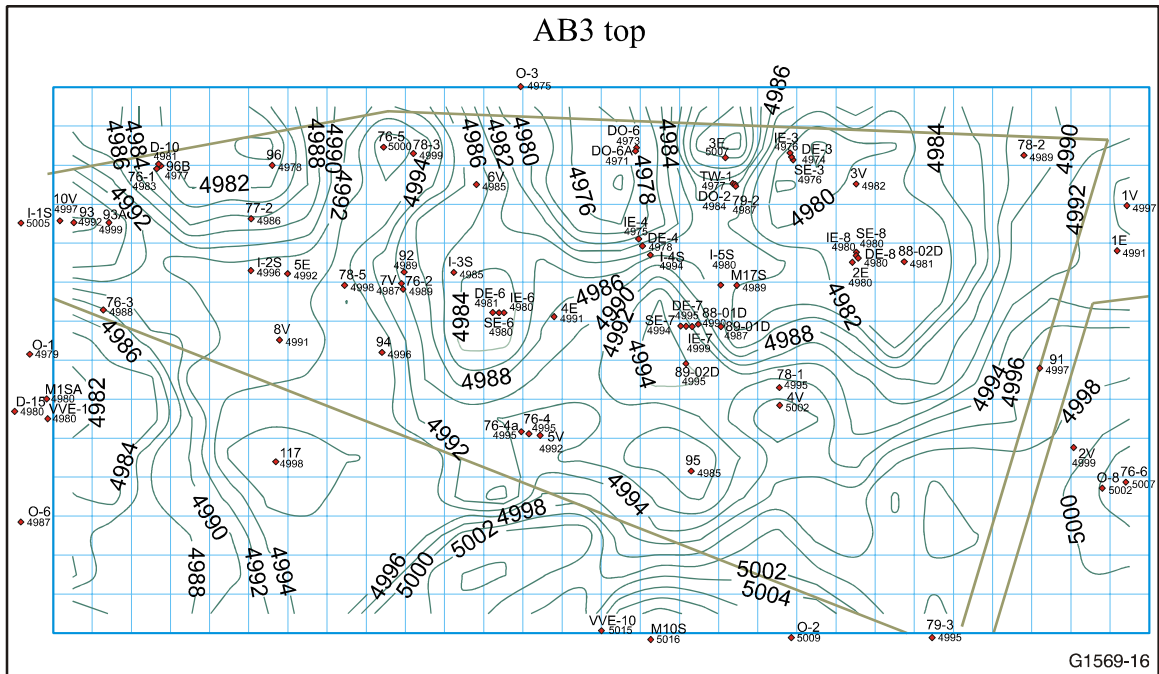
Figure 4-5. Kriged surface (feet above mean sea level) of the A-B interbed for the second-level refined grid.
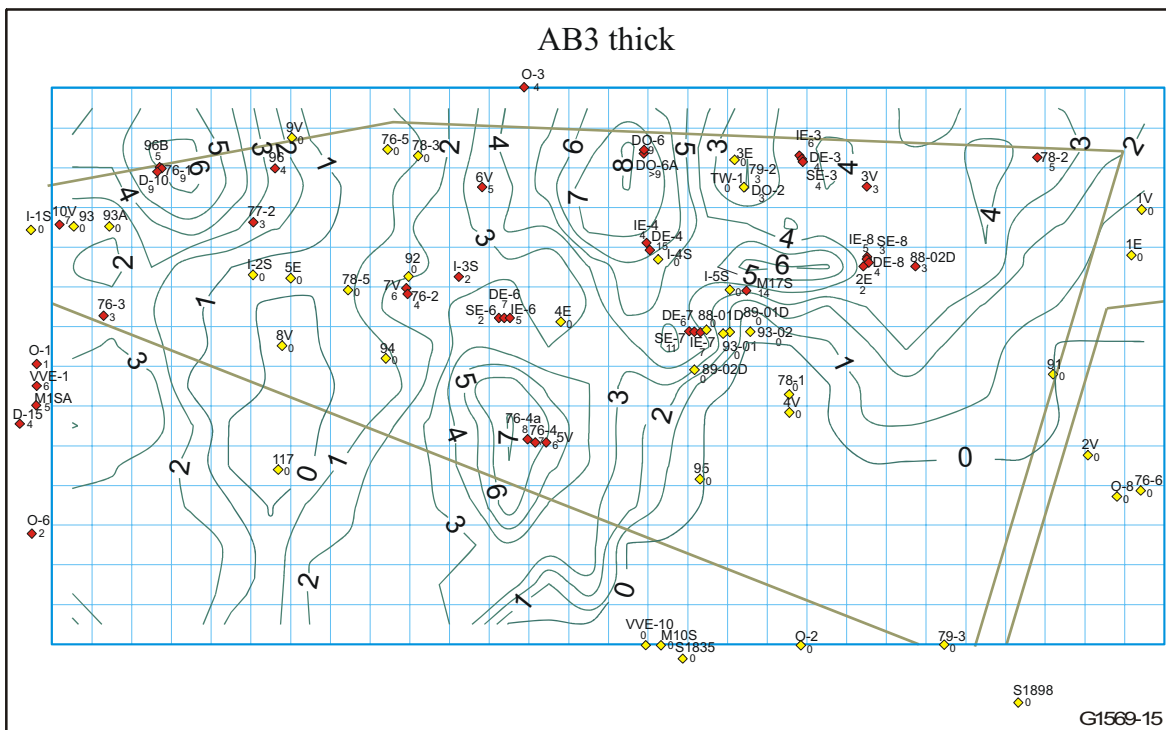
Figure 4-6. Kriged thickness (feet) of the A-B interbed for the second-level refined grid. Yellow symbols mark the locations where the A-B interbed is absent.
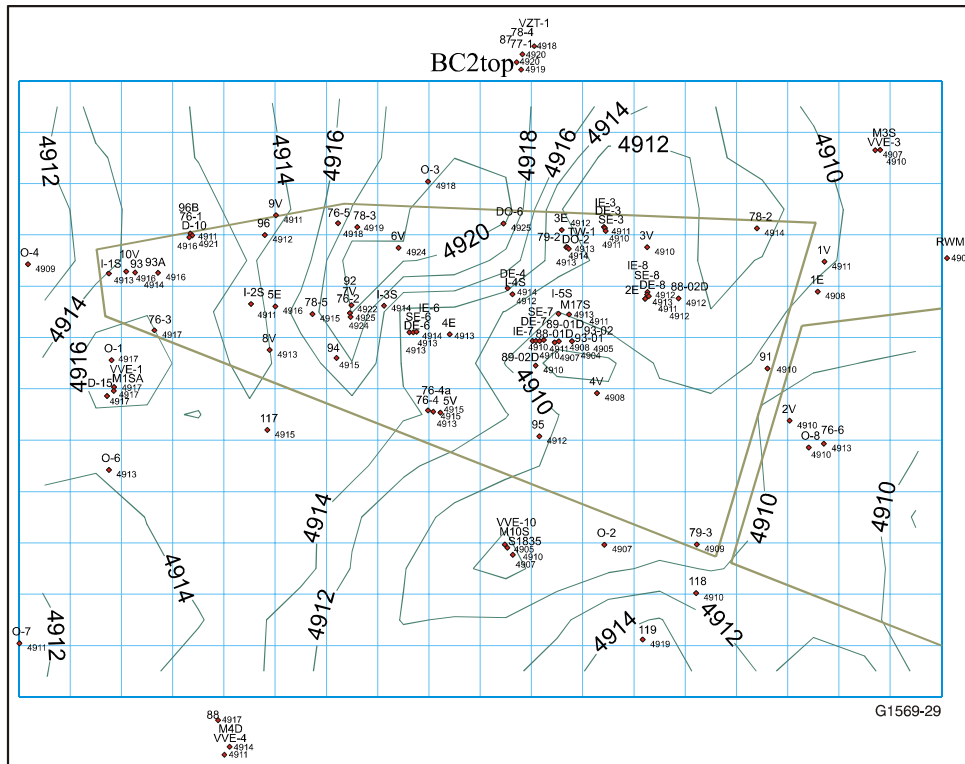
Figure 4-7. Kriged surface (feet above mean sea level) of the B-C interbed for the first-level refined grid.
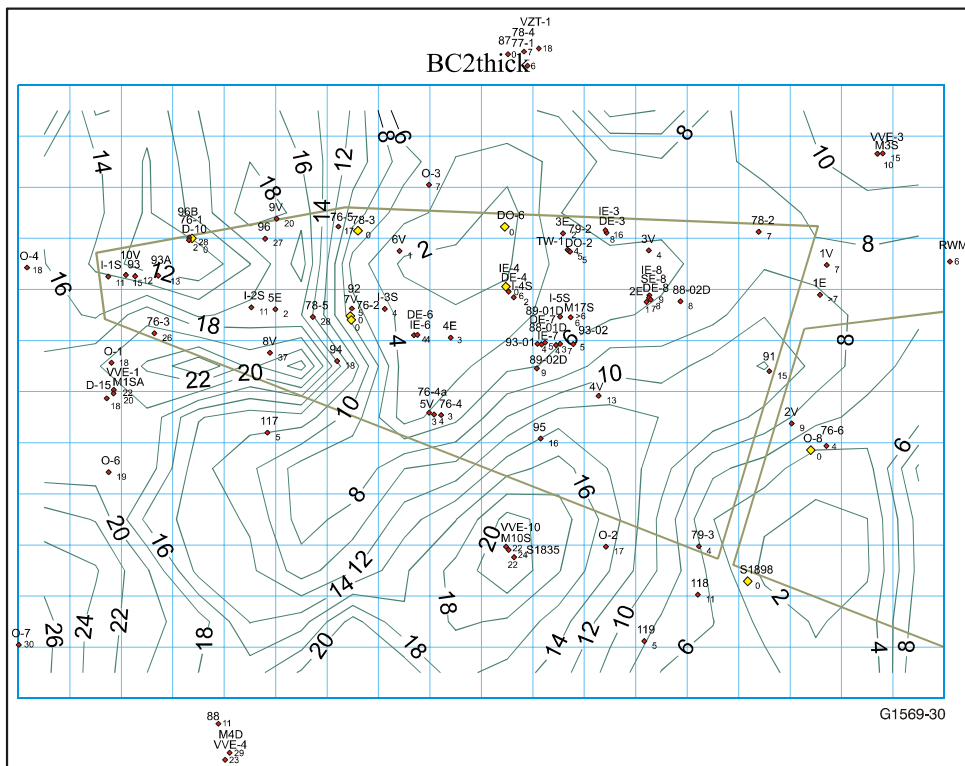
Figure 4-8. Kriged thickness (feet) of the B-C interbed for the first-level refined grid. Yellow symbols mark the locations where the B-C interbed is absent

Figure 4-9. Kriged surface (feet above mean sea level) of the C-D interbed for the base grid. Note the trough leading southeasterly from the Subsurface Disposal Area toward Well M6S.

Figure 4-10. Kriged thickness (feet) of the C-D interbed for the base grid.
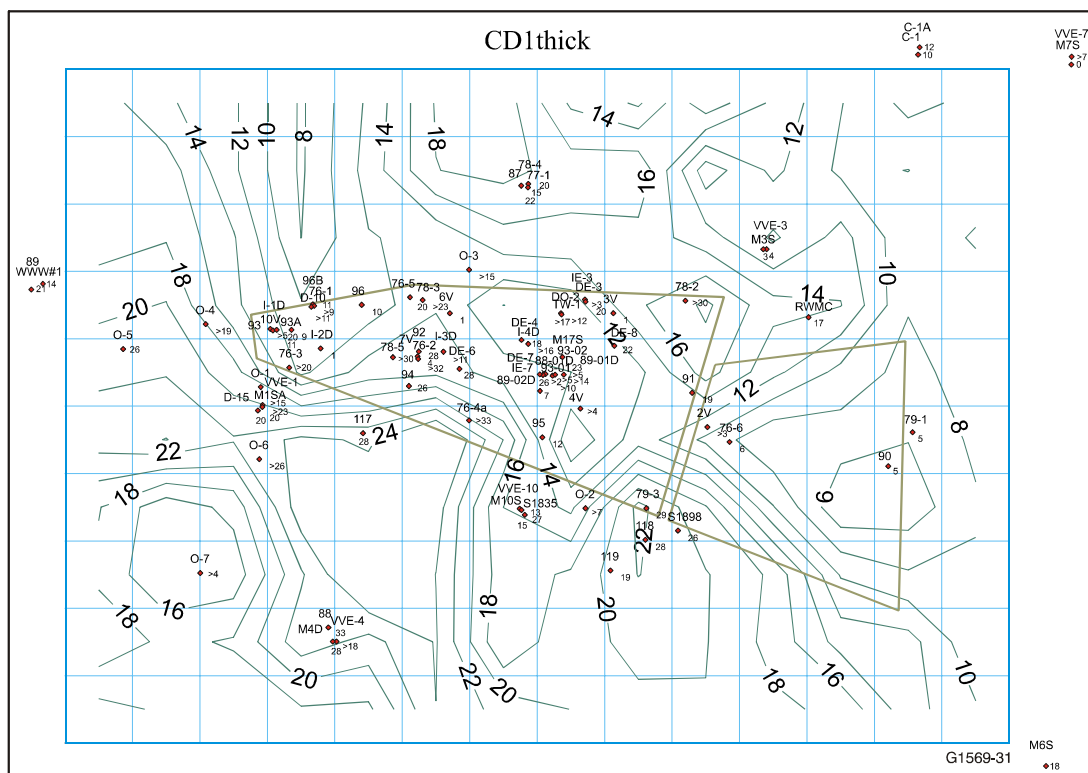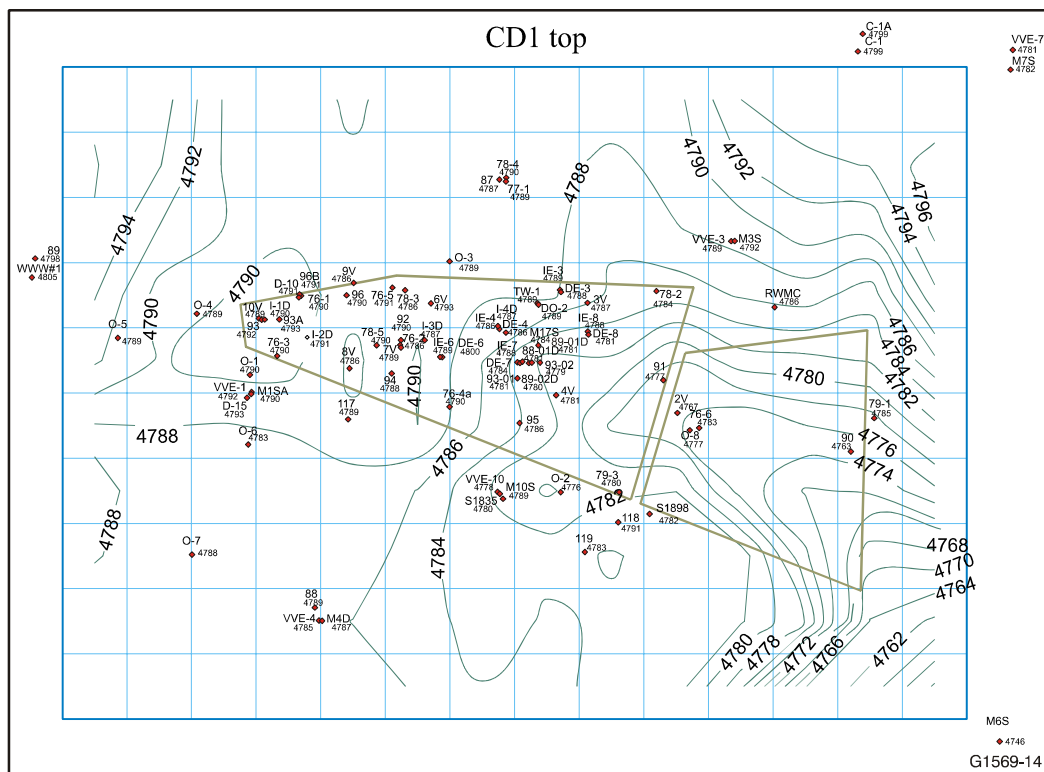
Both surface shape and thickness of each of the sedimentary features impact movement of water and contaminants through the subsurface. In particular, an interpreted trough or channel in the upper surface of the C-D interbed—that develops in the eastern half of the SDA and extends to the southeastern corner of the domain—influences water and contaminant movement above and through the C-D interbed.

4.3.3 Vertical Discretization

The next step in development of the RI/FS vadose zone model was vertical discretization of the base simulation domain. The kriged lithologic surfaces from Leecaster (2004) were used in conjunction with the horizontally discretized domains to create a conformable vertical grid. A minimum vertical grid size, maximum vertical grid size, and a geometric factor for increasing vertically adjacent gridblocks were assigned for each lithologic unit in the base vadose zone domain. Minimum grid size was 0.5 m (1.6 ft) for each of the sediment and basalt units, except for the A-B interbed, where a minimum grid size of 0.4 m (1 ft) was assigned. The geometric factor for the ratio between successive vertical gridblocks was a maximum of 1.5, which is a commonly used ratio to ensure numerical accuracy. Maximum vertical gridblock size was 3 m (9.8 ft) in the sediment units and 10 m (33 ft) in the basalt. Logic for adjusting vertical gridblock sizes was applied vertically at each horizontal gridblock location to allow for an optimum match of the gridblock interfaces to the kriged surface elevations. By having the same minimum gridblock size specified for both the sediment and basalt features, uniformity of gridblock sizes was ensured across lithologic interfaces. The total number of vertical gridblocks determined through this process was 80 at each horizontal location for the base vadose zone simulation domain. The upper surface of the vadose zone simulation domain was variable and was determined from the kriged elevation for the surficial sediment. The lower surface of the vadose zone simulation domain was assigned as a flat plane at the water table. As discussed previously, this assignment was correctly implemented for the RI/FS model as opposed to the ABRA model, where the plane was assigned at an elevation 27.5 m (90 ft) above the aquifer.

The logic for vertical grid discretization was different for the refined areas. Vertical discretization for the base domain was not adjusted further, based on the kriged elevations in the refined grids. Rather, the kriged elevations for the refined grids were compared to the conformable vertical discretization determined from the base grid, and then, as necessary, the material properties assigned in the refined domains were adjusted. This process resulted in smooth grid interfaces in the base domain and some degree of stair stepping in the refined grids. This can be seen in Figures 4-11 through 4-13, which show three-dimensional views of resulting grids, starting with the base grid and ending with the second-level grid refinement. These three-dimensional views are distorted both horizontally and vertically because the software (Visual Numerics 2001) that produces the views projects them onto a cube. The outline of the SDA is shown in each case projected just above the cube.

One special-case modification was made to lithologic assignments once the conformable grid was built. At a subset of grid locations in the second-level refined grid that represented the Low-Level Waste Pits (i.e., contiguous Pits 17 through 20), the region assigned as surficial sediment was extended downward 9.1 m (30 ft) from the top of the model to represent the approximate depth of these pits.

4.3.4 Hydrologic Properties

This section describes the assignment of hydrologic properties for the RI/FS model. Properties for the single-continua model are described first, with a comparison to measurements from core samples collected from wells installed after the assignments were made. Then additional properties necessary for the dual-continua simulations are described.
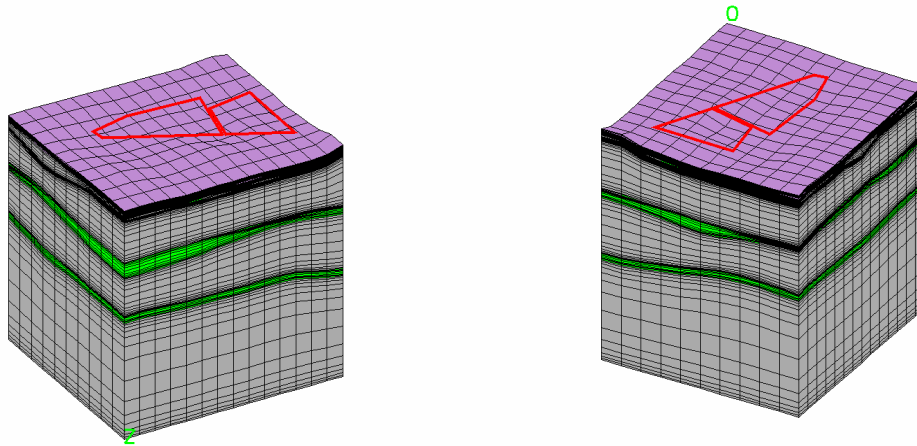
Figure 4-11. Southwest and northeast views of the base grid beneath the Subsurface Disposal Area showing vertical conformable gridding. The vertical extent shows the entire vadose zone simulation domain. Interbed grids are shaded green and fractured basalt grids are shaded gray (vertical exaggeration about a factor of 12). The A-B interbed appears black as a result of fine vertical discretization in these views.
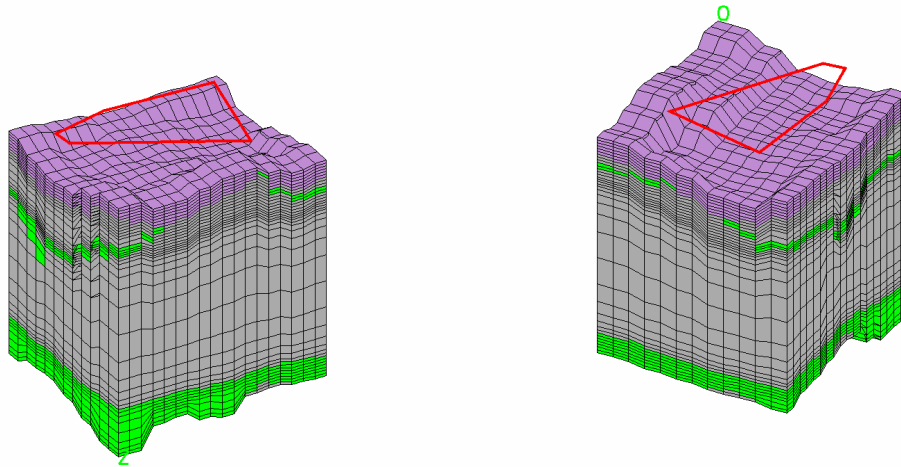
Figure 4-12. Southwest and northeast views of the first-level refined grid showing vertical conformable gridding. The first level of grid refinement extended to the base of the B-C interbed beneath the Subsurface Disposal Area (vertical exaggeration about a factor of 45).
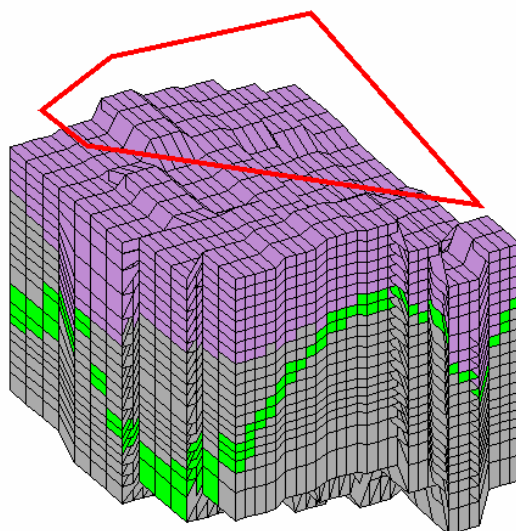
Z

Figure 4-13. Southwest view of the second-level refined grid showing vertical conformable gridding. The second level of grid refinement extended to the base of the A-B interbed beneath the Subsurface Disposal Area. Note the A-B interbed merging with the surficial sediment (vertical exaggeration about a factor of 120).

4.3.4.1 **Single Continua.** Hydrologic properties for porosity and permeability of the surficial sediment and the A-B interbed were assigned the same properties as the ABRA model (see Table 4-1) because no new information was available for these units. The fractured basalt porosity and vertical permeability were the same as the ABRA. The fractured basalt horizontal permeability was increased one order of magnitude from the value used in the ABRA and is now assigned a value of 90,000 mD. This increase was identified as part of the CCl$_4$ transport calibration (see Section 5.4).

Table 4-1. Parameterization of hydrologic properties and source of parameters for surficial sediment, A-B interbed, and fractured basalt.

Parameter	Permeability	Porosity	Source of Parameter
Surficial sediment	680 mD, isotropic	0.50 cm^3/cm^3 (Martian 1995)	Average of calibrated properties in Martian (1995)
A-B interbed	4 mD	0.57 cm^3/cm^3 (Magnuson and McElroy 1993)	Waste Area Group 3 modeling in Rodriguez et al. (1997)
Fractured basalt	300 mD vertical and 90,000 mD horizontal	0.05 cm^3/cm^3 (Magnuson 1995)	Magnuson (1995)

For all sediment in the simulation domain, van Genuchten (1980) equations were used to describe the relationship between water potential and moisture content. The Mualem (1976) equation was used to describe the relationship between saturation and relative permeability. The three-phase van Genuchten

constitutive equations, as adapted by Parker, Lenhard, Kuppusamy (1987) with slight modifications to the normalized saturation terms, implemented in TETRAD are

$$P_{c\_ow} = \frac{\sigma_{ow}\rho_w g}{\sigma_{gw}\alpha}\left[\left(\overline{S}_w\right)^{-1/\gamma}-1\right]^{1/\beta}$$

(4-1)

and

$$P_{c\_go} = \frac{\sigma_{go}\rho_w g}{\sigma_{gw}\alpha}\left[\left(1-\overline{S}_g\right)^{-1/\gamma}-1\right]^{1/\beta}$$

(4-2)

where:

P_{c_ow} and P_{c_go} are the interphase capillary pressure between the oleic-aqueous and gaseous-oleic phases, respectively

σ_{ij} is the surface tension between phases i and j

ρ_w is the density of water

α is the van Genuchten fitting parameter related to the inverse air-entry pressure

β is the van Genuchten fitting parameter related to the pore size distribution

$\gamma = 1 - \dfrac{1}{\beta}$.

The normalized saturation terms in Equations (4-1) and (4-2) are given by the following equations:

$$\overline{S}_w = \frac{S_w - S_{wr}}{1 - S_{wr}} \qquad \overline{S}_g = \frac{S_g}{1 - S_{wr}}$$

(4-3)

where S_{wr} is the irreducible aqueous-phase saturation. In this simulation study, there was never any oleic phase present; therefore, σ_{go} was set to zero and σ_{ow} and σ_{gw} were set to one. The effect was to make Equation (4-1) represent the capillary pressure between the aqueous and gaseous phases. This capillary pressure is the same as water potential in the absence of osmotic pressure. The term water potential expressed as centimeters of water will be used for the remainder of this report.

The relative permeability terms for the aqueous and gaseous phases implemented in TETRAD are

$$k_{rw} = \left(\overline{S}_w\right)^{1/2}\left[1-\left[1-\left(\overline{S}_w\right)^{1/\gamma}\right]^{\gamma}\right]^2$$

(4-4)

and

$$k_{rg} = \left(\frac{S_g - S_{gr}}{1 - S_{wr} - S_{gr}} \right)^{\!\!1/2} \left[1 - \left[1 - \left(\frac{S_g - S_{gr}}{1 - S_{wr} - S_{gr}} \right)^{\!\!1/\gamma} \right]^{2\gamma} \right]$$ (4-5)

where S_{gr} .is the irreducible gaseous-phase saturation.

Parameters assigned for the van Genuchten moisture characteristic curve were taken from GWSCREEN (Rood 1999) default values that were based on the average of four SDA surficial sediment samples that were hydraulically characterized and reported in Baca et al. (1992). The values for residual moisture content, van Genuchten α, and van Genuchten β were 0.142 cm^3/cm^3, 1.066 m^{-1}, and 1.523 (dimensionless), respectively. These values were the same as those used in the ABRA model. In the TETRAD model, the residual water saturation is entered rather than the residual water content. The S_{wr} calculated from the GWSCREEN defaults is 0.292. This value was used in the RI/FS model for all sediment features.

A Corey-type analytical equation was used to describe the constitutive relationships for basalt fractures. The equations implemented in TETRAD are

$$P_{c\_gw} = A_{gw} \left(1 - S_w \right)^{B_{gw}}$$ (4-6)

and

$$k_{ri} = A_i \left[\frac{S_w - S_{wr}}{1 - S_{sr}} \right]^{B_i}$$ (4-7)

where A_{gw}, B_{gw}, A_i, and B_i are fitting parameters for phase i (w aqueous, g gaseous, o oleic).

The moisture characteristic curve parameters for fractured basalt in the RI/FS model were slightly different from those used for the IRA and ABRA models. Two parameters in the analytic expression used for relative permeability of the fractured basalt portions of the simulation domain are the residual water saturation and a parameter that controls the amount of curvature. For the ABRA, the values for residual water saturation and the amount of curvature were 0.0 and 1.001, respectively. In the RI/FS model, these two parameters are assigned values of 0.01 and 2.0, respectively. The reason for the change was to take advantage of faster simulations that resulted from different parameters. Either parameterization results in rapid movement of water down through the fractured basalt, as discussed in Section 5.2. The simulation speedup from this change, approximately a factor of 2, resulted from less numerical overshoot and undershoot behavior for gridblocks near saturation in the iterative solution. The nearly linear slope of the water saturation relative-permeability curve—with the amount-of-curvature parameter set to 1.001—resulted in the iterative solution overshooting and then undershooting the correct solution when water saturation approached unity. These overshoots resulted in additional iterations to obtain a mass-convergent solution.

Kriged permeability fields for the B-C and C-D interbeds are shown in Figure 4-14. The kriged porosity fields for the B-C and C-D interbeds are shown in Figure 4-15. Only the most refined grid for each interbed is shown, although kriging results were provided in Leecaster (2002) for all base and refined grids. For these grids, the average of the kriged porosities for the B-C and C-D interbeds was 0.354 and 0.428, respectively.
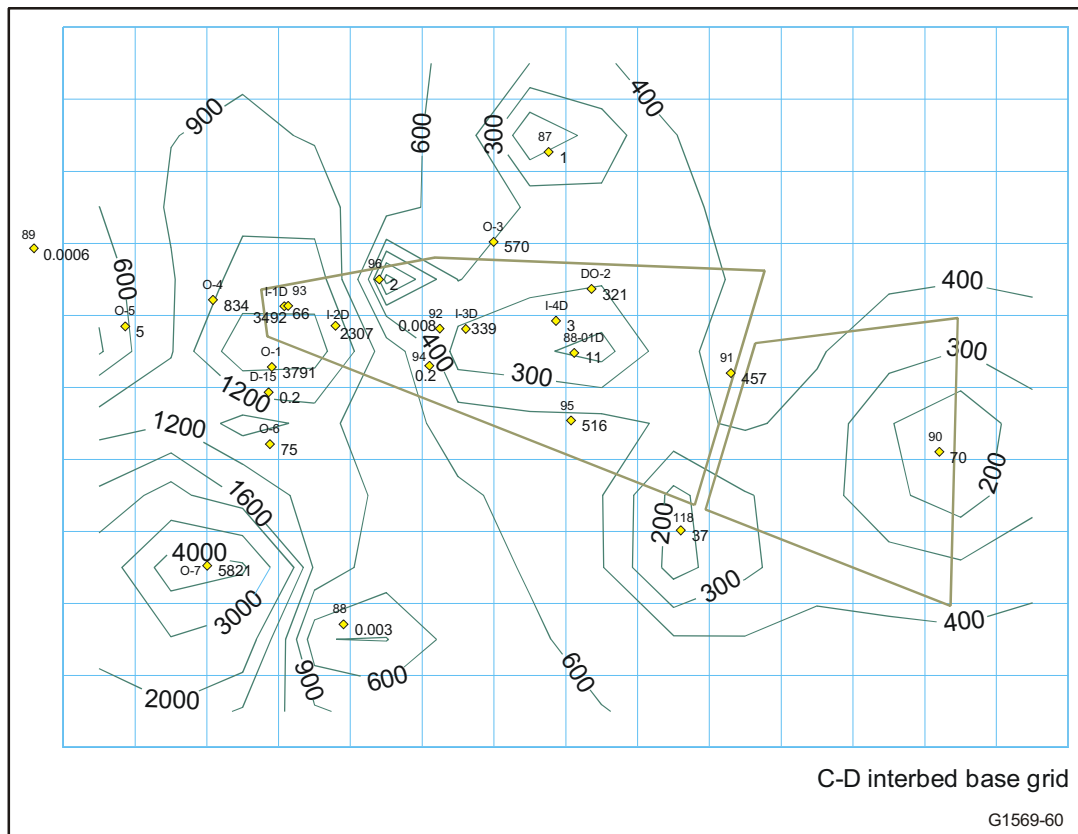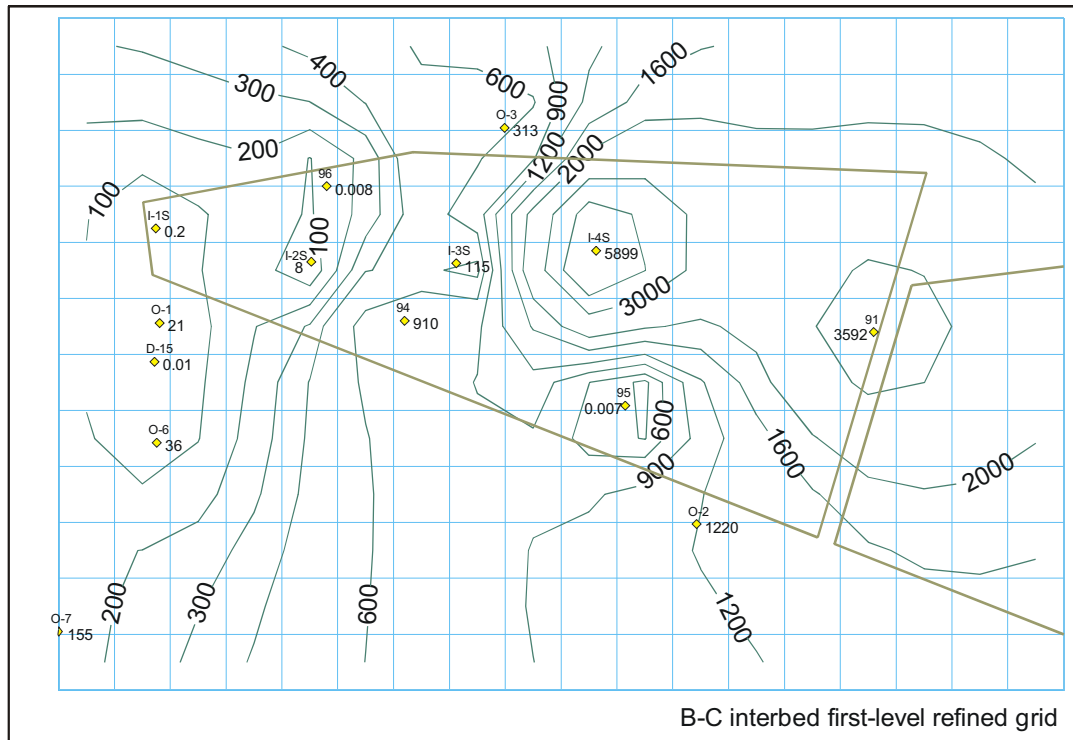
Figure 4-14. Kriged permeability (mD) for the B-C and C-D interbeds. Measured values from core samples are indicated at their respective locations.
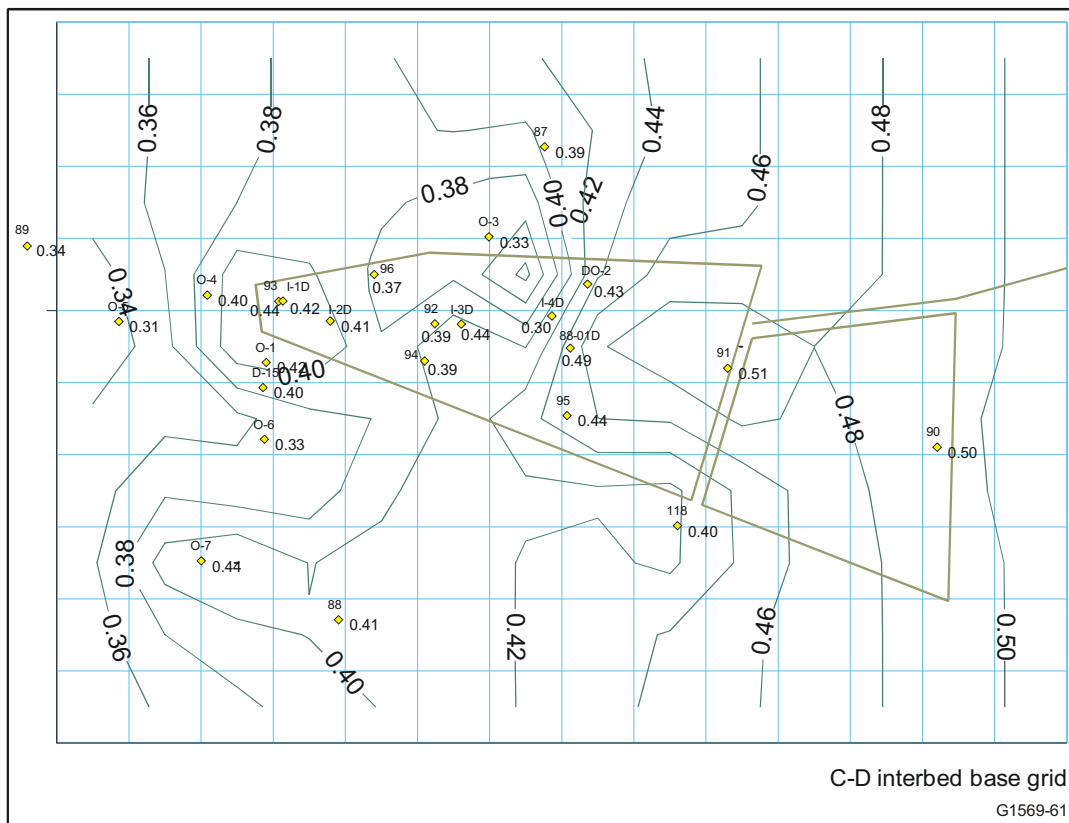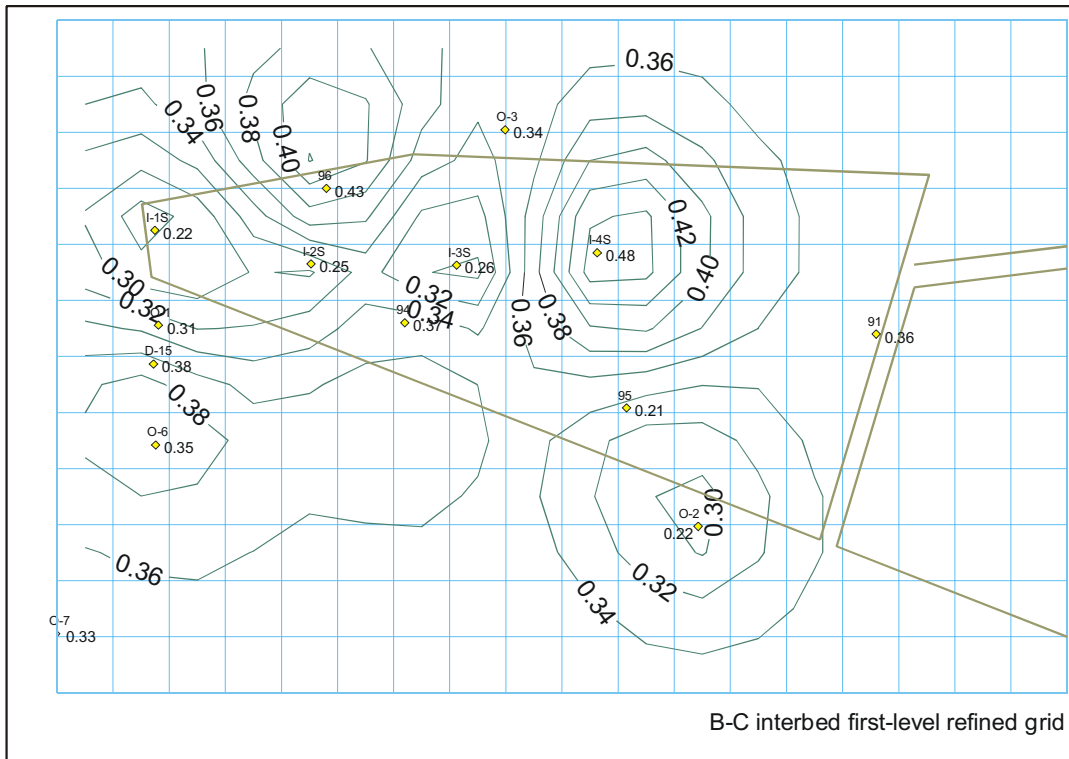
Figure 4-15. Kriged porosity for the B-C and C-D interbeds. Measured values from core samples are indicated at their respective locations.

Similar to the ABRA and IRA models, a low permeability value of 1 mD and a low porosity value of 0.05 were assigned to the top gridblocks representing both the B-C and C-D interbeds. This was accomplished by identifying the uppermost gridblock representing these interbeds in the grid with the greatest level of refinement, and then assigning the low-porosity and low-permeability value to that gridblock and the next two interbed gridblocks beneath it for a total of three low-permeability, low-porosity gridblocks. The three low-permeability, low-porosity gridblocks were used to emulate the thicker, single low-permeability, low-porosity gridblock used in the IRA model, and was necessary for the RI/FS model CCl_4 calibration (see Section 5.4). This low-permeability feature represents either a low-permeability sedimentary feature at the top of the interbeds or, more likely, a low-permeability feature caused by fine sediment infilling of fractures in the basalt immediately above the interbed. The latter occurs from deposition of entrained sediment fines as infiltration continues to occur through overlying basalt emplaced after formation of the interbeds. Inclusion of this low-permeability, low-porosity feature was necessary to achieve simulated conditions close to saturation at locations within the interbeds and to facilitate spreading of CCl_4 in the vadose zone as part of transport calibration.

An artifact of this assignment of low-permeability, low-porosity gridblocks is shown in Figure 4-16, which portrays the maximum simulated porosity for the first level of grid refinement for the B-C interbed. A variable number of vertical gridblocks represent the B-C interbed at each location. In Figure 4-16, the actual maximum simulated porosity, after the low-permeability, low-porosity gridblocks were implemented, was queried at each horizontal location. These values are posted in Figure 4-16 within each gridblock. Then these maximum values are contoured using the same intervals as in Figure 4-15. Two thinner regions of the B-C interbed show up in this plot. These are regions where the maximum porosity is 0.05 and occurs because the number of vertical gridblocks in these regions was three or less and, therefore, the entire interbed thickness was assigned the low-permeability, low-porosity value. Also posted in Figure 4-16 are the average value of the maximums (i.e., 0.316) and the overall average of all the B-C interbed (i.e., 0.206). These values show the effect of the assigned low-permeability, low-porosity gridblocks in lowering porosity. For clarification, although hydrologic properties were assigned differently in the low-permeability, low-porosity portions of the interbeds, distribution coefficients were assigned to these portions consistently with the rest of the interbeds.

4.3.4.1.1 *Comparison to Subsequent Measured Interbed Properties*—Core samples collected during drilling in Fiscal Year 2003 by the Operable Unit 7-08 Project were analyzed for hydrologic properties. These measured properties were compared to estimates for those locations based on kriging results from Leecaster (2002) and against sample results from nearby wells. These comparisons are included in Appendix E of this report. In general, measured porosities were lower than predicted porosities or the closest observed porosity from nearby wells. Agreement in permeability values was better, with the majority of observed values within the prediction interval from Leecaster (2002). The new results were closer to the kriged predictions than to the overall median, leading to a conclusion that modeling the spatial distribution of permeability was an improvement over predicting a single overall mean for the interbeds. Overall, the new measurements were within the range exhibited in previous hydrologic properties sampling. Statistical analysis of new permeability and porosity values are either within or below the kriged predictions for these properties in 60% of the samples. Small sample size makes analysis of results more uncertain, but, given that condition, the data do not suggest significant bias in the kriging results. Therefore, the kriging analysis in Leecaseter (2002) was supported by the new data.
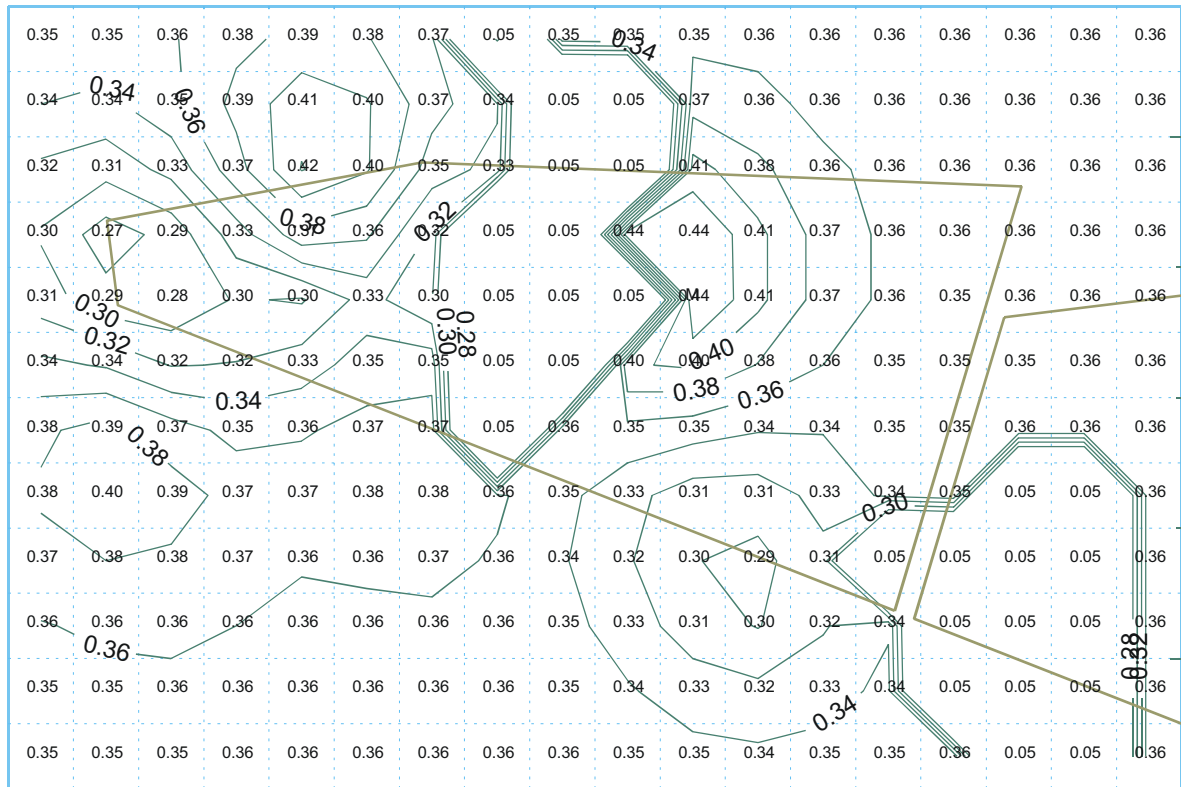
Figure 4-16. Maximum simulated porosity for the B-C interbed.

4.3.4.2   Dual Continua. Additional properties necessary to simulate water movement in dual-continua media (sometimes referred to as dual-permeability media) are described in this section. The second continuum in this case is the basalt matrix. This continuum becomes necessary in RI/FS modeling when there is substantial movement of water or contaminants from the basalt fractures into the basalt matrix. For contaminants that partition into the gaseous phase and undergo the more rapid process of diffusion, such as VOCs or C-14, simulating the second continuum of the basalt matrix becomes necessary. The hydrologic property values used for the basalt matrix are shown in Table 4-2.

Table 4-2. Parameterization of hydrologic properties and source of parameters for the basalt matrix for dual-continua simulations.

Parameter	Value	Source
Permeability	0.05 mD, isotropic	Magnuson (1995)
Porosity	0.10 cm^3/cm^3	Sondrup (1998)
van Genuchen alpha	3.840 m^{-1}	Bishop (1991)
van Genuchten N	1.474	Bishop (1991)
Residual water saturation	0.066	Bishop (1991)

A dual-continua simulation (Warren and Root 1963) consists of two separate continuums that are mathematically interconnected. In the dual-continua approach, there is a fracture domain overlapping with a matrix domain; therefore, there are twice as many gridblocks as in the single-continuum simulation. Because fractures run through the entire domain, it is necessary to assign sediment properties to those portions of the fracture domain that correspond to either surficial sediment or interbeds. A parameter called the characteristic matrix block length had to be increased in these same sediment blocks to ensure the flux of water was correctly represented through the combined sediment for both continua. For the basalt fractures, the characteristic matrix block length was set to 20 m (65.6 ft), which was an increase from the previously used value of 2 m (6.6 ft) in the IRA modeling. This increase was a result of calibration for the VOC model. In the interbeds, this characteristic matrix block length value was increased to 1,000 m (3,280.8 ft). The other dual-continua parameters remained the same as those for the ABRA. The transmissibility multiplier for fracture-matrix connections was left at 6.0 to result in three orthogonal sets of fractures with a connectivity factor of 0.5 in each of these three directions to allow partial contact between matrix blocks across the fractures.

4.3.5 Boundary Conditions

Boundary conditions are discussed first for the aqueous-phase portion of the model and then for additional gaseous-phase boundary conditions that were necessary for dual-continua simulations. Boundary conditions are generally discussed in terms of top surface, lateral sides, and bottom surface of the simulation domain.

4.3.5.1 Aqueous Phase

4.3.5.1.1 Surface—Aqueous-phase surface boundary conditions for the vadose zone model primarily consist of assigning water fluxes. Two types of water fluxes were imposed on the simulation domain, representing steady-state conditions and historical flooding conditions. Gaseous-phase boundary conditions of atmospheric pressure were also applied across the upper surface of the domain to prevent pressure building up in the subsurface during infiltration events*.*

As with the ABRA model, three infiltration rates were assigned to different regions inside the SDA for the RI/FS model. These rates represented a low-, medium-, and high-infiltration rate and were based on inverse modeling to neutron probe access tube measurements from Martian (1995). The spatial assignment was modified slightly, based on preliminary inverse modeling of moisture contents from Type B probes within the waste. The modeling is termed preliminary because it was determined the moisture content results were impacted by thermal influences and were not finalized. Despite the preliminary and qualitative nature of the inverse-modeling-infiltration estimates, the infiltration values for gridblocks containing Type B soil moisture and resistivity Probes Pit 5-TW1, MM2-3, and 741-08 were changed to the high-infiltration rate. Figure 4-17 shows the resulting distribution of the three assigned infiltration rates across the SDA.

In the RI/FS model, the value assigned for the high-infiltration rate was changed to 10.0 cm/year (3.9 in./year), rather than the 24.1 cm/year (9.4 in./year) value used in the ABRA model. The high ABRA infiltration rate of 24.1 cm/year (9.5 in./year) included the effect of three locations that had extremely high-infiltration rates due to neutron probe access tubes being located in areas of low topography (e.g., ditches) (Martian 1995). Excluding these elevated infiltration rates resulted in a high-infiltration rate of 10.0 cm/year (3.9 in./year), which was judged more representative of upper-bound water infiltration through waste in the SDA. The change in the high-infiltration rate from 24.1 to 10.0 cm/year (9.4 to 3.9 in./year) resulted in a reduction in the overall average assigned infiltration across the SDA from 8.5 cm/year (3.3 in./year) in the ABRA model to 5.0 cm/year (1.9 in./year) in the RI/FS model.
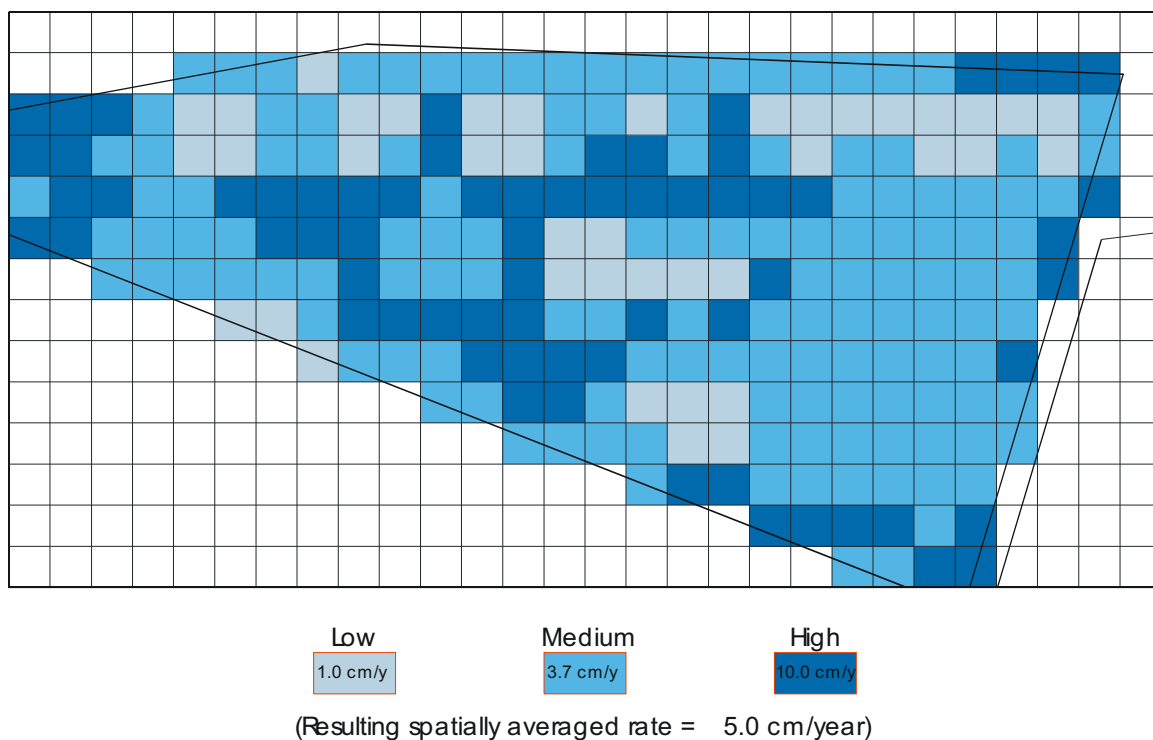
Figure 4-17. Spatially variable infiltration assignment for model domain inside the Subsurface Disposal Area.

The horizontal discretization of the SDA in the RI/FS model limits the extent that infiltration can be assigned on a site-specific basis. High infiltration through ditches or temporary collapse features that focus infiltration are beyond the scope of modeling. When considering transport from buried waste, infiltration rates need to be assigned based on what infiltration is likely to be through the waste, rather than infiltration through ditches near roads.

Outside the SDA, surface infiltration was assigned the same rate of 1 cm/year (0.4 in./year) that was used in ABRA modeling, based on Cecil et al. (1992).[b]

Three historical flooding events have occurred in the SDA and were included in the RI/FS model, essentially using the same method as the IRA model, but with slight differences caused by differences in gridding. Figure 4-18 shows locations where additional water was imposed at the surface for the 1962, 1969, and 1982 floods, respectively. Estimates of the amount of water that entered the SDA for each of the floods were taken from Vigil (1988) and are shown in Table 4-3. Each flood was assumed to last 10 days. The locations selected for the 1962 flood exclude gridblocks representing Pit 3, which was open and flooded in 1962. However, because the source-release model does not include the effect of the floods, this omission has no substantial effect.

---

b. This surface infiltration rate estimate is expected to decrease, based on an ongoing reevaluation by INL Site scientists.
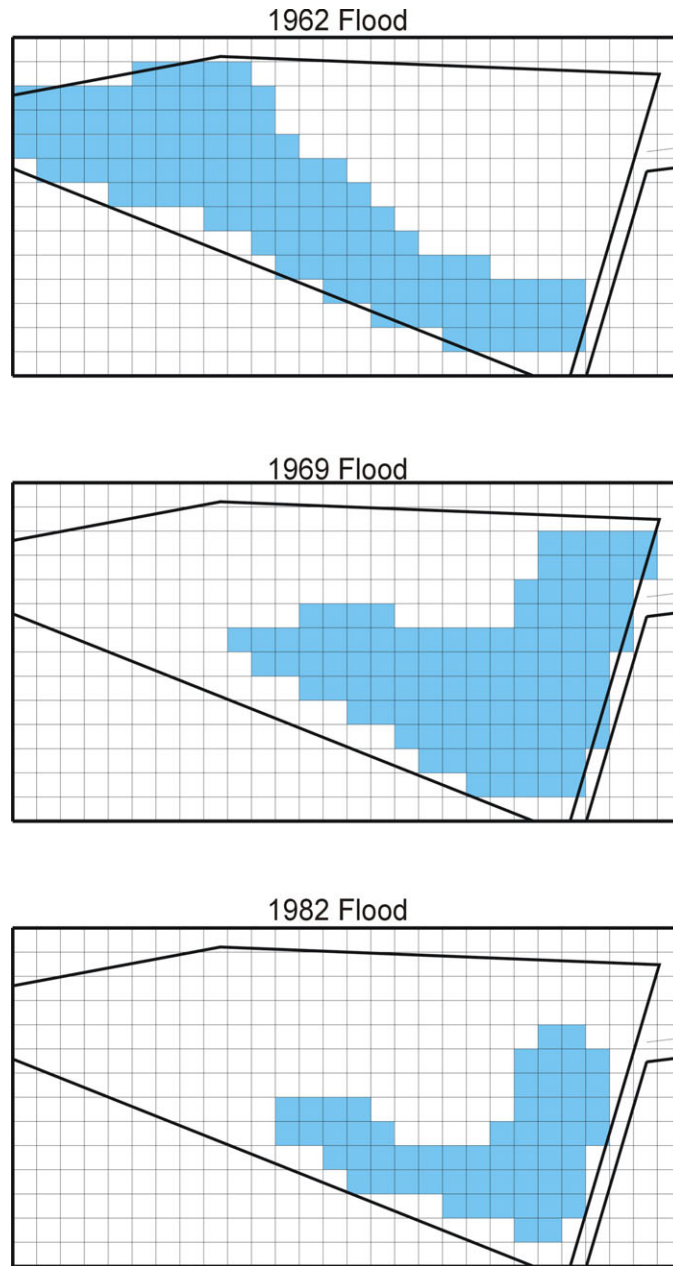
Figure 4-18. Locations of additional water applied during the 1962, 1969, and 1982 flooding events in the Subsurface Disposal Area in the second-level refined grid.

Table 4-3. Historical flooding volumes and application rates at the Subsurface Disposal Area.

Year	Estimated Volume (acre-ft)	Infiltration Rate (m/day)
1962	30	2.26×10^{-2}
1969	20	1.68×10^{-2}
1982	8.3	1.24×10^{-2}

4.3.5.1.2 ***Bottom***—The lower boundary of the vadose zone domain was assigned a vapor-static atmospheric pressure to emulate a water table condition. Water and tracer components (i.e., contaminants) in the water could freely advect out through the bottom boundary of the simulation domain.

4.3.5.1.3 ***Horizontal***—Default no-flux boundaries were allowed for all horizontal or lateral sides of the simulation domain. This was different from the ABRA, because there was no influence from the spreading areas included at the western boundary above the C-D interbed. Although the USGS tracer test (Nimmo et al. 2001) showed that there can be an influence above the C-D interbed, when that influence was included in the ABRA model, it only served to dilute simulated groundwater-pathway concentrations for long half-life radioactive contaminants that migrated strictly as dissolved in the aqueous phase. Therefore, the influence of the spreading areas was not included in the RI/FS modeling.

4.3.5.2 Vapor Phase

4.3.5.2.1 ***Surface***—Surface boundary conditions for the VOC transport model consisted of 1) a diffusion boundary condition, and 2) a fluctuating surface pressure to mimic changes in barometric pressure. The diffusion boundary condition, as implemented in TETRAD, allows molecular diffusion across grid boundaries. The diffusion occurs as if there was an extra external gridblock with fixed saturations and mole fractions. In this case, the external gridblock at land surface represents the atmosphere and was assumed to be completely saturated with air. This implies a zero concentration boundary for VOC vapor diffusion. The width of the external gridblock, which determines the diffusion length, is equal to the thickness of the uppermost gridblock in the model.

Barometric pressure fluctuations at land surface were included in the VOC model calibration, but were not included in the base-case simulations for the draft RI/BRA due to extremely long simulation times. In lieu of a fluctuating pressure, a constant pressure equal to atmospheric pressure was assigned at the upper surface of the domain. As discussed below in Sections 5.4.7 and 5.5.3, not including barometric pumping in the base-case simulations was conservative for the groundwater pathway as less mass escaped through the upper surface of the model domain. Implementation of the fluctuating atmospheric pressure boundary condition is described in Section 5.4.2.3.2.

4.3.5.2.2 ***Horizontal***—Diffusion boundaries similar to those assigned at land surface were also assigned to the lateral boundaries and were necessary because of the relatively small domain size compared to the size of the plume. First-type aerostatic pressure boundary conditions were also assigned to the lateral boundaries, based on a gradient of 0.012 kPa/m.

4.3.5.2.3 ***Bottom***—The bottom of the vadose zone model domain was prescribed the same water-table type boundary condition for the vapor-phase model as was prescribed for the dissolved-phase model (see Section 4.3.5.1.2). However, for the vapor-phase model, this condition was imposed on both the fracture and matrix domain, although the majority of the contaminant flux occurred in the fracture domain. This approach to assigning the bottom boundary conservatively lets contaminant mass advect out the bottom of the model domain without being influenced by contaminant mass already present in the aquifer.

4.3.5.2.4 ***Internal***—Both air injection during well drilling and gas removal due to vapor vacuum extraction operations were included in the dual-phase transport model. More than 40 wells have been drilled in the vicinity of the SDA using air as the fluid; this does not include reverse-air-circulation drilled wells, which typically recover most of the injected air. In wells drilled with air before 1994, air was injected at approximately 1,000 cfm and 250 psi to bring drill cuttings to the surface. A survey of SDA drill logs indicates that for most of the wells, circulation was partially or totally

lost below about 18.3 m (60 ft), which meant a large volume of air has been pumped into the subsurface of the SDA. Implementation of air-drilling in the model is described in Section 5.4.2.3.2.

Vapor vacuum extraction was also included in the model in much the same way air injection is handled. One difference with extraction is that phases are extracted rather than components. In this case, the gaseous phase is extracted, which is mostly air but can also include any water vapor or VOC vapor. Also, extraction is simpler because the extraction interval does not change the way an injection interval changes when a well is drilled. Three historic vapor extraction tests were included in the calibration and base-case simulations. They include the 1989 2-week test, the 1990 4-month test, and the 1993 Organic Contamination in the Vadose Zone Treatability Study. All of these tests pumped from Well 8901. In the base-case simulations, actual Operable Unit 7-08 operations from January 1996 through January 2005 were included, involving extraction from multiple wells. Base-case simulations also included future vapor extraction activities to the year 2010, assuming extraction from six wells for 10 months a year. Vapor extraction implementation in the model is described in Section 5.4.2.3.2.

4.3.6   Initial Conditions

Initial conditions for all simulations were obtained by assigning an initial water saturation of 50% to the entire simulation domain in both the single- and dual-continua domains. Then the simulation was run for 300,000 days (approximately 820 years) to let the system come into equilibrium. Water saturation in the C-D interbed was monitored to determine whether equilibrium had been obtained. Figure 4-19 shows the simulated time history of water saturation at a location at the top of the C-D interbed, located centrally beneath the SDA for a single-continuum domain. Initially, this gridblock wets up as excess water in the fractured basalt from above the interbed moves into and through the interbed. After the first approximate 50 years, change in saturation was negligible, indicating that steady-state conditions had been achieved.
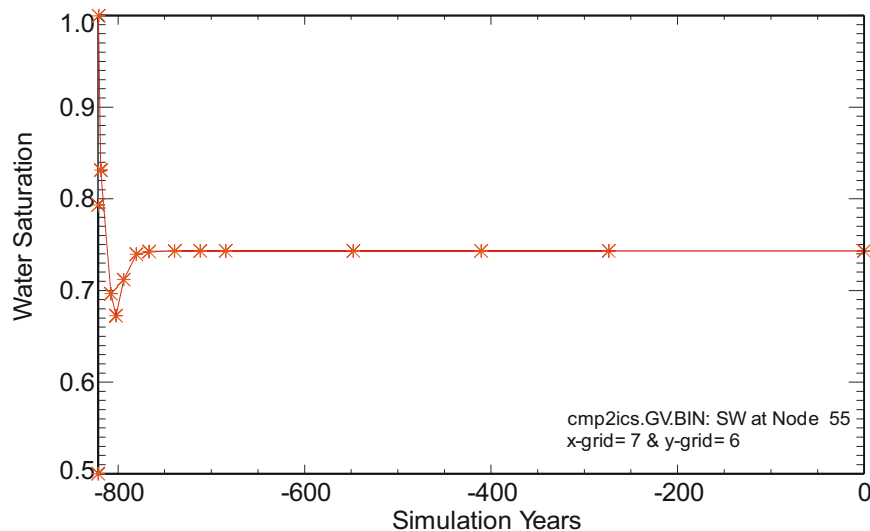
Figure 4-19. Initial condition simulation showing the time history of water saturation in the C-D interbed beneath the Subsurface Disposal Area.

For the dual-continua initial conditions simulation, results for the fracture domain are virtually identical to those in Figure 4-19. Water saturation in the matrix domain for the same horizontal location, but beneath the C-D interbed in the basalt, is shown in Figure 4-20. Water saturation in the basalt beneath the interbed takes considerably longer to stabilize. Even after the approximate 820-year simulation, there

is still a slight amount of drainage occurring, but, with the vast majority of the flow occurring in the fracture domain, this small residual change has a negligible effect on the simulation.
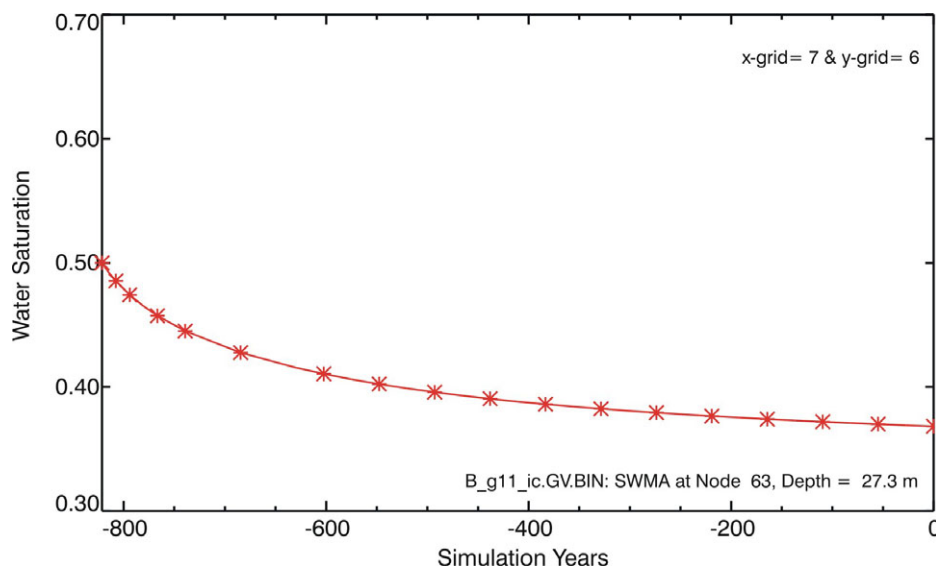
Figure 4-20. Initial condition simulation showing time history of water saturation in the basalt matrix beneath the C-D interbed.

4.3.7 Contaminant Transport

This section discusses transport in the vadose zone model. Topics addressed are transport mechanisms and their parameterization, contaminants that were simulated and how they were grouped, how these contaminants were introduced into the vadose zone model from the source-release model, and how contaminants were transferred out of the vadose zone model.

4.3.7.1   Transport Mechanisms. General mechanisms included in the transport model were advection, mechanical dispersion, diffusion, sorption, radioactive decay, buoyancy, and facilitated transport. Each is discussed in the following subsections.

4.3.7.1.1   Distribution Coefficients—Sorption was considered to follow linear, reversible isotherms that could be described using distribution coefficients, or K_ds. A K_d lumps all possible geochemical interactions into a single parameter. Because sorption was assumed not to occur within the fractured basalt portions of either the vadose zone or the aquifer, only sediment K_d values were necessary in the RI/FS model.

Table 4-4 provides K_ds used in the RI/FS model that were defined for use in Holdren and Broomfield (2004). Values for Ac-227, Am-241, Am-243, Pu-238, Pu-239, and Pu-240 were decreased from those used in the IRA and ABRA models to account for sieving of interbed material (Hull 2003). Values for Np-237 and uranium isotopes were increased based on additional batch equilibrium measurements from interbed cores (Leecaster and Hull 2004). The value for C-14 is different than the value in Holdren and Broomfield (2004) because the ABRA and RI/FS values were transposed in Holdren and Broomfield (2004). The C-14 value of 0.4 mL/g was selected from the conservative end of the range presented in Plummer, Hull, and Fox (2004). The value for chromium also is incorrect in Holdren and Broomfield (2004). Chromium was simulated in both the IRA and ABRA models with a K_d of 0.1 mL/g. This same value is used in the RI/FS model. Distribution coefficients for VOCs are discussed in Section 5.4.

Table 4-4. Sediment distribution coefficients for Operable Unit 7-13/14 remedial investigation and feasibility study simulations.

Contaminant	Distribution Coefficient (mL/g)
Ac-227	2.25E+02
Am-241	2.25E+02
Am-243	2.25E+02
C-14	4.00E-01
Cl-36	0.00E+00
I-129	0.00E+00
Nb-94	5.00E+02
Np-237	2.30E+01
Pa-231	8.00E+00
Pb-210	2.70E+02
Pu-238	2.50E+03
Pu-239	0.00E+00[a] and 2.50E+03[b,c]
Pu-240	0.00E+00[a] and 2.50E+03[b,c]
Ra-226	5.75E+02
Sr-90	6.00E+01
Tc-99	0.00E+00
Th-229	5.00E+02
Th-230	5.00E+02
Th-232	5.00E+02
U-233	1.54E+01
U-234	1.54E+01
U-235	1.54E+01
U-236	1.54E+01
U-238	1.54E+01
Chromium	1.00E-01
Nitrate	0.00E+00
Carbon tetrachloride	1.00E-03[d] and 2.20E-01[e]
Methylene chloride	1.00E-03[d] and 4.40E-03[e]
Tetrachloroethylene	1.00E-03[d] and 1.82E-01[e]

a. Mobile fraction source release, surficial sediment, and A-B interbed.
b. Mobile fraction in B-C and C-D interbeds.
c. Nonmobile fraction source release, surface sediment, and interbeds.
d. Volatile organic compounds in basalt.
e. Volatile organic compounds in surface sediment and interbeds.

4.3.7.1.2   Facilitated Transport—Plutonium mobility in the RI/FS model was based on research by Batcheller and Redden (2004). The source-term model accounts for the mobile fraction leaving the waste form. In the vadose zone model, this released mobile fraction of plutonium is then allowed to migrate with a 0 K_d through the surficial sediment and A-B interbed. The B-C and C-D interbeds are assigned the sediment K_d value of 2,500 mL/g from Table 4-4. Facilitated transport is considered for Pu-239 and Pu-240, but not for Pu-238. As discussed in Section 5.1.3 of the draft RI/BRA, Pu-238 is not simulated with a colloidal fraction based on the work of Batcheller and Redden (2004), which showed that certain processes at Rocky Flats Plant could produce colloids. The fraction of Rocky Flats Plant plutonium that is mobile is 3.7% for the RI/FS model. Pu-238 was not simulated with a colloidal fraction because it would have been separated as an impurity and would not have gone through the high-temperature processes that generate colloids.

4.3.7.1.3   Other Transport Parameters—A variety of additional parameters were required to implement the vadose zone transport model. These additional parameters were particle density, diffusion coefficients, tortuosity, and decay half-lives. Particle density was assigned the typical value of 2,700 kg/m^3 for sediment (Freeze and Cherry 1979). This was the same value assigned in the ABRA model. Because sorption was assumed not to occur in fractured basalt, the grain density assigned for that portion of the simulation domain did not matter.

Diffusion of contaminants within the aqueous phase was assigned the common literature value of 1×10^{-5} cm^2/second (Freeze and Cherry 1979). This was the same value assigned in the ABRA model. The restriction of diffusion caused by tortuosity also was included, based on a relationship from Lerman (1988) that was used to describe diffusion, as shown in Equation (4-8):

$$D = D_o \theta_w^2 \tag{4-8}$$

where:

D =   diffusion in the porous medium (length^2/time)

D_o =   free-water diffusion coefficient (length^2/time)

θ_w =   volumetric moisture content (unitless).

Various formulations of diffusion and tortuosity are implemented in different simulators. In the TETRAD simulator, diffusion within the aqueous phase is treated, as shown in Equation (4-9):

$$D_{eff} = \frac{\theta_w D_o}{\tau_w} \tag{4-9}$$

where:

D_{eff} =   effective diffusion coefficient (length^2/time)

τ_w =   aqueous-phase tortuosity.

The aqueous-phase tortuosity term for TETRAD was then calculated, as shown in Equation (4-10):

$$\tau_w = \frac{1}{\theta_w} \, .$$

(4-10)

The end result of this application is to have greater tortuosity values assigned for drier conditions. Single tortuosity values were assigned for each sedimentary feature and for fractured basalt. Tortuosity values were determined using Equation (4-10) and are given in Table 4-5. Tortuosity values were based on the average simulated water content for each sedimentary feature from the base RI/FS model (shown in the second column of Table 4-5), and either the assigned porosity for surficial sediment and the A-B interbed or the average of the kriged values for the B-C and C-D interbeds (shown in the third column of Table 4-5). Fractured basalt has low-simulated moisture content, approximately the same as the assigned residual water saturation; therefore, fractured basalt was arbitrarily assigned a high aqueous-phase tortuosity.

Table 4-5. Aqueous-phase tortuosity values for the remedial investigation and feasibility study model.

Material	Average Simulated Water Saturation (cm³/cm³)	Assigned or Average Porosity (cm³/cm³)	TETRAD Tortuosity (dimensionless)
Surficial sediment	0.59	0.50	3.4
A-B interbed	0.70	0.57	2.5
B-C interbed	0.68	0.354	4.2
C-D interbed	0.63	0.428	3.7
Fractured basalt	—	—	100

Vapor-phase tortuosity values were used as a calibration parameter. Initially, tortuosity values were calculated from an empirical expression derived by Millington (1959) and later modified to improve agreement between model results and observed data. Later, the Millington formulation was directly implemented in the TETRAD code so the tortuosity values could vary spatially and temporally. This, however, was unsuccessful in improving agreement between model results and observed data, and ultimately the tortuosity values were assigned constant values for each material type. This is discussed in detail in Section 5.4.

Longitudinal and transverse dispersivity values of 5.0 and 0.5 m (16.4 and 1.6 ft), respectively, were assigned in the vadose zone transport model. The longitudinal value is the same as was used in the IRA and ABRA models and was originally based on inverse modeling from the large-scale infiltration test (Magnuson 1995). The transverse dispersivity value of 0.5 m (1.6 ft) is the same as was used in the ABRA model and was assigned by using the modeling rule-of-thumb that the transverse dispersion is one-tenth the longitudinal dispersion (Freeze and Cherry 1979). The 5.0-m (16.4-ft) longitudinal value is smaller than would be assigned using the general rule-of-thumb that the dispersivity should be approximately one-tenth of the domain size (Gelhar 1986). In the absence of calibration data (e.g., breakthrough of a nonsorbing contaminant), no basis is available to substantially adjust the dispersivity values from those used in the ABRA model. Ideally, higher concentrations would result for pulses of mobile contaminants because the lower dispersivity would produce a sharper simulated front. For a long, slow release (e.g., a solubility-limited release of a lower-mobility contaminant), the lower dispersivity ideally would result in a slightly later first arrival. However, because dispersion control consisting of higher order solutions that limit numerical dispersion was not used in the TETRAD

simulation, the relative contribution of numerical dispersion compared to simulated dispersion in the vadose zone model is unknown. No dispersivities were assigned for vapor-phase transport because diffusion would dominate the dispersive fluxes.

Half-lives for each radioactive COPC were assigned based on literature values (GE 1989) and are given in Table 4-6.

Table 4-6. Half-lives for radioactive contaminants of potential concern used in the remedial investigation and feasibility study groundwater-pathway simulations.

Contaminant	Half-life (years)
Ac-227	2.18E+01
Am-241	4.32E+02
Am-243	7.38E+03
C-14	5.73E+03
Cl-36	3.01E+05
I-129	1.57E+07
Np-237	2.14E+06
Pa-231	3.28E+04
Pb-210	2.23E+01
Pu-238	8.78E+01
Pu-239	2.41E+04
Pu-240	6.57E+03
Ra-226	1.60E+03
Tc-99	2.13E+05
Th-229	7.34E+03
Th-230	7.70E+04
Th-232	1.41E+10
U-233	1.59E+05
U-234	2.45E+05
U-235	7.04E+08
U-236	2.34E+07
U-238	4.47E+09

4.3.7.2   Contaminant Groupings. Contaminant release and subsurface transport were simulated for 31 contaminants, which were grouped into 11 groups of contaminants for fate and transport simulation. This same grouping was used in source-term simulations (Anderson and Becker 2006). Members of a decay chain are assigned to the same group. Isotopes in the chain with a half life of more than 1 year were included explicitly in simulations, while contaminants with shorter half-lives were assumed to be in equilibrium with long-lived parents. Grouping for COPCs and long-lived decay-chain members is defined in Table 4-7 as Groups 1 through 5. Some of the long-lived daughter products were not identified as COPCs in the ABRA (Holdren et al. 2002), but were included to confirm that they pose no unacceptable risk and to assess sensitivity and uncertainty. Some RI/FS sensitivity cases reduce release of the parent nuclide and thus increase ingrowth of the daughter in the waste zone.

Table 4-7. Contaminant groups for Operable Unit 7-13/14 simulations.

Simulation Group	Group Name	Contaminants in Group[a]	Description	Basis for Group
Group 1	Am-241	Am-241, Np-237, U-233, and Th-229	Pu-241 decay chain	Neptunium series beginning at Am-241, created by weapons' production.
Group 2	Am-243	Am-243, Pu-239, U-235, Pa-231, and Ac-227	Am-243/Pu-239 decay chain	Am-243 to Pu-239 (both created primarily by weapons' production) to actinium series initiated by U-235.
Group 3	Pu-240	Pu-240, U-236, Th-232, and Ra-228	Pu-240 decay chain	Pu-240 to U-236 (created primarily by weapons' production) to thorium series initiated by Th-232.
Group 4[b]	Pu-238	Pu-238, U-234, Th-230, Ra-226, and Pb-210	Pu-238 decay chain	Pu-238 (created primarily by reactor operations) to U-234 to mid-uranium series.
Group 5[b]	U-238	U-238, U-234, Th-230, Ra-226, and Pb-210	Uranium decay chain	Uranium series initiated by U-238 (primarily from weapons' production).
Group 6	Tc-99	Tc-99, I-129, and Cl-36	Mobile activation products	Created by reactor operations.
Group 8[c]	C-14	C-14	Mobile activation product	Requires dual-phase simulation. Created by reactor operations.
Group 9	Nb-94	Nb-94 and Sr-90	Fission and activation products	Surface pathways only. Created by reactor operations.
Group 10	Nitrate	Nitrate (as nitrogen) and chromium	Toxic chemicals	Nonvolatile (single-phase), nonradioactive chemicals. Nitrate is contained primarily in Series-745 sludge from Rocky Flats Plant. Mobile with no decay. Chromium is a possible model performance indicator.
Group 11	Volatile organic compound	Carbon tetrachloride, Methylene chloride, Tetrachloroethylene, and 1,4-dioxane	Toxic chemicals in organic sludge	Volatile (dual-phase) nonradioactive chemicals. Scaled in the Ancillary Basis for Risk Analysis.

a. Simulations include contaminants that are not contaminants of concern. The additional contaminants are decay-chain products or are useful for other reasons (e.g., comparison to performance assessment modeling and interpreting model performance and uncertainty).
b. Groups 4 and 5 both contain U-234, Th-230, Ra-226, and Pb-210.
c. Group 7 contained tritium, which was dropped as a model performance indicator.

4.3.7.3   Source Release Implementation in Vadose Zone Model. The vadose zone model implements the temporal source-term release (Anderson and Becker 2006) spatially in an automated fashion, using a PV-Wave program. PV-Wave is a commercial visual data analysis software program that was used for pre and post-processing model results (see Appendix B). In addition to being spatially distributed, the source release is also distributed vertically at each assigned location based on the number of gridblocks within the surficial sediment at that location. Once released, the contaminants are allowed to migrate with the simulated water movement. Anderson and Becker (2006) divided the SDA into 18 source areas for modeling contaminant release and transport of radionuclides and chemicals, except for C-14, which used nine source areas. The source-release model was linked with the vadose zone model through assigned infiltrations that resulted from assigned spatially variable surface water fluxes. Individual assigned water fluxes for each gridblock within the 18 source areas were averaged for use in the source-release modeling. Figures 4-21 through 4-23 show the resulting average infiltration for each source area. Figure 4-23 is necessary because areas representing Pits 4, 5, and 10 were reduced for VOC simulations, based on disposal location knowledge.
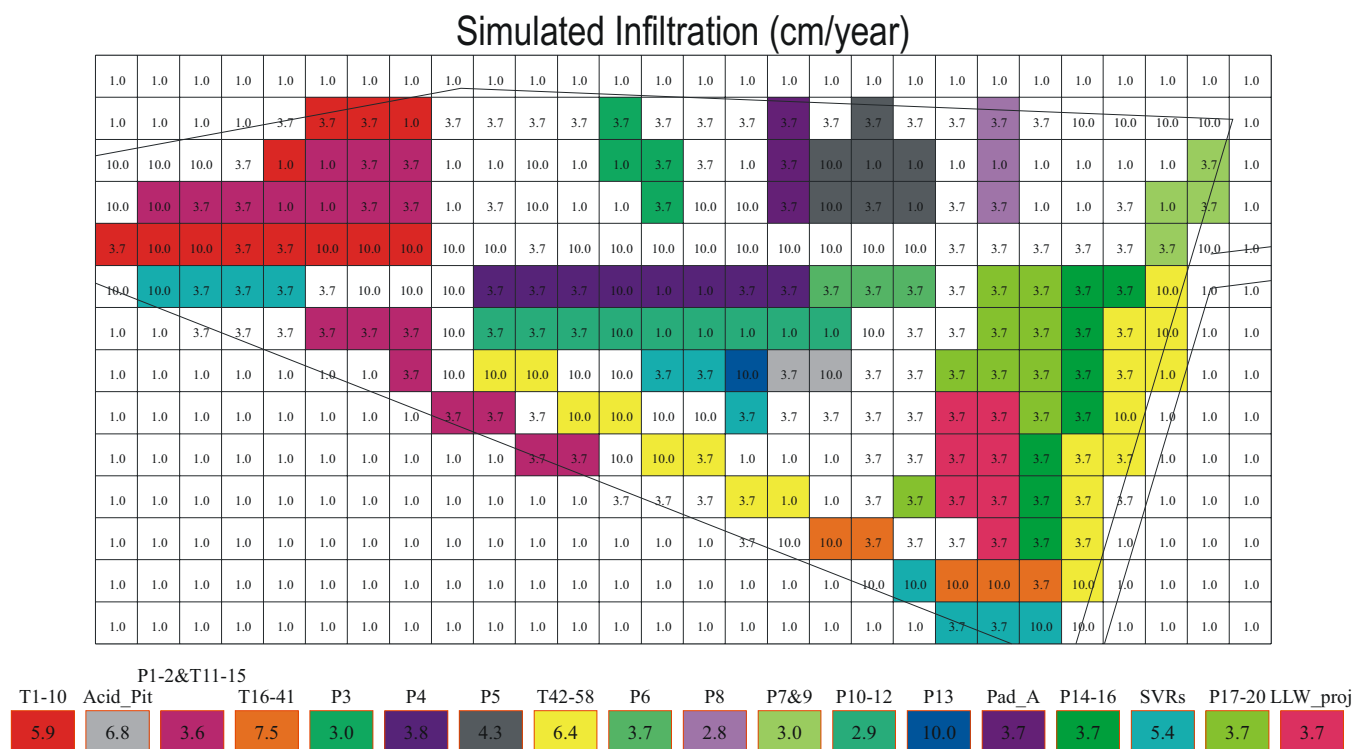
Figure 4-21. Subsurface Disposal Area infiltration rates with averages by source area for dissolved-phase contaminants.

Simulated Infiltration (cm/year)

SVR12	TR58	SVR17	SVR20	TR52	pre-60	60-66	67-83	post-83
3.7	6.8	6.8	3.7	3.7	10.0	3.9	6.8	5.6

Figure 4-22. Subsurface Disposal Area infiltration rates with averages by source area for carbon-14.

Simulated Infiltration (cm/year)

T1-10	Acid_Pit	P1-2&T11-15 T16-41	P3	vP4	vP5	T42-58	P6	P8	P7&9	vP10-12	P13	Pad_A	P14-16	SVRs	P17-20	LLW_proj
5.9	6.8	3.6	7.5	3.0	2.8	1.0	6.4	3.7	2.8	3.0	3.8	10.0	3.7	3.7	5.4	3.7

Figure 4-23. Subsurface Disposal Area infiltration rates with averages by source area for volatile organic compound contaminants.

The general methodology for distributing contaminant release vertically at each location was to

1. Start release in the first gridblock that was at a depth of greater than 1.5 m (4.9 ft) below the top surface. This was equivalent to maintaining a clean overburden thickness of 1.5 m (4.9 ft).

2. End release one gridblock above the bottommost surficial sediment gridblock. This maintained a clean underburden thickness of at least 0.5 m (1.6 ft).

Two exceptions were implemented to these general rules. First, Pad A releases were assigned to the second gridblock beneath the surface for the three gridblock locations representing Pad A. The reason for this assignment is that Pad A waste is actually buried above grade, and the second gridblock down was the closest approximation that could be made in the model; the uppermost gridblock was being used to assign infiltration rates. Second, Acid Pit sources were assigned at the bottommost gridblock to approximate burial at the bottom of an open pit. The Low-Level Waste Pit is not listed as an exception for waste zone thickness assignments. As discussed previously, the surficial sediment at the grid locations representing the low-level waste disposal pits were deepened to 9.1 m (30 ft) when the lithologic assignments for the gridblocks were made. With this approach, the general methodology correctly assigned waste for low-level waste streams that went into the active pit.

4.3.7.4   Interface from Vadose Zone Model to Aquifer Model. The primary result used in the aquifer model is the flux of water and contaminants from the bottom of the vadose zone simulation domain. These time-varying fluxes were extracted, using a PV-Wave program, from each gridblock in the base vadose zone domain to build a table of flux values that was used as input into the aquifer model.

4.4   Aquifer Model

The objective in the aquifer simulation was to evaluate three-dimensional advective-dispersive transport in a predominantly horizontal flow regime. The aquifer flow model had been updated in the ABRA to take advantage of additional water level data (Whitmire 2001). For the RI/FS model, the aquifer domain was again revised to extend the domain farther to the south and west. This extension ensured that risk isopleths at the 1.E-05 level were closed within the simulation domain. Permeability values were not adjusted to improve agreement between simulated and observed water levels for this extension to the ABRA domain. Appendix C contains complete details of this aquifer domain extension. A summary of the domain extension is included here.

The domain was extended westward so that it was twice the width of the ABRA aquifer model domain. The domain was extended southward so that it was three times the height (in a north-south sense) of the ABRA aquifer model domain. Hydrologic properties in the extended domain were taken from McCarthy et al. (1995). The low-permeability region immediately south and southwest of the SDA was retained. Prescribed head boundary conditions were based on interpolated water levels measured in 2003 and were applied with an assumption of hydrostatic conditions. Porosity was assigned uniformly for the entire model domain and had the same value as in the ABRA model, 0.06. Simulated velocities in the new extended domain are compared to the old domain in Appendix C. With the larger domain, monitoring wells with considerably lower water levels got included in interpolating boundaries, and the head gradient imposed across the domain was greater, leading to increased velocities away from the SDA. However, with retention of the low-permeability region in the SDA vicinity, the velocities remain slow, keeping aquifer simulation results essentially consistent with the ABRA.

4.4.1 Transport Properties

Simulating transport in the aquifer model was straightforward compared to the vadose zone. The flux of water and contaminants from the vadose zone model were applied as an upper-boundary condition in the refined portion of the model. The remainder of the upper surface of the model and the bottom surface of the model were treated as no-flux areas. Contaminants could advect through external boundaries.

Because it was assumed that sorption did not occur within fractured basalt, and only fractured basalt was simulated in the aquifer portion of the model, no K_d values were necessary in the aquifer portion of the model. Diffusion was included and was parameterized the same as in the vadose zone model. Tortuosity was assigned using the same approach as in the vadose zone model (i.e., following the approach in Lerman [1988]), with a resulting value of 16.7 (dimensionless). Dispersion was parameterized differently in the aquifer model than in the vadose zone model. Longitudinal and transverse dispersivity values of 9 and 4 m (30 and 13 ft) were assigned, respectively. These values were the same as those used in the ABRA model. Similar to the vadose zone model, assigned dispersivity values are small relative to the one-tenth domain size general rule of thumb.

4.4.2 Aquifer Permeability Comparison

Six single well pump tests were conducted in Fiscal Year 2003 (Jolley 2003) on aquifer monitoring wells that previously did not have transmissivity estimates. These additional transmissivity tests serve as a check on the assigned permeability values. The additional tests were for Wells M11S, M13S, M14S, M15S, M16S, and M17S. Figure 4-24 shows results of the additional tests posted at the well locations, along with previous estimates. Only Well M17S comes close to the region assigned in the aquifer model as a low-permeability zone, and it has an estimated transmissivity of 500 ft^2/day. This transmissivity is lower than that of many of the upgradient wells, but is not in the range of the assigned value for the low-permeability region south and southwest of the SDA. The additional well tests do show that assigned permeability for the region upgradient of the SDA is reasonable.

4.4.3 Comparison to Estimated Aquifer Flow Directions

An evaluation of flow directions in the aquifer in the local vicinity of the SDA was conducted for the Operable Unit 7-13/14 Project (see Appendix D for complete evaluation). In this evaluation, water levels were evaluated over time using three-point solutions with groupings of three wells to determine flow directions as a function of time. The flow directions are plotted using a rose diagram, similar to that normally used to plot wind velocities. Figure 4-25 shows the comparison of simulated and interpreted flow directions. Wells used for the comparison that are within the refined domain are labeled with blue text, and well triplets used to determine direction over time are labeled with purple text. The rose diagrams are plotted at the approximate centroid of each triplet. The larger the rose diagram in the figure, the larger the separation between wells and the less likelihood of errors due to very low gradients, which increase likelihood of measurement error influencing results. The interpreted flow directions often show a slight southeastward component beneath the eastern half of the SDA and beneath the Transuranic Storage Area, indicating some agreement with flow directions from the RI/FS aquifer model.

Regarding the RI/FS aquifer flow model, general flatness of the water table in the immediate SDA vicinity, coupled with an apparent low-permeability region to the south-southwest of the SDA, precludes completely accurate determination of groundwater flow directions. The presence of a low-permeability region is hypothesized on an increasingly compelling body of supporting evidence and evaluations. This hypothesis also is consistent with the interpretation by Roback et al. (2001) that RWMC is in a low-permeability region extending southerly from the Lost River Range onto the INL Site.
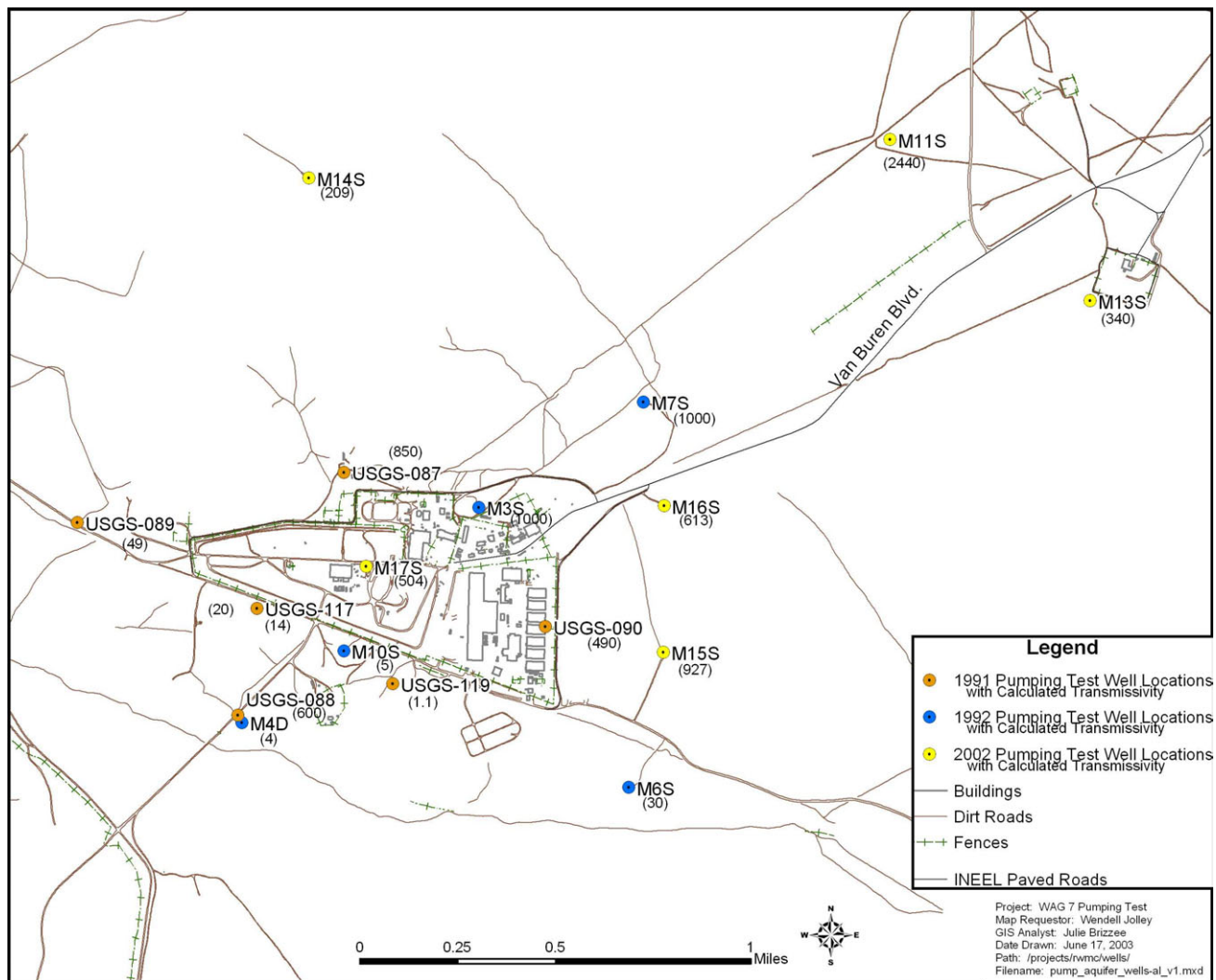
Figure 4-24. Transmissivity (feet^2/day) from pump tests in the Subsurface Disposal Area vicinity (from Jolley [2003]).
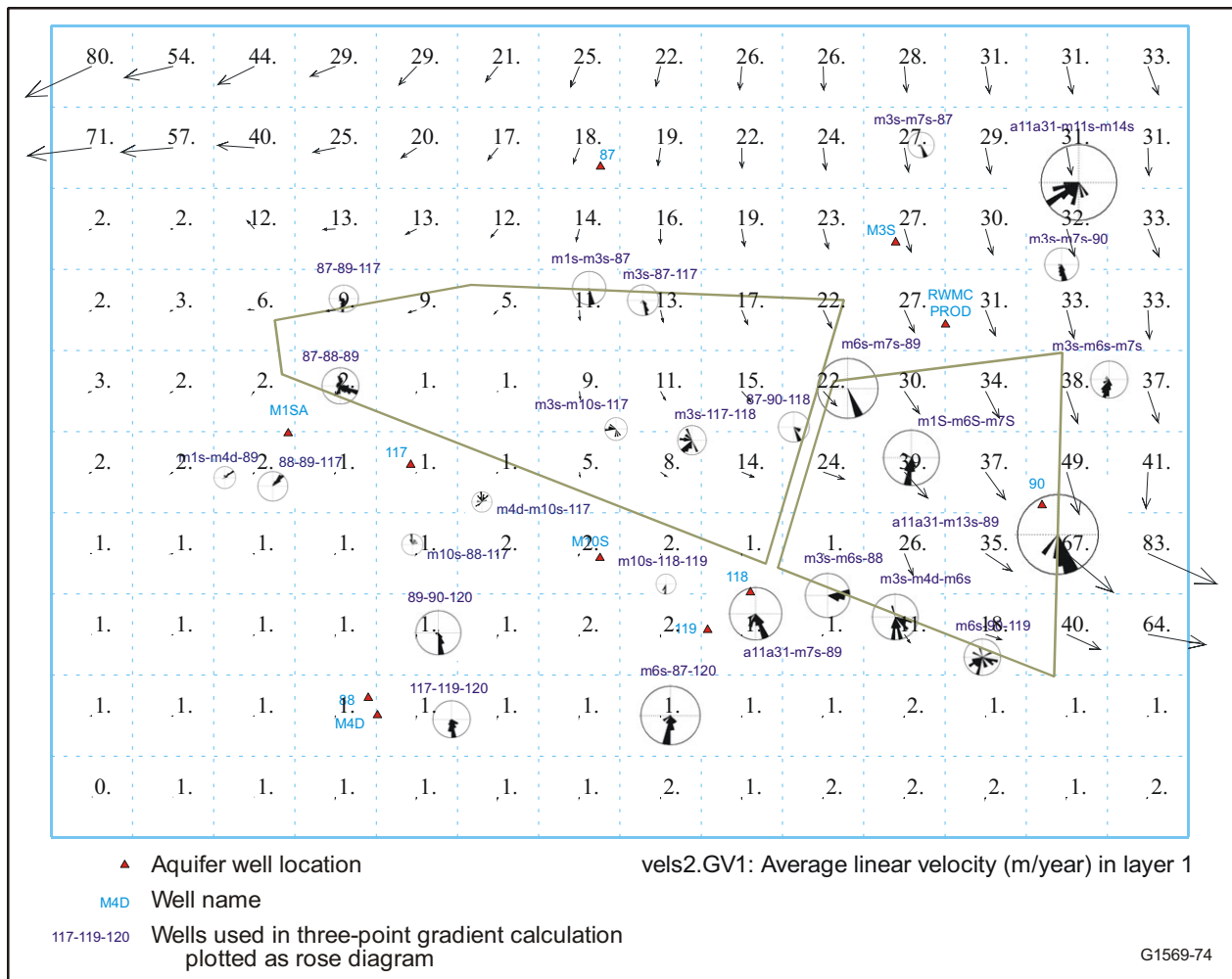
Figure 4-25. Simulated groundwater average horizontal linear velocities (meter/year) for the first-level refined grid in the aquifer domain compared to interpreted aquifer flow directions as a function of time.

An assumption in the aquifer model was that flow was predominantly horizontal. This assumption was implemented by assigning permeability as uniform in the vertical direction at each location in the model and by assuming that pressure within the aquifer was in hydrostatic equilibrium with the water table at each location, including the assigned boundary pressures. The only location where slight vertical velocities resulted was within the refined area of the aquifer domain where additional water is applied from the vadose zone model. Figure 4-26 shows the simulated vertical average linear velocity at each gridblock in the upper layer of the aquifer model for just the refined area. Comparing velocities in the vertical direction to those in the horizontal direction (Figure 4-25) shows that velocities were predominantly horizontal, even in this refined area, which received some additional water flux from the vadose zone model. The effect of increasing the fractured-basalt anisotropy ratio to 300:1 can be seen where vertical velocities at the top of the aquifer were larger in the southeastern corner due to water getting concentrated during transit of the vadose zone by the topography of the C-D interbed channeling water to the southeast. This does not substantially impact simulation results as discussed in Section 6.4.7.

0.01	0.00	0.06	0.07	0.09	0.10	0.11	0.01	0.00	0.06	0.00	0.00	0.01	0.04
0.00	0.01	0.06	0.08	0.06	0.11	0.10	0.03	0.11	0.01	0.01	0.01	0.01	0.00
0.00	0.03	0.07	0.06	0.09	0.03	0.02	0.02	0.05	0.01	0.01	0.01	0.01	0.00
0.00	0.14	0.02	0.01	0.05	0.03	0.02	0.00	0.03	0.06	0.01	0.01	0.04	0.00
0.01	0.07	0.02	0.00	0.05	0.00	0.01	0.25	0.03	0.50	0.02	0.02	0.03	0.00
0.10	0.20	0.09	0.09	0.08	0.09	0.07	0.02	0.18	0.28	0.76	0.08	0.05	0.01
0.03	0.01	0.02	0.24	0.06	0.18	0.06	0.13	0.72	0.03	0.12	0.47	0.11	0.01
0.04	0.03	0.01	0.04	0.17	0.18	0.10	0.10	0.08	0.03	0.00	0.02	0.25	0.08
0.18	0.07	0.05	0.16	0.03	0.11	0.03	0.06	0.04	0.02	0.00	0.00	0.19	0.38
0.02	0.05	0.04	0.03	0.01	0.09	0.09	0.02	0.05	0.01	0.01	0.19	0.31	3.55

avels.GV1: Vertical average linear velocity (m/year) in layer 1

Figure 4-26. Simulated vertical average linear velocities (m/year) for the uppermost layer in the first-level refined grid in the aquifer domain.

4.4.4   Link to Operable Unit 10-08 for Future Aquifer Model Development

The impact of increased velocities, from extending the aquifer simulation domain and reinterpolating head boundaries, demonstrates uncertainty in the aquifer simulation. Overall, treatment of water movement in the aquifer is simplistic with water movement being primarily two-dimensional with limited three-dimensional contaminant movement. Improving representation of the movement of water and contaminants within the aquifer is the scope of the Operable Unit 10-08 Groundwater Modeling Project (DOE-ID 2004). The Operable Unit 10-08 groundwater model is currently under development to represent INL-scale transport, considering contaminant loading from all facilities concurrently. The potential effect of commingled plumes from INL Site facilities is one primary reason this model is being developed. This Site-wide model is being developed using information from the disciplines of geology, hydrology, contaminant chemistry, isotope chemistry, and thermal transport. This Site-wide model will use contaminant loading to the aquifer from individual waste area group facility models and has the stated goal of being consistent with local velocities from waste area group models if they are based on local information (e.g., the Operable Unit 7-13/14 model's representation of the low-permeability zone).

5. SIMULATIONS SUPPORTING PARAMETERIZATION OF THE OPERABLE UNIT 7-13/14 MODEL

This section describes simulations that were performed during development of the updated Operable Unit 7-13/14 model. These simulations augment and support selection of parameters in the model. In some cases, this is simply a comparison of simulated to observed concentrations for noncontaminant of concern constituents. In other cases, such as CCl₄, there was a substantial effort devoted to calibrating the model to mimic observed distributions of contaminants.

5.1 Measured Interbed Moisture Comparisons

This section presents a comparison of measured and simulated interbed water potentials. A summary of the deep tensiometer monitoring network is provided, followed by a description of the calibration process where the van Genuchten parameters of the interbeds were slightly modified from those in the ABRA model. Lastly, the final RI/FS model results are compared in terms of simulated fluxes through the interbed and fluxes estimated from measured water potentials and measured soil hydrologic properties.

5.1.1 Advanced Tensiometer Monitoring Network

Advanced tensiometers were developed for use in the deep vadose zone to monitor infiltration, distribution, and drainage of water under unsaturated conditions. A network of these instruments was installed in the vadose zone beneath and adjacent to the SDA at depths ranging from 2.7 to 117 m (9 to 385 ft) below land surface. Locations of 26 wells that comprise the advanced tensiometer network are shown in Figure 5-1. Installation of the deep tensiometer network and monitoring results are summarized in the draft RI/BRA report (Section 2).

Overall, the monitoring network has been active primarily through a series of drier than average years with no large transient events and a general drying trend. Even so, there have been transient events recorded as a result of infiltration inside the SDA. Averaged water potentials indicate wetter conditions inside the SDA compared to outside, especially for the B-C interbed. The influence of higher surface infiltration inside the SDA is dampened at the depth of the C-D interbed. These observations are used in the next section where model results are compared to observations.

5.1.2 Remedial Investigation and Feasibility Study Base Model Comparison to Deep Tensiometer Monitoring Network Matric Potentials

To compare TETRAD-simulated results with measured water potentials, the TETRAD-simulated results have to be converted to comparable units. The TETRAD simulator internally tracks water pressure in absolute pressure (kPa) and outputs pressure in the same unit. The field-measured water potentials are customarily measured and reported in pressure units of centimeters of water of tension. To convert from absolute pressure units to water potential units also requires outputting the TETRAD-simulated absolute air pressure (kPa). Using the relationship that capillary pressure is equal to pressure of the wetting fluid minus pressure of the nonwetting fluid, and conversions between pressure units of kPa and centimeters of water, the conversion is

$$P_c \ (cm \ H_2 0) = \left[P_w - P_g \ (kPa) \right] \left[10.1678 \frac{cm \ H_2 0}{kPa} \right]$$

(5-1)

where:

P_c =   capillary pressure or water potential (cm H$_2$0)

P_w =   simulated pressure of wetting fluid, water in this case (kPa)

P_g =   simulated pressure of nonwetting fluid, gas in this case (kPa).
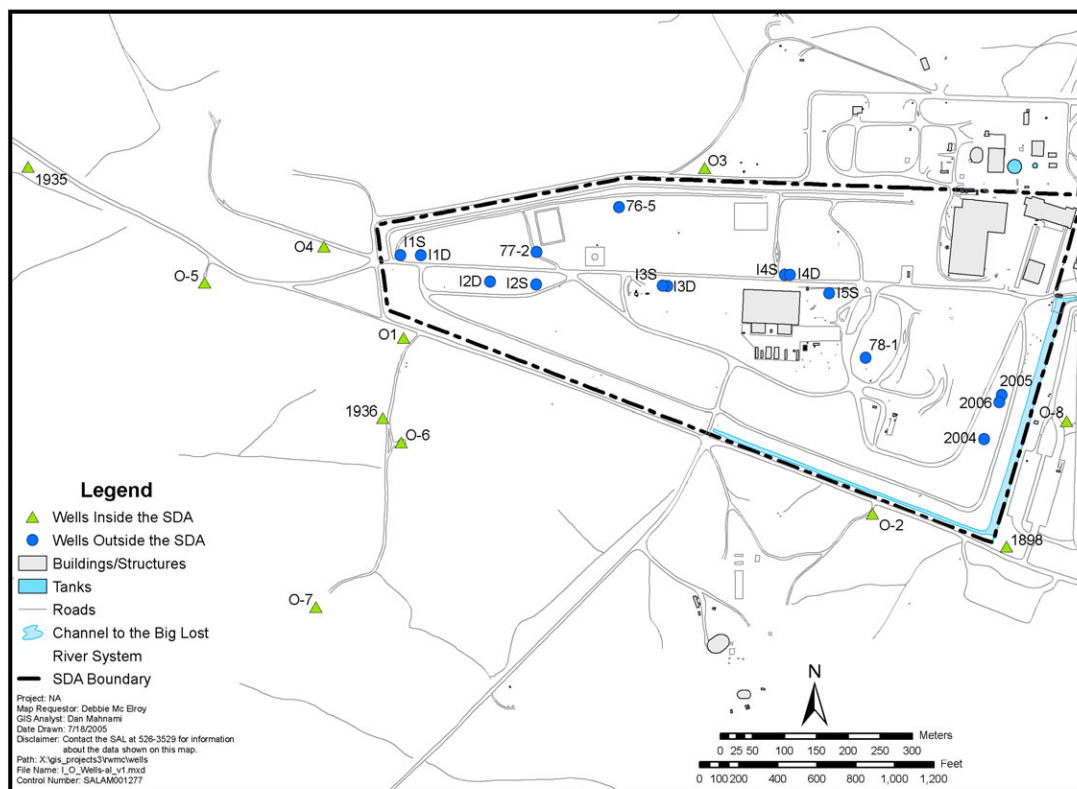
Figure 5-1. Location of advanced tensiometers in the Subsurface Disposal Area.

The final base-case model results for simulated water potentials in the B-C and C-D interbeds are shown in Figure 5-2. The 4/2001 simulation time shown was chosen because it was sufficiently after the 1982 flood for simulated water potentials to be constant and also adequately close to the comparison period from where potentials were averaged in McElroy and Hubbell (2003). Contour lines in the figure were generated with a PV-Wave processing routine and represent the maximum water potential at any location vertically across the identified interbed, with maximum in this case meaning the wettest condition. For comparison, averaged water potentials from McElroy and Hubbell (2003) are shown in Figure 5-2 at their respective locations. The principal observation that can be drawn from the simulated results is that they show good agreement to the observed trend of wetter conditions inside the SDA compared to outside. The simulated results also show a slight easterly shifting of the simulated wettest area in the C-D interbed, which is likely due to the general slope of this interbed. Lastly, there is a water collection point in the extreme southeastern corner of the C-D interbed, where saturated conditions developed, as can be seen by the water potential of zero at this location. This water collection point is caused by further horizontal movement of water above the interbed being constrained by the boundaries of the simulation domain, but is shown elsewhere in this report to not significantly influence transport results (see Section 6.4.7).

Figure 5-2. Simulated water potential (cm H$_2$0) for the base case with comparison to averaged measured water potentials from McElroy and Hubbell (2003).

Preliminary to obtaining the final base-case model results, a set of simulations were conducted to try to improve agreement between simulated and observed water potentials from the advanced tensiometer monitoring network. In these simulations, the van Genuchten sorting parameter N, used for sediment portions of the vadose zone model, was varied from 1.323 to 2.423. These simulations also required simulating 300,000 days for obtaining steady-state initial conditions. Simulated matric potentials were extracted at locations that correspond to the deep tensiometer monitoring network and were compared statistically to averaged water potentials from McElroy and Hubbell (2003). This comparison included calculating root mean squared error, mean average error, and mean error relative to measured values and tabulating the lowest, highest, and average water potential from the maximum water potential extracted vertically through simulated interbed gridblocks at each horizontal location for both the B-C and C-D interbeds and the overall average for all interbed gridblocks. Ideally, the lowest and highest simulated interbed water potential would mimic the range of the observed water potential range, which was about -320 and -30 cm, respectively, from McElroy and Hubbell (2003). Table 5-1 shows a comparison of simulated water potentials and calculated comparison statistics for a range of values for the different values of the van Genuchten N parameter.

Table 5-1. Simulated water potential statistics (cm H_2O) for a range of van Genuchten N values for the B-C and C-D interbeds.

Name	van Genuchten N	Low	High	Average of Maximums	Overall Interbed Average	Root Mean Squared Error	Mean Average Error	Mean Error
B-C Interbed								
observed		-320	-30					
r3	1.323	-259	0	-98	-309	92	77	45
r1 (base)	1.523	-279	-6	-115	-312	83	70	28
r5	1.723	-279	-16	-124	-305	79	65	19
r7	2.023	-268	-25	-128	-288	76	62	13
r9	2.423	-253	-32	-129	-262	73	60	11
C-D Interbed								
observed		-360	-109					
r3	1.323	-407	0	-141	-413	134	107	95
r1 (base)	1.523	-397	0	-155	-412	125	99	84
r5	1.723	-375	0	-159	-402	123	97	81
r7	2.023	-347	0	-159	-379	124	98	82
r9	2.423	-322	-1	-155	-343	127	101	86

Increasing the van Genuchten N parameter results in an improvement in the root mean squared error, mean average error, and mean error for the B-C interbed, and slightly worsens agreement between simulated and observed water potentials in the C-D interbed. Agreement between simulated low and high maximum values and the observed range in the deep tensiometers mostly improves in both the B-C and C-D interbeds with increasing values of the N parameters. The general effect of increasing the N parameter can be seen in the Average of the Maximums and Overall Interbed Average columns, where the values show that both interbeds get wetter overall.

5.1.3 Remedial Investigation and Feasibility Study Base Model Comparison to Interbed Saturation

Rather than simply picking the van Genuchten N parameter from the simulation with the best statistical fit to the observed averaged water potentials presented in the previous section, consideration was also given to how wetter conditions within the interbeds affect CCl_4 transport. Figures 5-3, 5-4, and 5-5 show the maximum simulated water saturation at each horizontal gridblock location for both the B-C and C-D interbeds. In these three figures, the simulated water saturation above 0.9 is shaded to indicate the wettest regions. Also shown in red are the locations where perched water has been observed or immediately above the interbeds. At the lowest van Genuchten N value of 1.323 (Figure 5-3), the extent of the wettest region is largest for both the B-C and C-D interbeds. As the value of N increases (Figures 5-4 and 5-5), the zones with elevated saturations decrease in size. With calibration to CCl_4 as one of the objectives in developing this model, the simulations with extensive wet regions in the interbed better served to spread out simulated CCl_4 concentrations horizontally in the vadose zone and better mimicked observed CCl_4 behavior. As discussed in the section on modeling of CCl_4, the wetter interbeds best served to reduce downward vapor-phase diffusion. Choosing a simulation as the base case was a matter of balancing the improvement in observed fit to the water potentials against a decrease in agreement for the CCl_4 transport modeling. With these competing interests, the status quo value of N equal to 1.523 that was used in the ABRA was selected for continued use in the RI/FS model.

5.1.4 Remedial Investigation and Feasibility Study Base Model Comparison to Interbed Vertical Water Fluxes

In addition to comparisons of simulated and observed matric potentials, comparisons were also made between estimated water fluxes from those matric potentials and simulated water fluxes from the model. The simulated maximum vertical Darcy velocities across the B-C and C-D interbeds are shown in Figure 5-6. Irregular contour intervals set at 0.5, 1, 3, 5, 7, 10, 15, 20, and 25 cm/year are used to show adequate detail. These results illustrate spatial distribution of simulated water fluxes.

The degree of focusing of water movement by simulated variable topography and the presence and absence of the A-B interbed is notable. The spatial average of the assigned infiltration rate inside the SDA is 5 cm/year (1.9 in./year). By the depth of the B-C interbed, a large portion of the western half of the SDA is at a deficit relative to this value. West of the SDA boundary, there is zone of increased vertical water flux primarily due to depressions in the upper surface of both the A-B and B-C interbeds. In the eastern half of the SDA, there is a large area of increased water flux that extends southward past the southern SDA boundary. By the depth of the C-D interbed, there is no zone of increased water flux west of the SDA boundary. The zone of increased flux through the B-C interbed has dissipated. The zone of elevated water flux in the eastern half of the SDA persists through the C-D interbed, although it has shifted toward the east-southeast due to the topography of the top of the C-D interbed. The interpolated channel in the upper surface of the C-D interbed, leading east-southeast beneath the Transuranic Storage Area, does capture some water and directs it all the way to the southeastern corner of the model domain, where it is forced to go through the C-D interbed due to the horizontal no-flux boundaries.

These zones of increased water flux exert an influence on where simulated contaminants migrate through the vadose zone. For comparison purposes, estimated steady-state vertical Darcian fluxes at the deep tensiometer monitoring locations from Hubbell et al. (2004) are shown in Figure 5-6. These estimated values are based on the averaged matric potentials from McElroy and Hubbell (2003), the use of a unit-gradient assumption, and hydraulic characterization of saturated and unsaturated properties of collocated core samples. Comparability of the simulated and estimated fluxes varies. In the B-C interbed, the simulated high-infiltration region west of the SDA is partially supported by estimated values for Wells O4 and I4. The low value at Well O1, south of the western SDA boundary, agrees with the simulated flux through this region. The two extremely high-infiltration estimates at Wells I-2S and I-4S are so far out of range that there is no comparison in the simulated results. The low estimated flux at

Well O3, closer to the center of the SDA, agrees well. Elevated values at Wells I-5S and O2 show relatively good agreement with the simulated region of elevated flux in the eastern half of the SDA. In the C-D interbed, there is less agreement, partly caused by coarser discretization. The simulated water flux across the western part of the SDA does not vary much from 1 cm/year (0.4 in./year), while the estimated values range from 7.8 to 213 cm/year (3 to 83.8 in./year). Note that if the spreading-area water source were still included in these simulations, the simulated flux would show better agreement.

5.2   Fractured Basalt Hydrologic Property

The TETRAD parameter, B_w (see Equation [4-7]), controls the degree of curvature in the relative permeability for the fractured basalt for the aqueous phase. This parameter was changed from 1.001 in the ABRA model to 2.0 in the RI/FS model. A set of simulations was conducted with assigned values of 2.0, 1.5, and 1.001 for the B_w parameter. Figure 5-7 shows the simulated vertical average linear velocity through the fractured basalt for a horizontal slice through the simulation domain beneath the B-C interbed with these B_w parameters. The contour intervals within each of the plots in Figure 5-7 are equal, but are different between plots. An approximate one order of magnitude reduction in the simulated vertical velocity in changing the B_w parameter from 1.001 to 2.0 exists. Also, less focusing of vertical water movement with the higher B_w parameter occurs. Overall, however, the velocities remain large and maintain rapid transport down through the fractured basalt portions of the vadose zone domain with any of the B_w parameter values. Given this rapid transport through fractured basalt for any of the B_w parameters from this range and a computational speedup factor of about 20X with the B_w parameter value of 2.0 compared to 1.001 (10.2 central processing unit hours versus 217.2 central processing unit hours for these comparison simulations), the B_w value of 2.0 was selected for use in the RI/FS model.

5.3   Magnesium Chloride Dust Suppressant Transport

Magnesium chloride brine was applied as a dust suppressant on SDA roads between 1984 and 1993. Subsequent arrival of this magnesium chloride at lysimeter monitoring locations in the vadose zone was first noted by Hubbell (1993). Monitoring subsequent movement of the chloride from this application in the vadose zone and aquifer gives insight into movement of water and dissolved-phase transport in general. Although the RI/FS vadose zone model was not strictly calibrated against this chloride transport, an effort was made to simulate application and transport of chloride to see if the RI/FS model emulated the observed transport.

Hull and Bishop (2003) present a detailed description of the reasons for the magnesium chloride application, the possible effects on transport, the most probable mass of magnesium chloride applied to the roads, the location of the applications, and the monitoring results that imply quick movement through the vadose zone. These monitoring observations were updated with more recent monitoring results in Koeppen et al. (2005). Results from both reports are compared against simulation results in this section.

One caution must be given before making any comparisons between simulated and observed results. A limitation is inherent in the source-release and vadose zone transport models related to discretization. The gridblocks in the most refined portion of the model are 38.1 m (125 ft) on a side. Infiltration rates through these gridblocks are constant and have to best approximate an average for each gridblock. Undoubtedly infiltration varies across an area 38.1 m (125 ft) on a side within the SDA, especially around roadways.
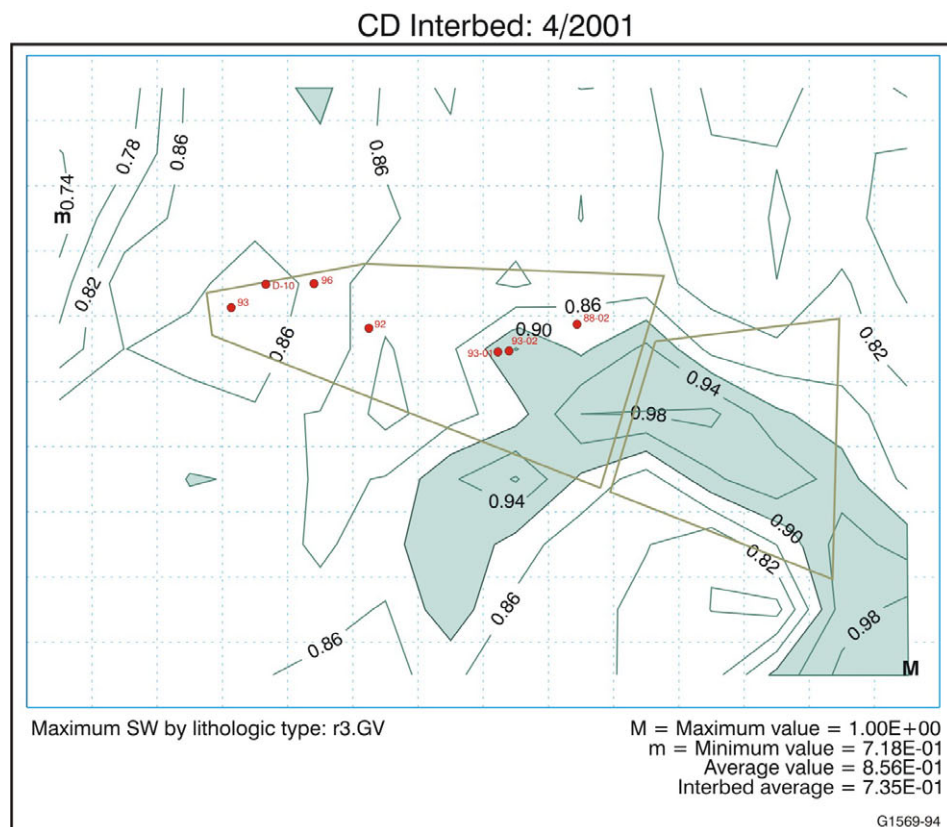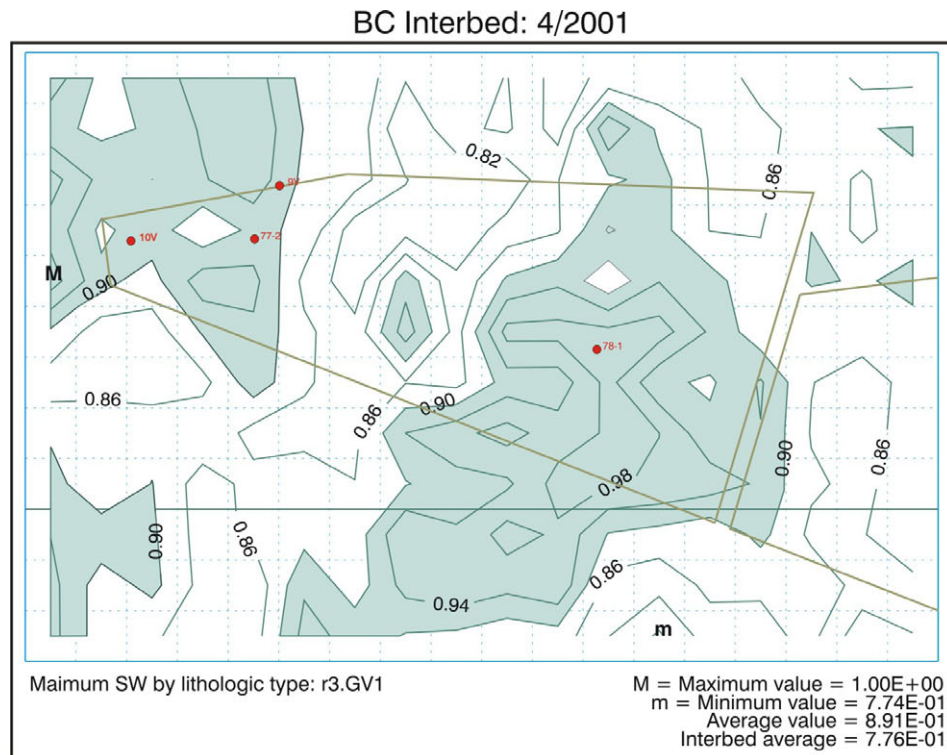
Figure 5-3. Maximum interbed water saturations with an interbed van Genuchten N parameter set to 1.323. Red symbols indicate well locations where perched water was observed at least once.

BC Interbed: 4/2001

Maximum SW by lithologic type: r1.GV1

M = Maximum value = 9.96E-01
m = Minimum value = 6.69E-01
Average value = 8.27E-01
Interbed average = 6.83E-01

CD Interbed: 4/2001

Maximum SW by lithologic type: r1.GV

M = Maximum value = 1.00E+00
m = Minimum value = 6.13E-01
Average value = 7.82E-01
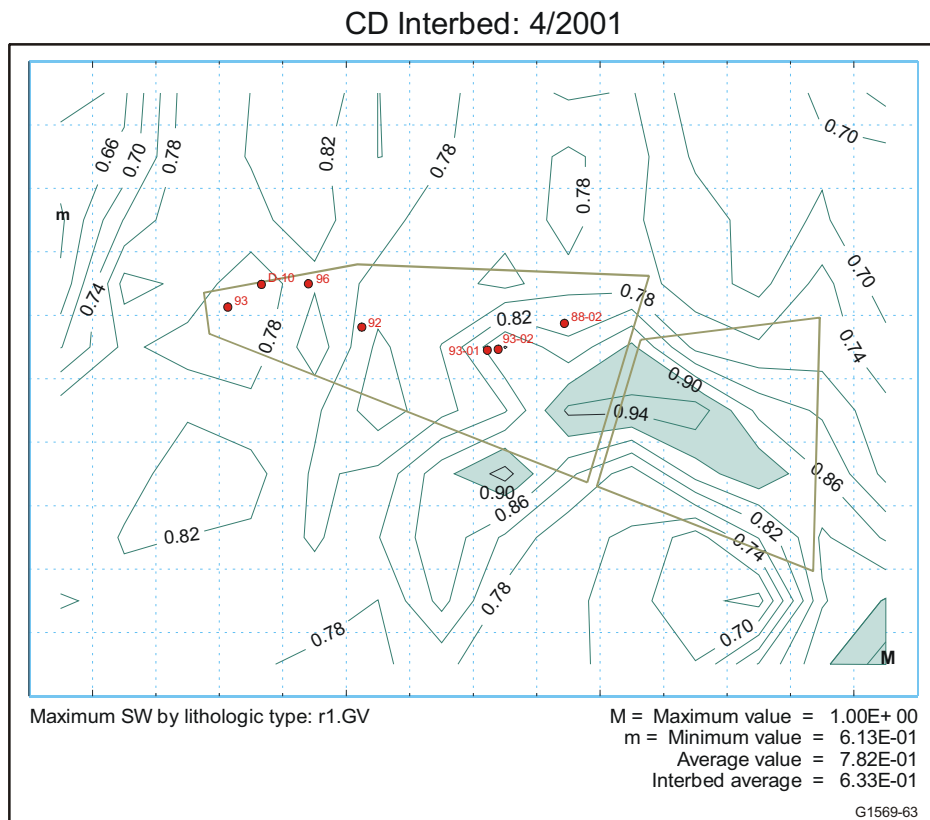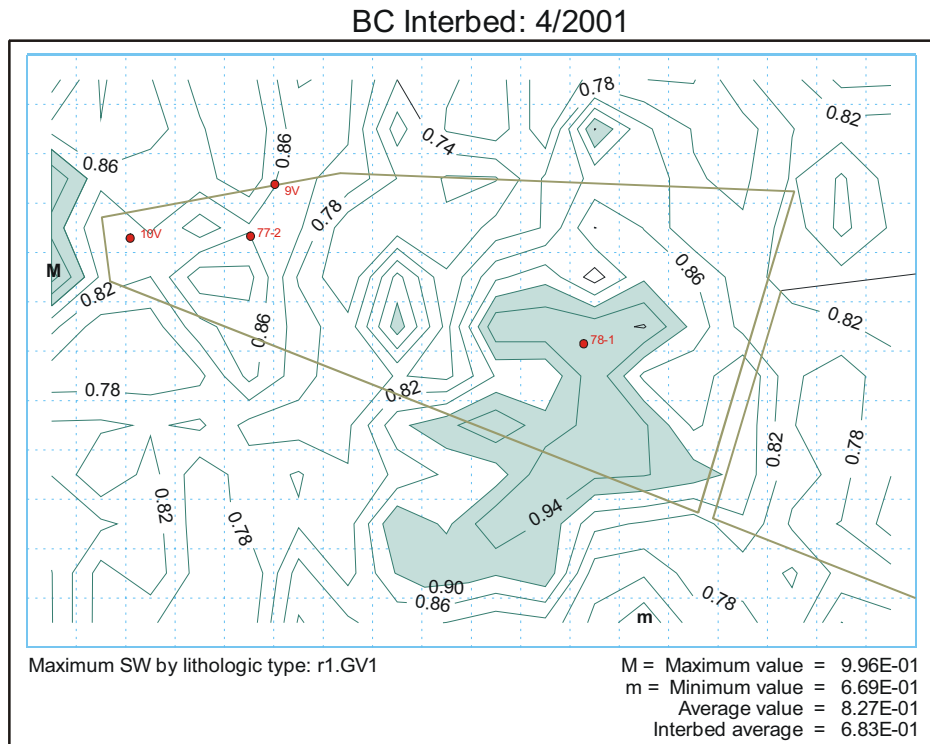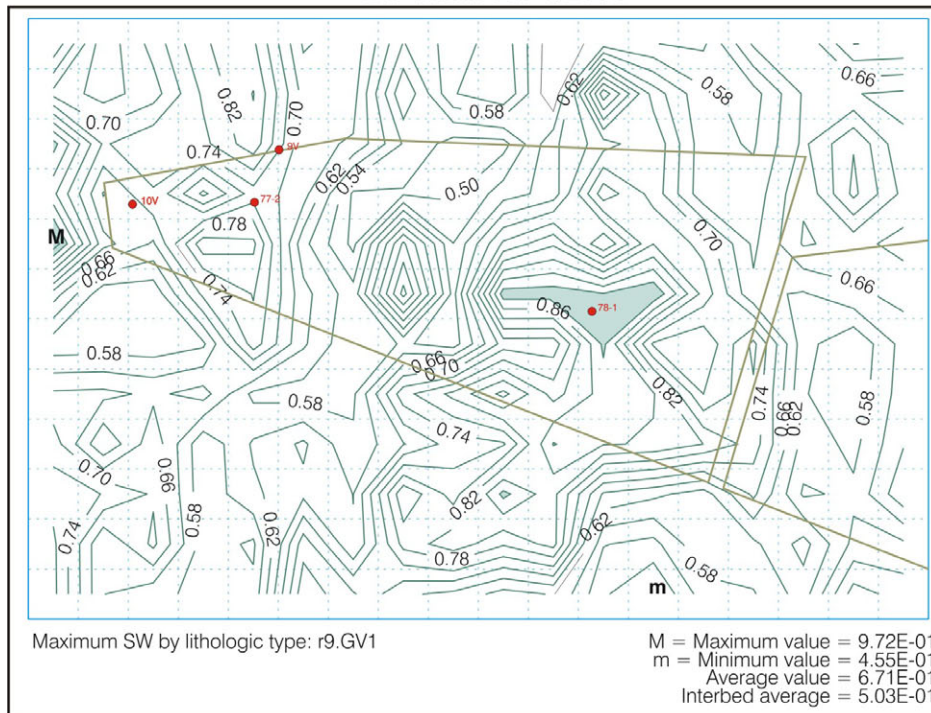Interbed average = 6.33E-01

G1569-63

Figure 5-4. Maximum interbed water saturations with an interbed van Genuchten N parameter set to 1.523 (base case). Red symbols indicate well locations where perched water was observed at least once.

BC Interbed: 4/2001

Maximum SW by lithologic type: r9.GV1

M = Maximum value = 9.72E-01
m = Minimum value = 4.55E-01
Average value = 6.71E-01
Interbed average = 5.03E-01

CD Interbed: 4/2001

Maximum SW by lithologic type: r9.GV

M = Maximum value = 1.00E+00
m = Minimum value = 4.11E-01
Average value = 6.13E-01
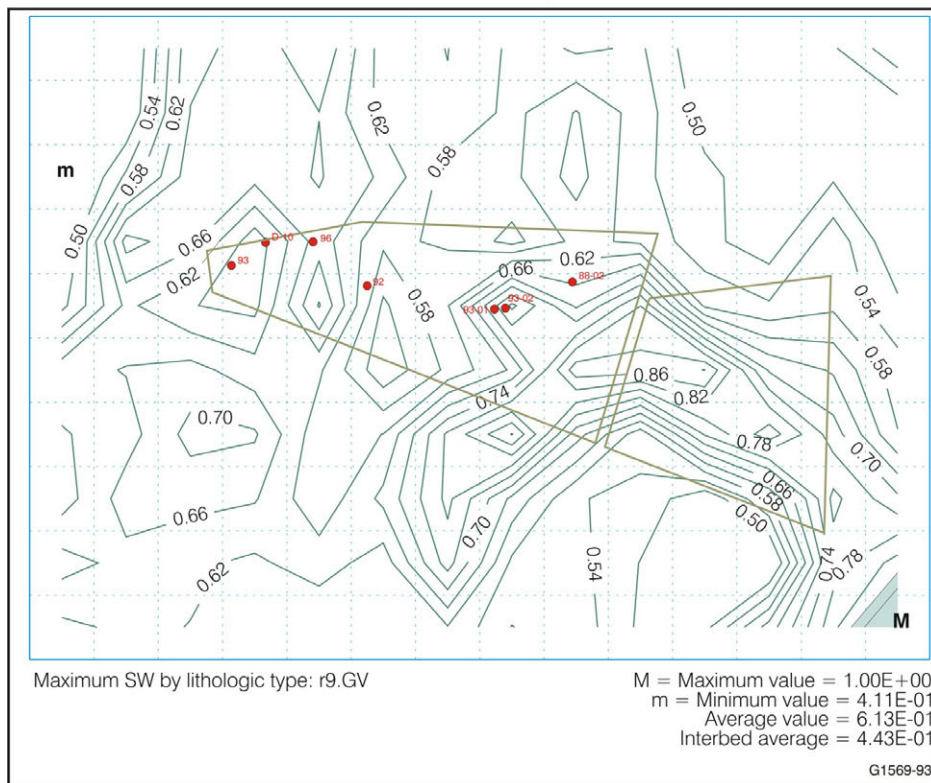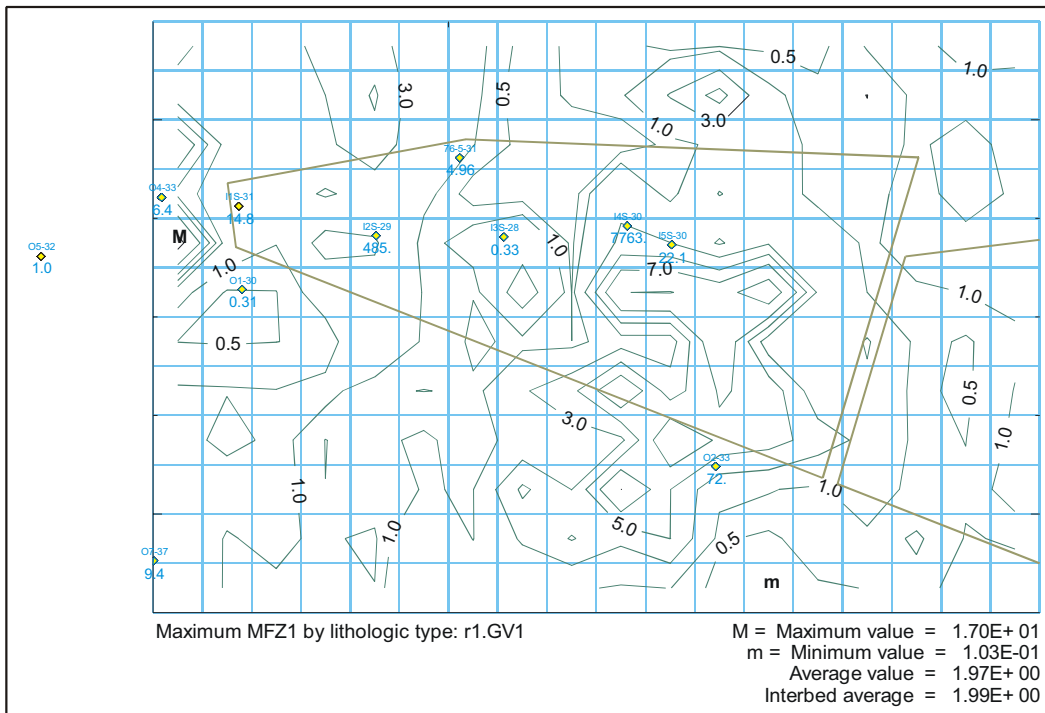Interbed average = 4.43E-01

G1569-93

Figure 5-5. Maximum interbed water saturations with an interbed van Genuchten N parameter set to 2.423. Red symbols indicate well locations where perched water was observed at least once.
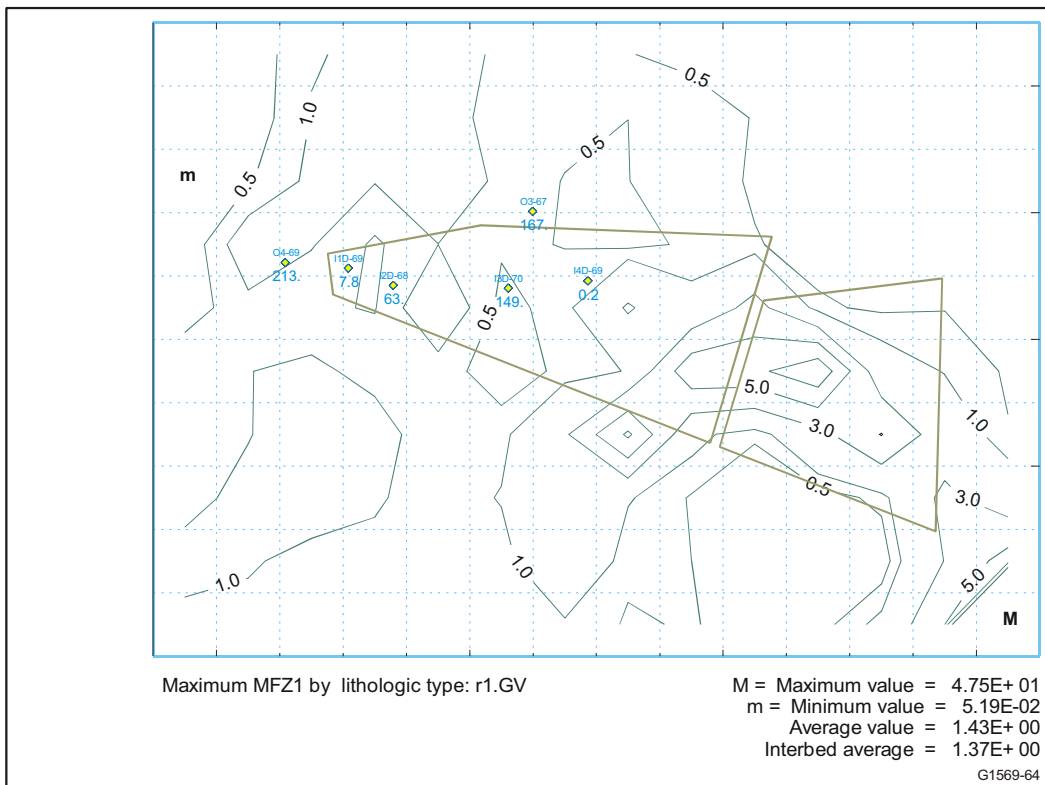
Figure 5-6. Maximum interbed vertical water flux (cm/year) for the base-case model and estimated vertical flux from McElroy and Hubbell (2003).
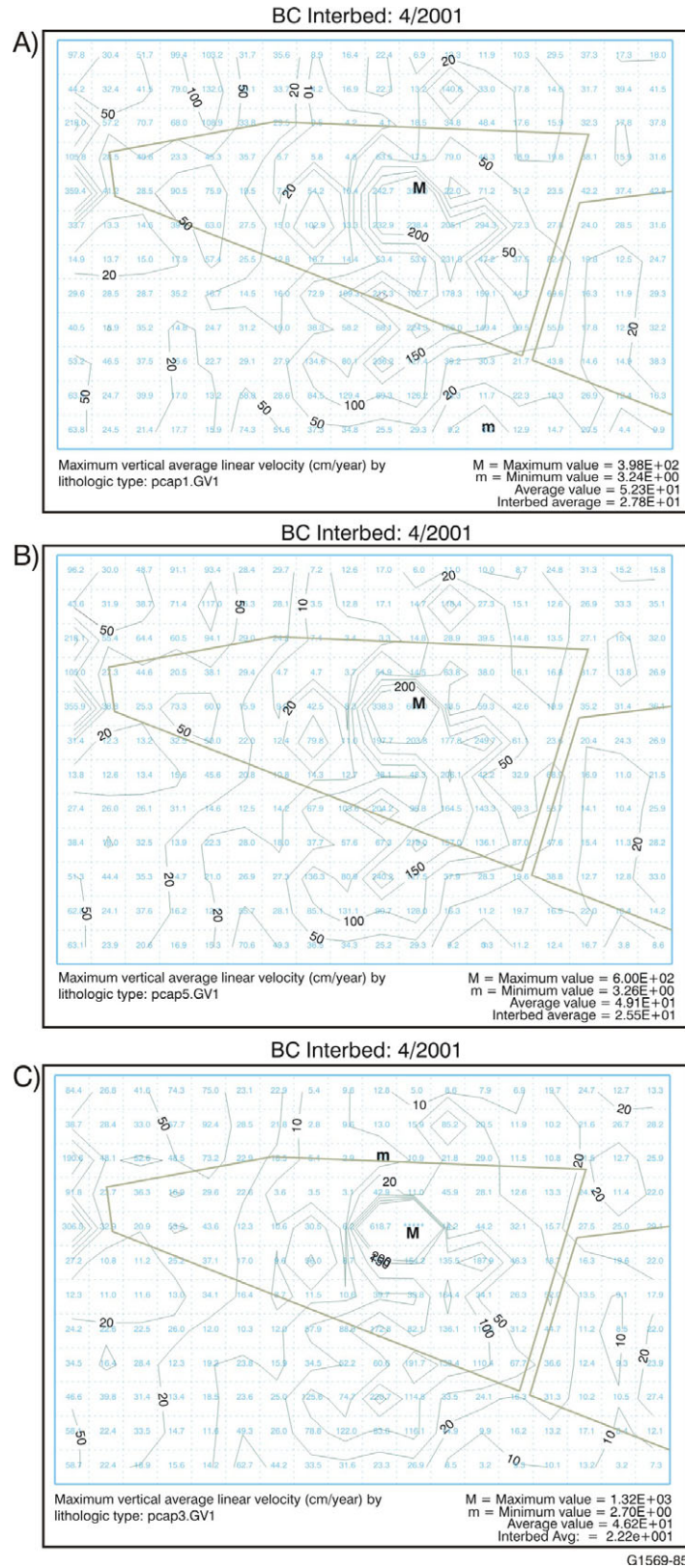
Figure 5-7. Simulated vertical average linear velocity in fractured basalt beneath the B-C interbed for A) B_w =2.0, B) B_w =1.5, and C) B_w =1.001.

Figure 5-8 shows the locations where magnesium chloride brine was determined to have been applied in the SDA (Hull and Bishop 2003) with the RI/FS model's first- and second-level refined grids superimposed. Figure 5-8 shows information for all years brine was applied. The brine application for each year was averaged for those gridblocks contacting an application zone in Figure 5-8. These averaged mass amounts were released in the model in the second gridblock below land surface at a depth of 0.75 m (2.5 ft) so they did not interfere with application of the surface boundary water fluxes in the uppermost gridblock. Figure 5-9 shows the volume in gallons of brine for Calendar Year 1984 applied to the gridblocks in the model. Rather than showing similar figures for 1985 and 1992 through 1993, Figure 5-10 shows the cumulative application for the entire application period of 1984 through 1993.

Two chloride brine release scenarios were initially evaluated using the ABRA model, a gradual release scenario and a 100% annual release scenario. In the 100% annual release scenario, releases of the chloride mass into the model occurred at a constant rate for a 1-year period, beginning at the midpoint of the application year. In the gradual release scenario, a fraction equivalent to 0.1632 of the estimated total mass applied was released each year until the total mass was released. Because the simulation results underestimated the observed chloride concentrations, only the 100% release scenario was used when updating the chloride brine simulations in the RI/FS model. This update used the base RI/FS model, including assigned surface infiltration fluxes (excluding the three historical flooding events) to simulate chloride brine transport, resulting from application of brine to the surface of the SDA. The three flooding events were not included because they all occurred before the first brine application.

Results for these chloride brine simulations were evaluated using cross sections and time histories. The locations for both are shown in Figure 5-11. The cross section was selected because it contains the D06-DL02 lysimeter, which shows the best breakthrough of the chloride brine. Because there can be multiple lysimeters at different elevations for an individual well location, lysimeters are referred to in this section using the combined well name-lysimeter number identifier. The northern time-history location was likewise selected for the same reason. The southern time-history location was selected to show results from a location where brine was applied at the surface.

Simulation results with the 100% annual release are shown in Figure 5-12. The simulation time of May 2003 was chosen because it corresponded to a year with a sampling event where chloride was elevated to the highest priority for analyses in one round; therefore, it has the most chloride analyses from the vadose zone monitoring system. Monitoring results from lysimeters within this cross section are superimposed at their respective locations. These results used the same time window of plus or minus 1 year and were averaged when more than one sample was available. Although the simulation results underpredict the monitoring results, the northward slope of the A-B interbed can be seen to slightly impact the simulation results. This northward spread at depth partially could explain why lysimeter DO6-DL02 shows such high concentrations when there are no records of brine being applied in the northern half of the SDA.

The simulated chloride concentration time history for the 100% annual release at the D06-DL02 location and depth is shown in Figure 5-13, along with observed monitoring results. The top plot shows both simulated and observed results with a consistent vertical axis, and illustrates the extent of the underprediction of the simulated results compared to the observed. The bottom plot uses a secondary axis for the field-monitoring results to allow the magnitude of the simulation results to be seen. There are at least two causes for underprediction. First, large gridblock sizes in the RI/FS model result in averaging the chloride mass over large volumes and thereby reducing the simulated concentration. In reality, chloride brine predominantly infiltrates into the subsurface over a small area defined by ditches along the roads. Second, in the simulation there was no chloride brine released above this location.
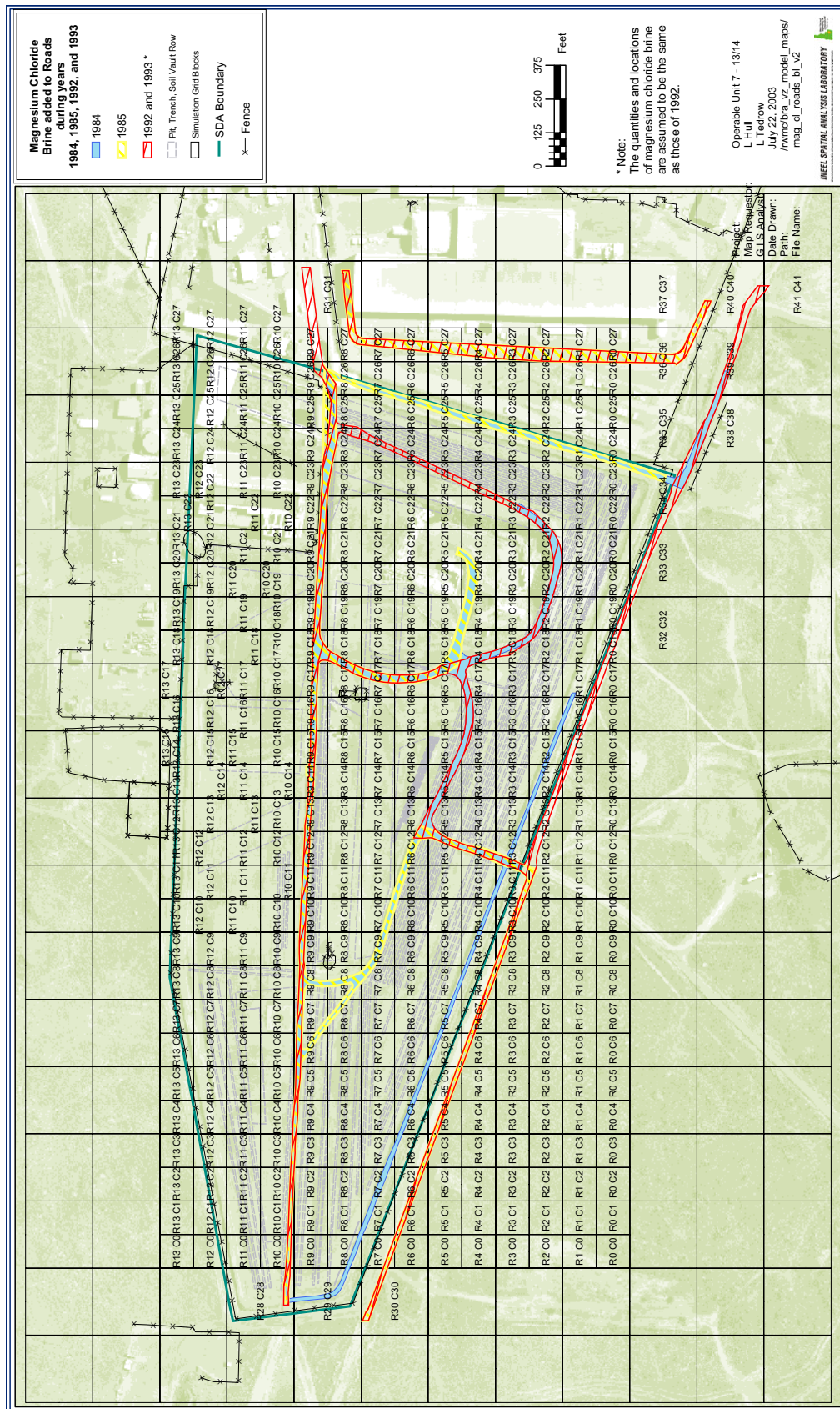
Figure 5-8. Estimated locations of magnesium chloride application in 1984, 1985, and 1992 through 1993 (after Hull and Bishop 2003).
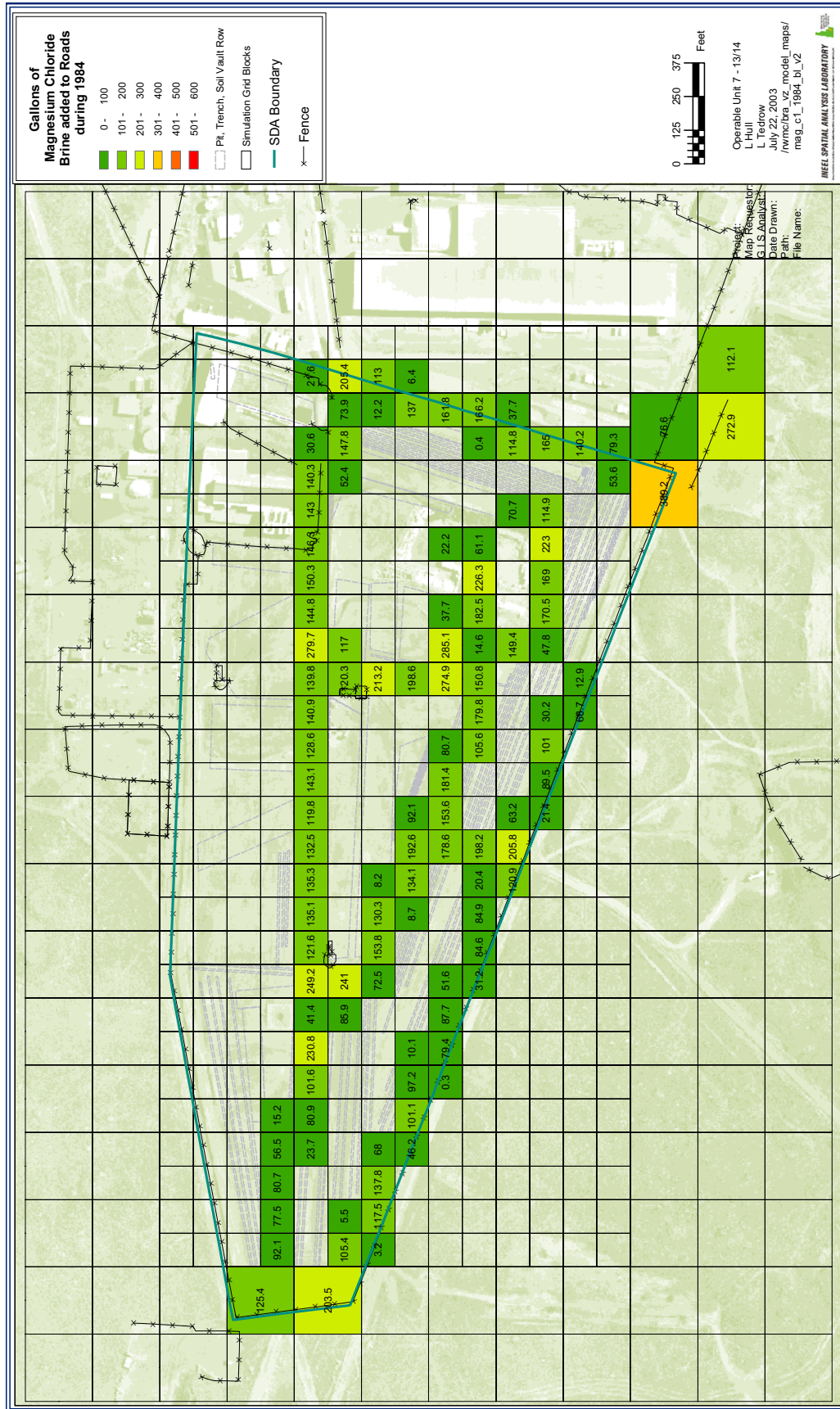
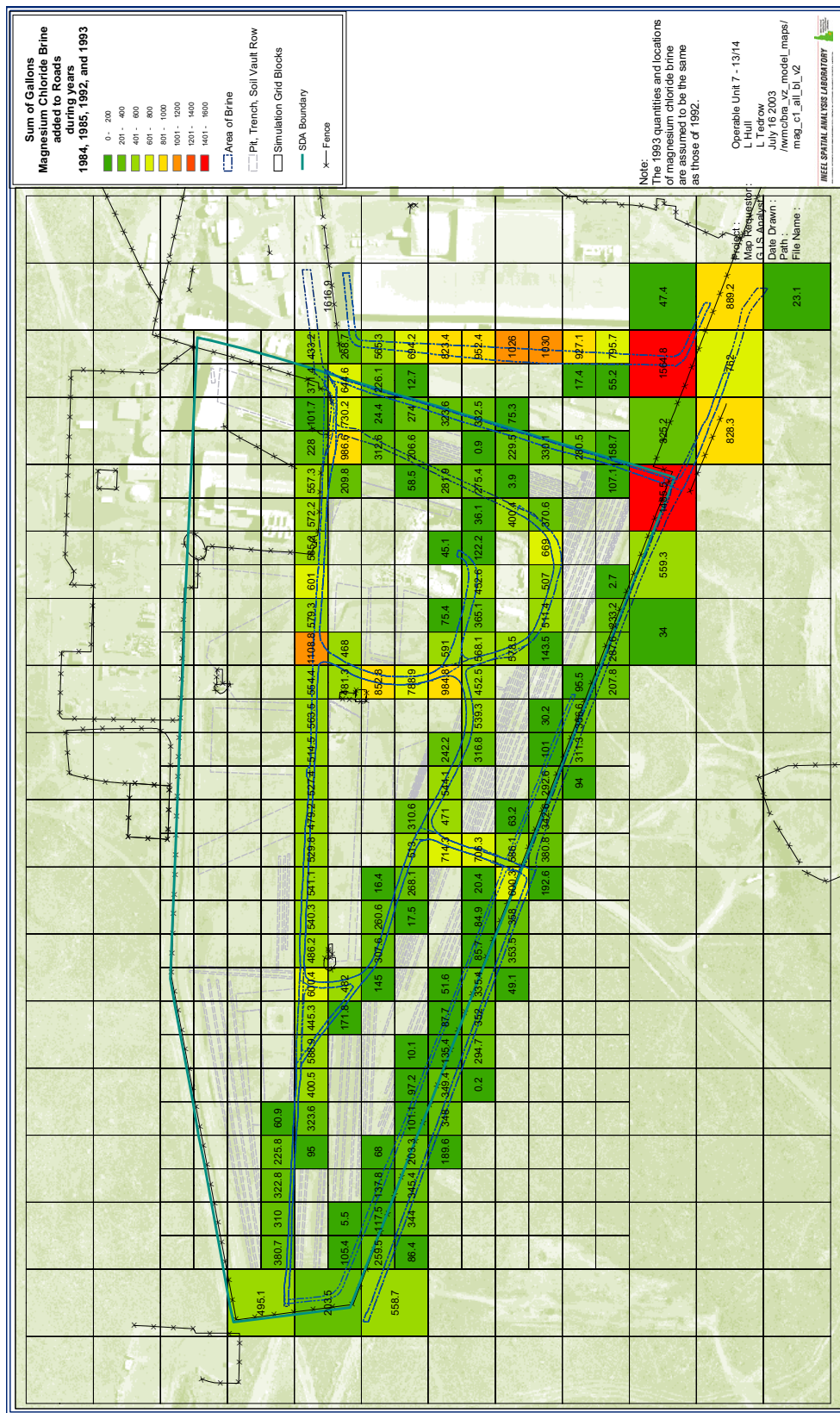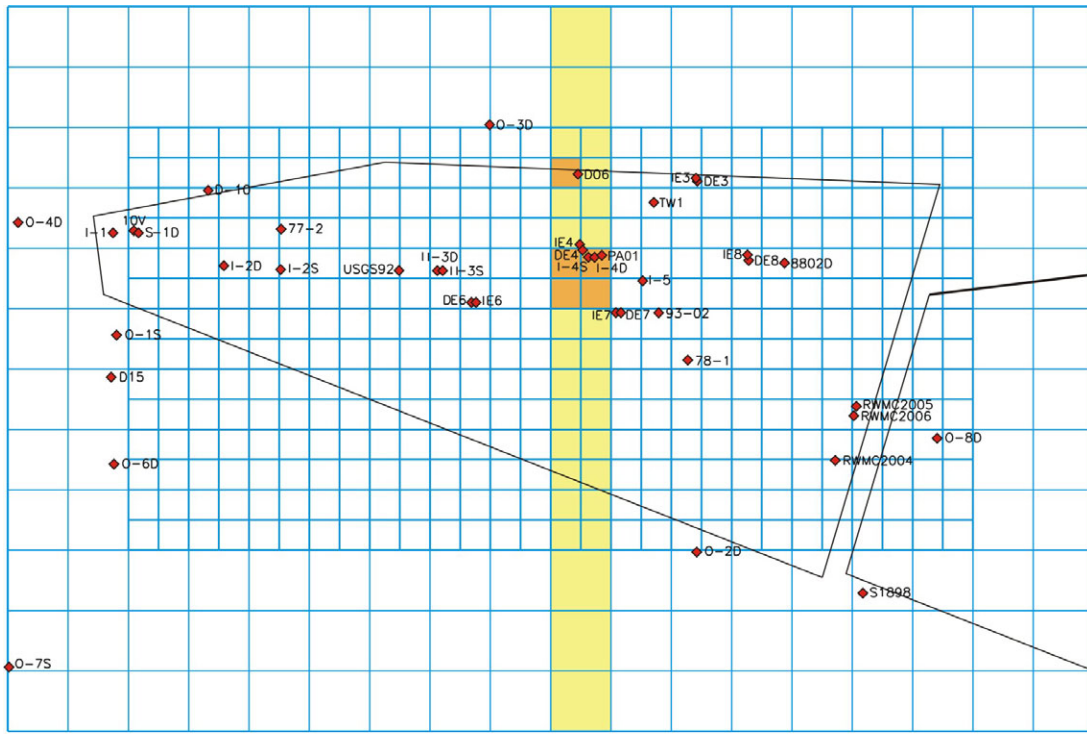Figure 5-9. Simulated magnesium chloride application rates and locations in 1984.

Figure 5-10. Simulated cumulative magnesium chloride application rates and locations from 1984 through 1993.

Figure 5-11. Locations for cross section (yellow shaded) and time history (orange shaded) comparisons for chloride simulations. Well locations are indicated by red diamonds.
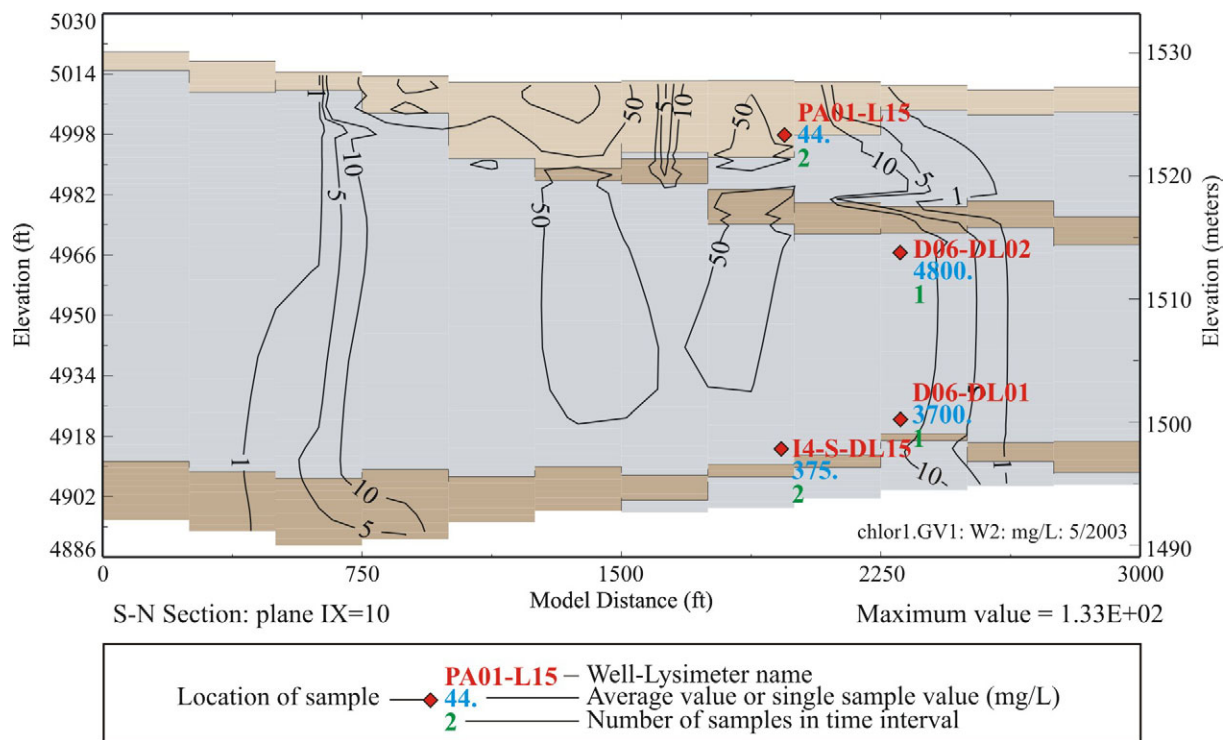
Figure 5-12. Simulated chloride concentrations with 100% annual release of applied chloride brine. See Figure 5-11 for location of cross section.
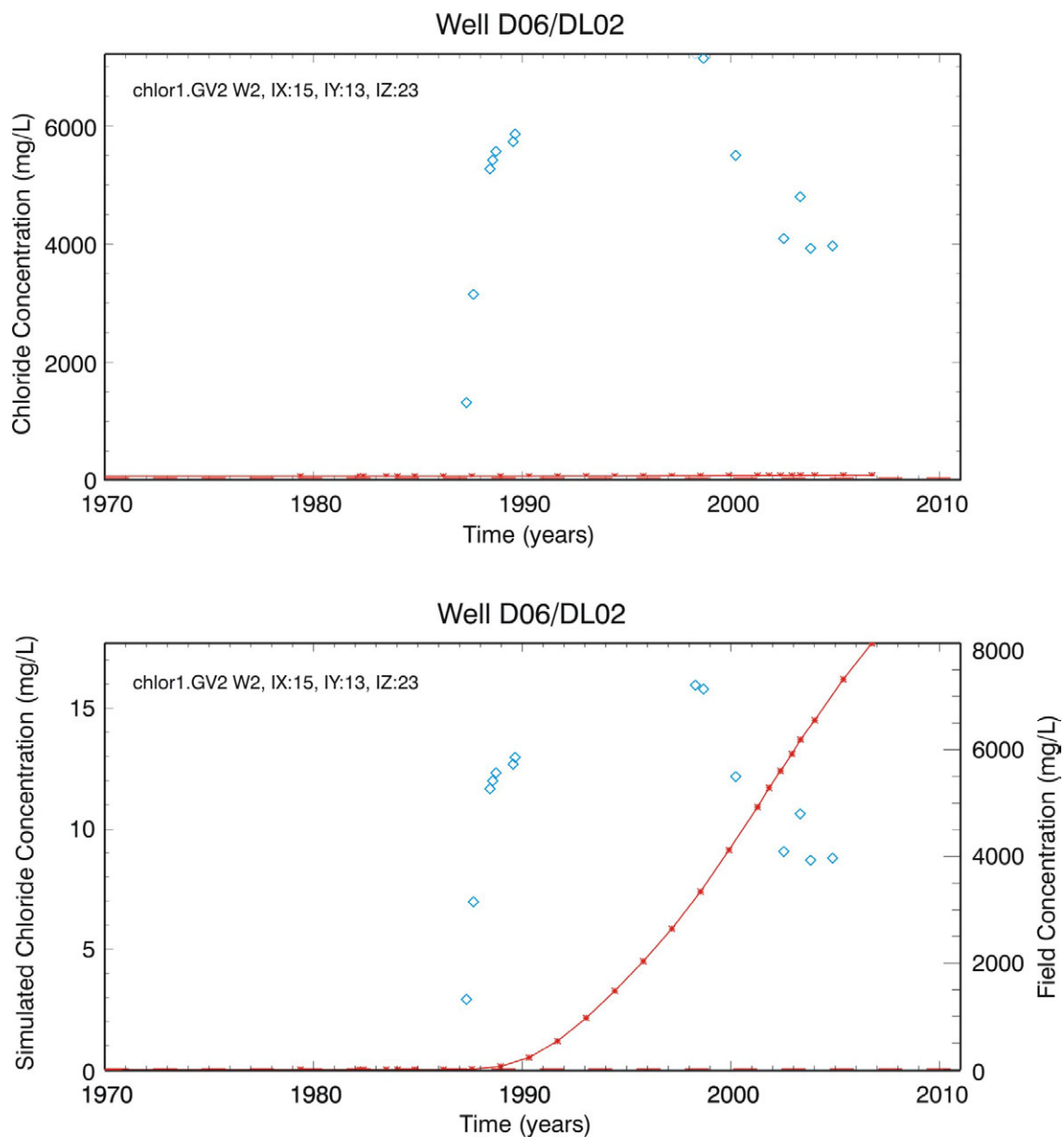
Figure 5-13. Simulated (red line) and observed (blue diamonds) chloride concentrations at the D06-DL02 lysimeter location. The bottom plot has observed concentrations plotted on the right axis. See Figure 5-11 for lysimeter location.

Figure 5-14 shows simulated chloride concentrations for locations I-4S-DL15 and I-4D-DL14, which do have chloride brine applied above them in the simulation. Although the simulation results underpredict the observed concentrations, there is at least an observable breakthrough using the same vertical scale.

Figure 5-14. Simulated (red line) and observed (blue diamonds) chloride concentrations at the I-4S-DL15 and I-4D-DL14 lysimeter locations. See Figure 5-11 for lysimeter locations.

Both simulated chloride time histories in Figures 5-13 and 5-14 show monotonically increasing concentrations that do not mimic the transient double-pulse character in the monitoring results at D06-DL02. This may be due to use of constant infiltration rates from the RI/FS model that were developed with a primary focus on infiltration through waste zones.

The question about the impact of constant infiltration rates led to the next two simulations where a spring infiltration event occurred at the locations shown in Figure 5-15. The locations were chosen to emulate additional infiltration occurring in ditches bordering the main east-west access road across the SDA. In these simulations, 10 and 30 cm of water were applied to the ditch area during a 30-day period, beginning April 1 of each year for years that had greater than 10 in. of precipitation since Calendar Year 1975. This resulted in increased infiltration in 19 out of 30 years from 1975 through 2004. Figures 5-16 through 5-18 show simulation results for the case of an additional 10 cm of water each year in April. Figures 5-19 through 5-21 show simulation results for the case of an additional 30 cm of water each year in April. The additional water accelerates transport, as can be seen in the time-history figures. Simulated concentrations at depth increase with the additional water applied along the ditches, but observed concentrations are still underpredicted. For the 30-cm simulation, concentrations have peaked by Calendar Year 2004 and then decrease, indicating the simulated front has passed this depth.

Figure 5-15. Locations receiving additional water to emulate infiltration in ditches along the primary east-west access road across the Subsurface Disposal Area.

Figure 5-16. Simulated chloride concentrations with an additional 10 cm infiltrating along the east-west access road each year in April. See Figure 5-11 for location of cross section.

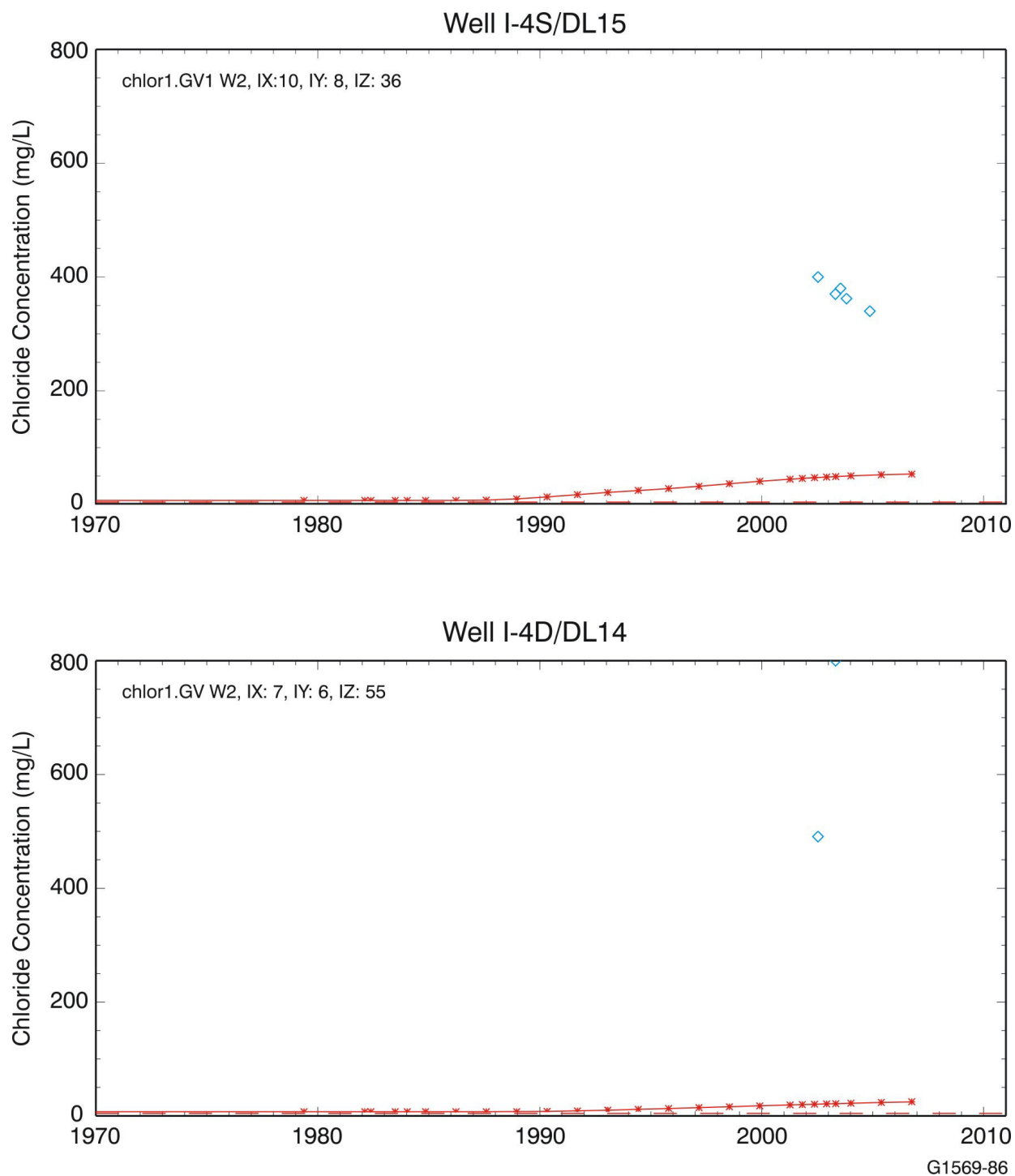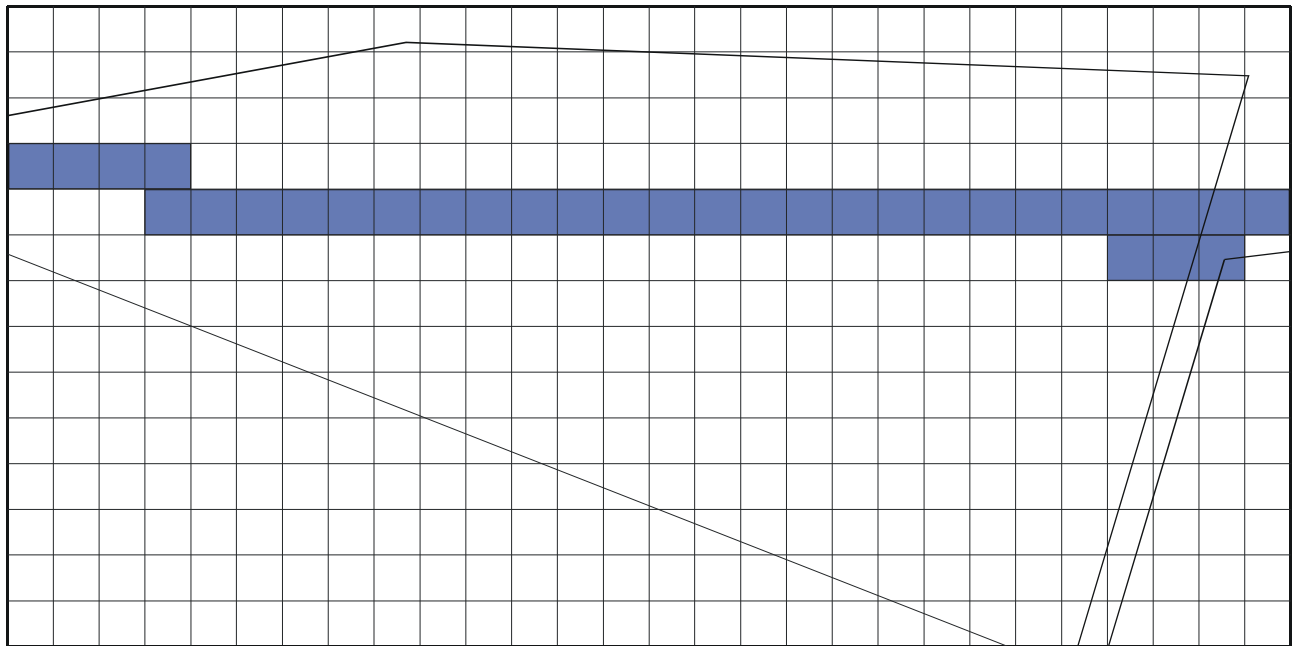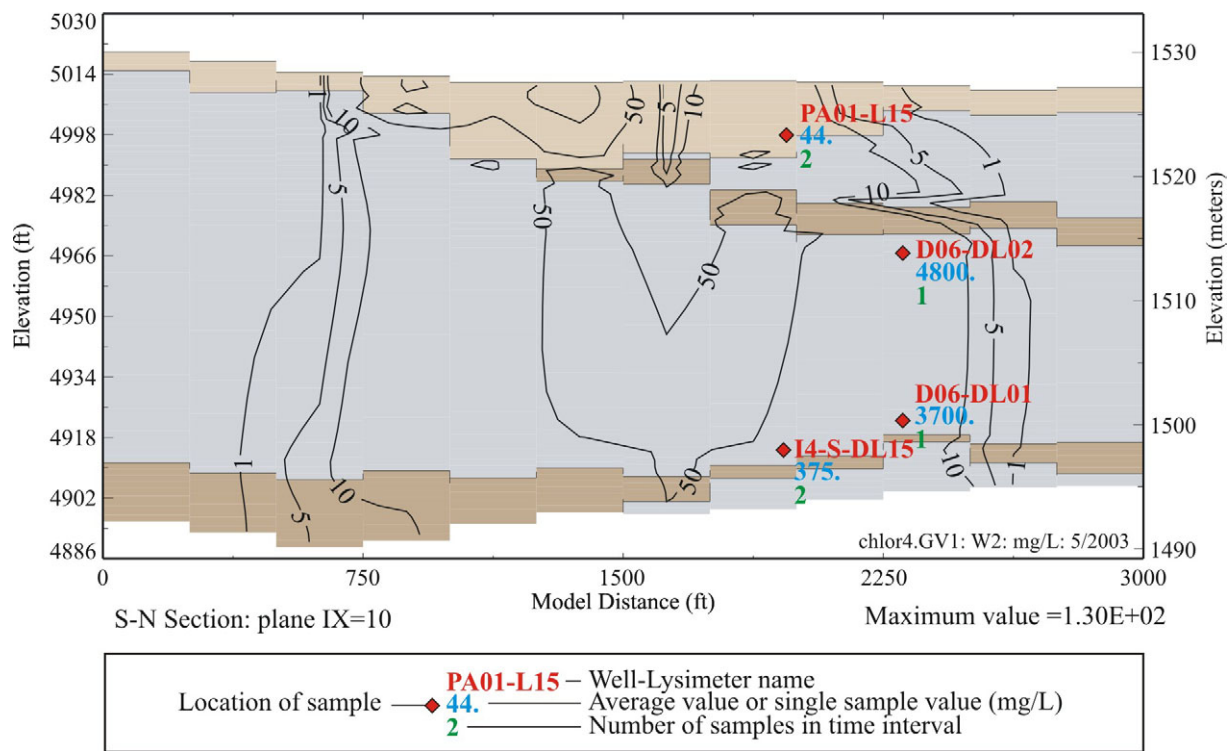Figure 5-17. Simulated (red line) and observed (blue diamonds) chloride concentrations at the D06-DL02 lysimeter location with an additional 10 cm infiltrating along the east-west access road each year in April. Note that the plot has observed concentrations plotted on the right axis. See Figure 5-11 for lysimeter location.

Figure 5-18. Simulated (red line) and observed (blue diamonds) chloride concentrations at the I-4S-DL15 location with an additional 10 cm infiltrating along the east-west access road each year in April. See Figure 5-11 for lysimeters location.
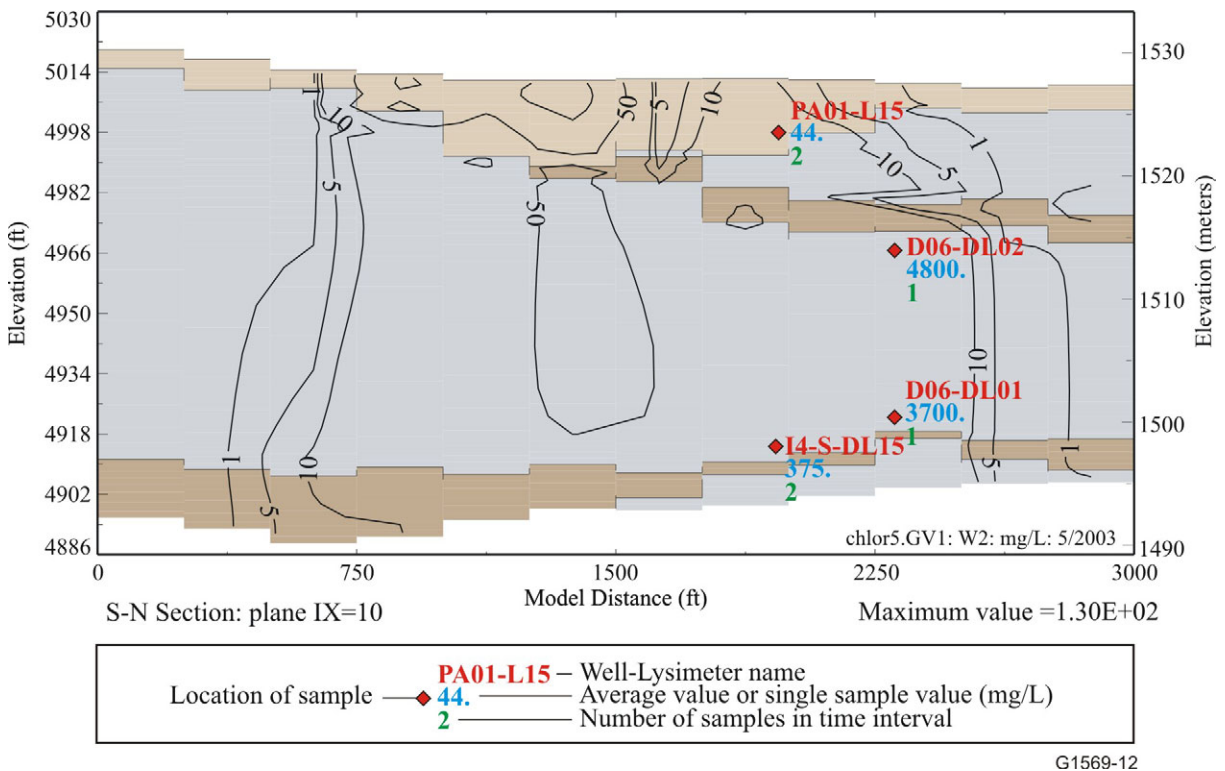
Figure 5-19. Simulated chloride concentrations with additional 30 cm infiltrating along the east-west access road each year in April. See Figure 5-11 for location of cross section.
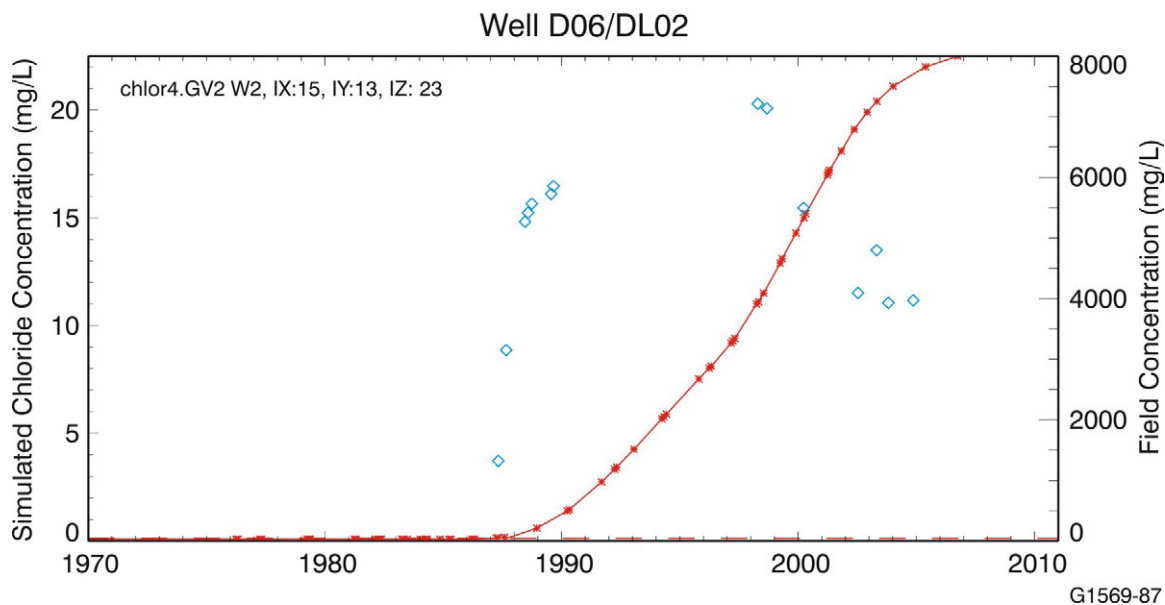
Well D06/DL02

Figure 5-20. Simulated (red line) and observed (blue diamonds) chloride concentrations at the D06-DL02 lysimeter location with additional 30 cm infiltrating along the east-west access road each year in April. Note that the plot has observed concentrations plotted on the right axis. See Figure 5-11 for lysimeter location.
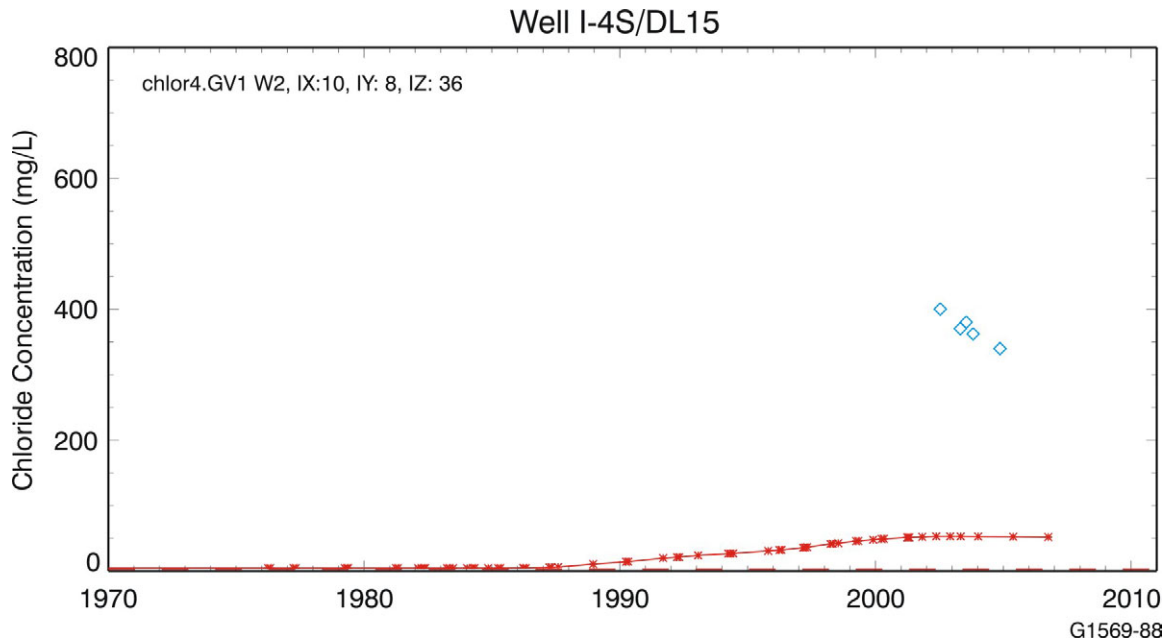
Well I-4S/DL15

Figure 5-21. Simulated (red stars) and observed (blue diamonds) chloride concentrations at the I-4S-DL15 location with an additional 30 cm infiltrating along the east-west access road each year in April. See Figure 5-11 for lysimeter location.
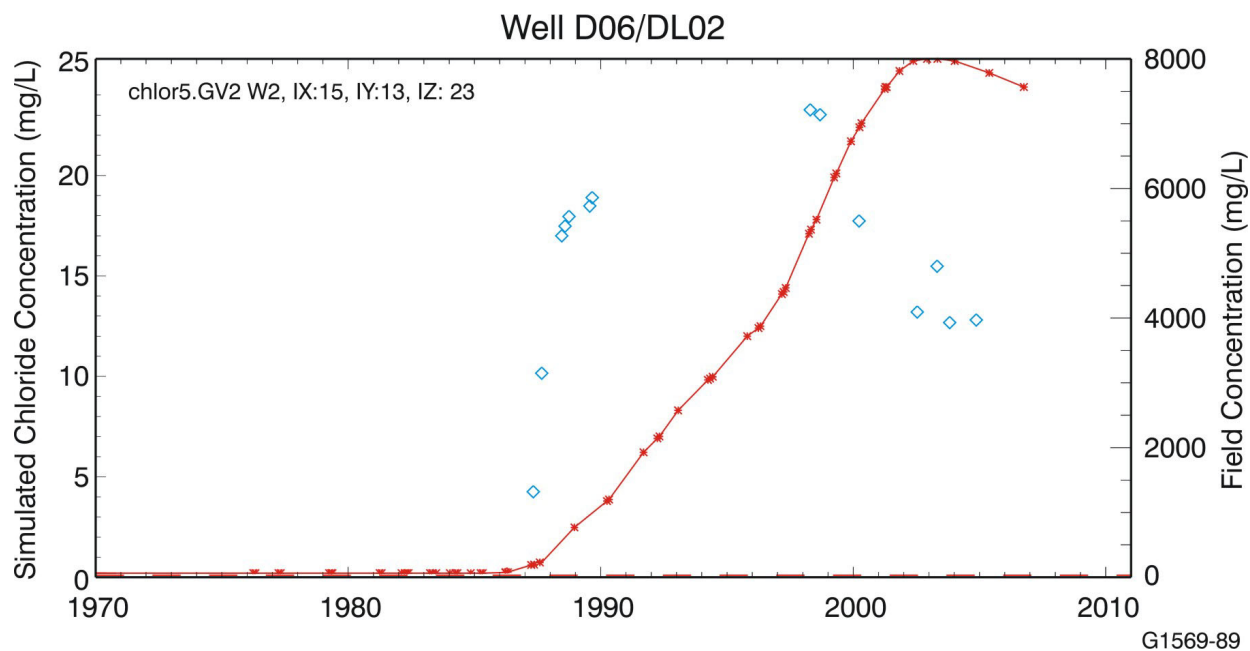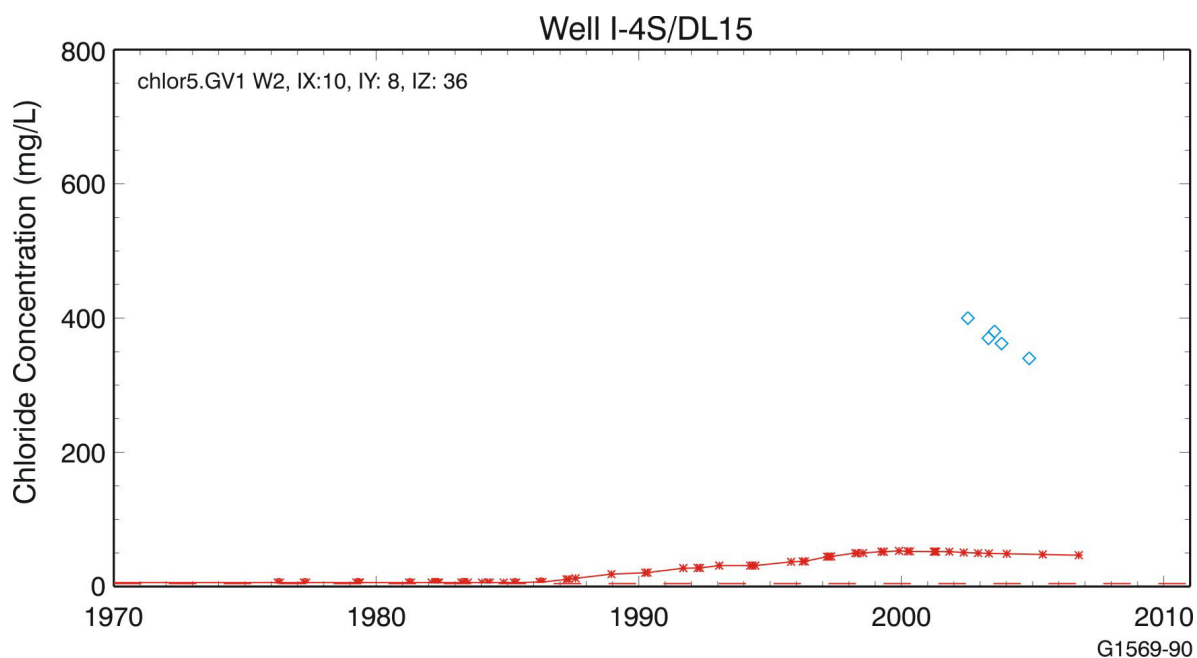
To compare transient behavior between the base case and additional water simulations, a profile with chloride concentration time histories from increasing depths for one location is shown in Figure 5 22. The location shown is for a gridblock in the second-level refined grid that corresponds to the I-4S-DL15 lysimeter. The depths portrayed are shallower than those shown previously for this lysimeter. The transient source that shows the characteristic double hump is evident at the shallow depth, which is only one gridblock lower than the gridblock where the chloride is released in the model. At this shallow depth, additional water serves primarily to dilute concentrations. However, at subsequently greater depths, the simulations with additional water result in higher simulated chloride concentrations. They also retain the transient character of the chloride release better than the base model.

In summary, relative to the chloride simulations, the RI/FS model has difficulty mimicking these very specific concentration time histories, even with additional water applied in an attempt to flush the chloride downward. This difficulty is primarily attributed to averaging induced by large gridblock sizes. The model with additional water applied along ditches does mimic the advance to depth in the B-C interbed, albeit at lower concentrations. The preferential nature of flow and transport is obvious in the chloride brine monitoring results when compared to this attempt to simulate brine advance. Any future efforts to simulate magnesium chloride brine movement in the subsurface should probably be performed within a more limited two-dimensional, cross-sectional model that would allow for greater discretization and improved representation of lithology.

5.4 Development and Calibration of the Volatile Organic Compound Transport Model

When the Operable Unit 7-13/14 ABRA was published, Operable Unit 7-08 in conjunction with Operable Unit 7-13/14 was in the process of updating and recalibrating the VOC transport model due to significant revisions in the CCl_4 inventory estimates. As a result, VOCs were not simulated in the ABRA transport model; rather, results from the IRA were scaled, based on the most current VOC inventory estimates. This was deemed appropriate from the standpoint that modeling with different inventory estimates would not change the risk estimates considerably. However, since the ABRA, the VOC transport model has been updated with all the corrections to the ABRA model described in this document, and has undergone additional calibration. The model also has been updated to simulate vapor vacuum extraction and includes actual operations data. This section describes VOC modeling objectives, methodology, and results of calibration.

5.4.1 Objectives

Objectives of CCl_4 calibration were to construct a model that could adequately reproduce the observed migration of CCl_4 from the SDA, and predict with a relatively high degree of confidence future concentrations of COPCs that migrate as a vapor (Group 11, VOCs and Group 8, C-14).

5.4.2 Volatile Organic Compound Model Description

The VOC transport model uses the same basic model that was developed for transport of dissolved-phase contaminants. All aspects of the dissolved-phased model for simulating water movement in the vadose zone and aquifer are the same for the VOC transport model. However, because VOCs are transported in the subsurface in multiple phases and by a number of complex, interrelated processes, additional capabilities were necessary for the VOC transport model that were not required for the flow or dissolved-phase transport model. Additional relevant transport processes and geologic features were
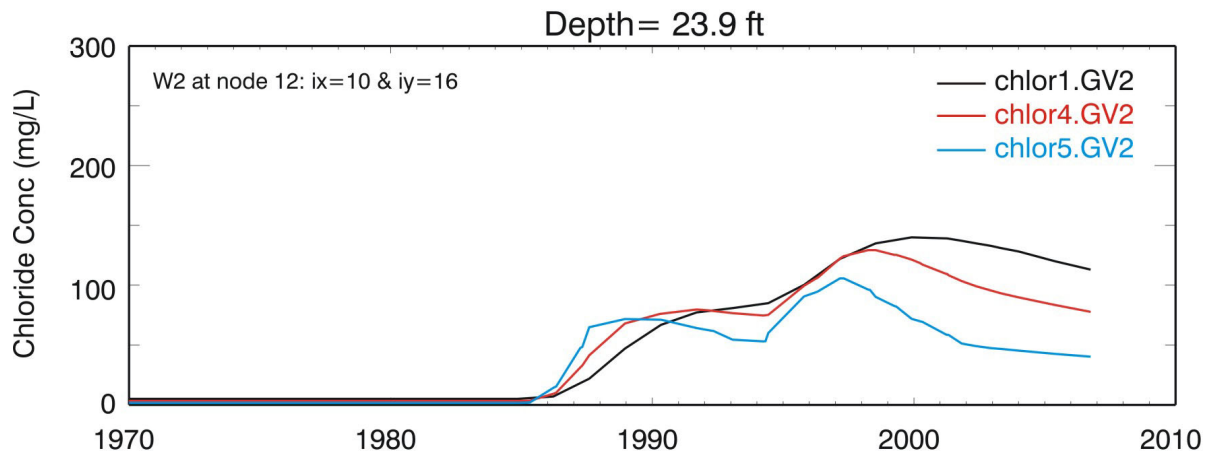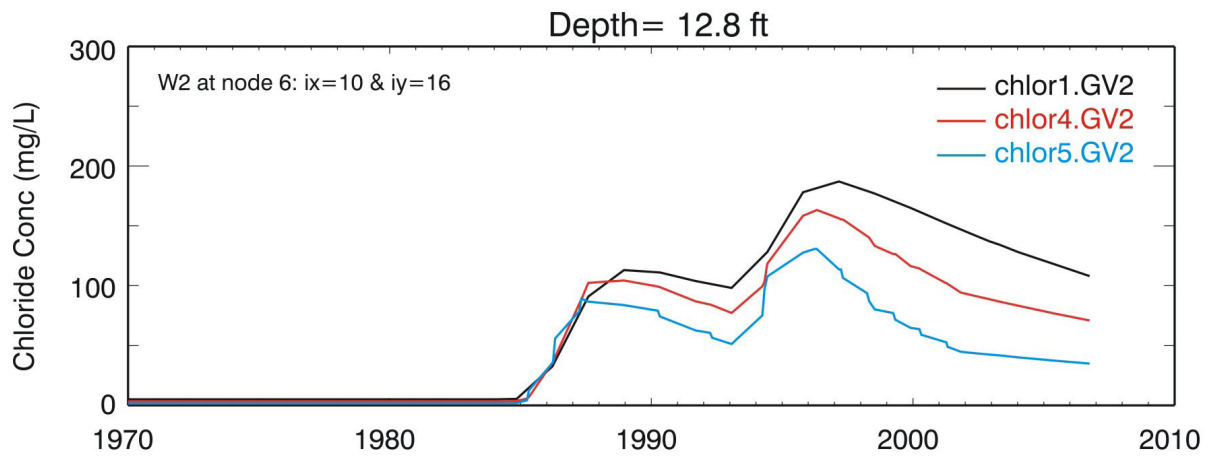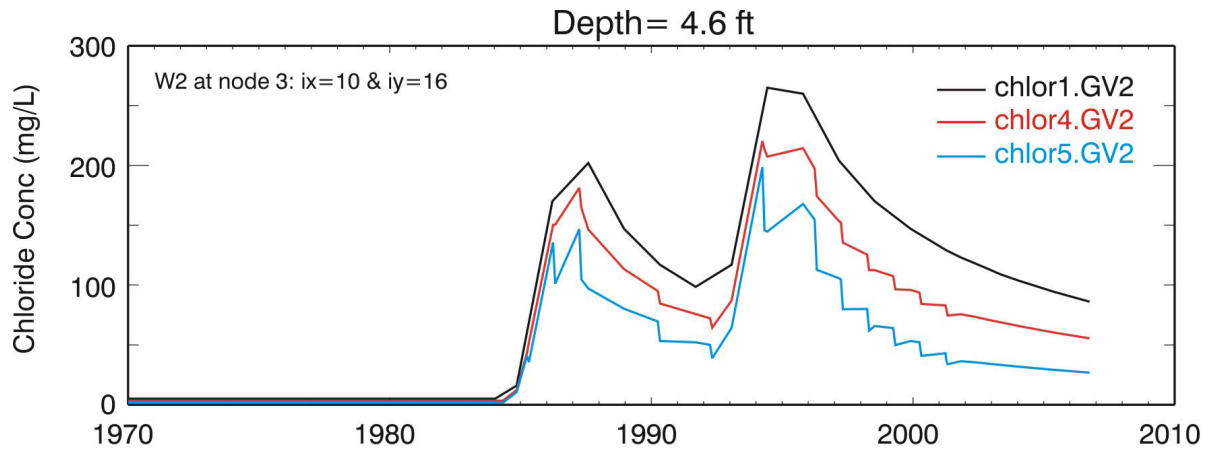
Figure 5-22. Simulated chloride concentrations at a series of increasing depths for the base (chlor1) and for the additional 10 cm (chlor4) and 30 cm (chlor5) of water infiltrating in April along the east-west access road.

included in the model only if they could be represented with reasonable accuracy, and if they produced a measurable effect on the results. Additional processes and features of the VOC transport model include the following:

- Dual-permeability, dual-porosity representation of the subsurface basalt

- Phase partitioning

- Vapor advection due to density, barometric pressure fluctuations, air injection during drilling, and vapor vacuum extraction phase partitioning

- Vapor diffusion with diffusion boundary conditions.

These additional processes and features are discussed in more detail in the following subsections.

5.4.2.1 *Conceptual Model of Volatile Organic Compound Transport.* Volatile organic compounds are transported through the subsurface by two primary mechanisms: advection and diffusion. Advection refers to passive transport of contaminants with the bulk movement of a mobile phase (i.e., gaseous, aqueous, or oleic). Diffusion is a spreading process that moves contaminants from areas of high concentration to areas of low concentration by intermolecular collisions. Partitioning occurs between all phases and is assumed to be an equilibrium process.

In the SDA, significant movement of a liquid oleic phase is unlikely because of the high viscosity of the treated waste. Even if liquid VOCs were present, the relatively small amount that might separate from the treated waste would likely residualize near the source. The high volatility of the VOCs and the relatively dry nature of the INL Site suggest that vapor transport is an important transport mechanism, especially in the basalt portions of the vadose zone. Gaseous movement of VOCs occurs primarily through diffusion and advection. Gaseous advection occurs primarily in the fractured basalt. Aqueous-phase VOCs migrate with infiltrating water, following established flow paths primarily in the sediment and fractured basalt. The basalt matrix acts primarily as a storage site for both gaseous- and aqueous-phase VOCs. The following subsections discuss VOC transport mechanisms in more detail.

5.4.2.2 *Volatile Organic Compound Transport Model Assumptions.* This section lists assumptions unique to the VOC transport model that are not listed in Section 4.2:

- All VOC COPCs were assumed to be contained in sludge. This is true for all of the tetrachloroethylene and 1,4-dioxane and 99.5% of the CCl_4, but only 51% of the methylene chloride was buried sludge. The other 49% of methylene chloride was contained in paper, rags, trash, dirt, and concrete.

- The VOC release rate (i.e., source term) was controlled by drum failure and diffusion through sludge, except for the methylene chloride that was not sludge; this portion was released by diffusion and no credit was taken for drum containment.

- In the year 2000, 50% of the original VOC mass had been released, and 50% remained in the pits (Sondrup et al. 2004).

- The vadose zone basalt is represented as a dual-continua (i.e., dual porosity and permeability) media to account for transport and storage in both the fractures and the matrix (see Section 4.3.4.2).

- Interphase mass transfer is linear and reversible.

- Partitioning between aqueous and gaseous phases is adequately described using Henry's Law.[c]

- Distribution coefficients are homogeneous in the interbeds, and sorption is negligible in basalt.

- Aqueous-phase VOCs migrate with infiltrating water, following established flow paths.

- Gaseous movement of VOCs occurs through diffusion and advection.

- Gaseous diffusion can be represented by Fickian diffusion, using an effective diffusion coefficient that includes a tortuosity factor.

- Gaseous advection is the result of density gradients and pressure gradients. Pressure gradients are caused by barometric pressure fluctuations, positive-pressure air drilling, and vapor vacuum extraction operations. Gaseous advection due to thermal gradients is negligible.

- Barometric pressure fluctuations can be adequately represented using a square-wave approximation. Fluctuations caused by passage of pressure fronts are important, while higher frequency variations due to wind gusts or diurnal temperature changes can be neglected.

- All air-drilled wells were drilled at the same speed and with the same air injection rate. Air recovery during drilling was 100% above the depth of 40 m (131 ft) below land surface, and 0% below 40 m (131 ft).

- Base-case simulations assume the Operable Unit 7-08 vapor vacuum extraction with treatment (VVET) system will operate 10 months (i.e., January through October) of each year, from 2005 through 2009, and will extract from wells in use at the end of 2004. Actual data from all other vapor vacuum extraction activities (i.e., 2-week test [1989], 4-month test [1990], treatability study [1993], and Operable Unit 7-08 operations from January 1996 through January 2005) are included.

- Eighty percent of VOC waste in the Accelerated Retrieval Project retrieval area was removed in January 2004, and containment of the remaining 20% failed in January 2004 (see Section 5.1.1 of the draft RI/BRA for an explanation).

- Injection and extraction wells are located in the center of the gridblock they occupy.

- Contaminant degradation was not included in the model.

- Calibration of the VOC transport model was performed using only CCl_4. Effects from the presence of other VOCs on partitioning and transport of CCl_4 were inconsequential for calibration.

5.4.2.3   *Volatile Organic Compound Fate and Transport Mechanisms and Parameters.*
This section contains a description of the following transport processes and parameters and how they were implemented in the VOC transport model:

- Phase partitioning, including sorption

- Gaseous diffusion and advection

- Aqueous diffusion, advection, and dispersion.

---

[c] Henry's Law: a fact in physical chemistry: the weight of a gas dissolved by a liquid is proportional to the pressure of the gas.